ENGINEERING
LIBRARY

AUG 11 1950

JOURNAL OF THE AERONAUTICAL SCIENCES

VOLUME 17 AUGUST, 1950 NUMBER 8

CONTENTS

Development of High-Speed Water-Based Aircraft ..... ERNEST G. STOUT 457

Application of Frequency-Response Analysis to Aircraft-Autopilot Stability ..... CHARLES L. SEACORD, JR. 481

Torsion of Thin-Walled Closed Cylinders Beyond the Elastic Limit ..... G. H. HANDELMAN 499

Column Buckling in the Elastoplastic Range ..... P. CICALA 508

Hydrodynamic Longitudinal Stability ..... GEORGE S. SCHAIRER 513

A Mechanical Analogy for Hypersonic Flow ..... H. REESE IVEY 519

Readers' Forum: "On the Stability for a Certain Degenerate Type of Disturbance of Viscous Fluid Flow Between Parallel Walls," by S. I. Pai; "Base Pressures at Supersonic Velocities," by A. Gabeaud; "Note on the Calculation of Deflections of Indeterminate Structures," by Bruno A. Boley and Roland H. Moore; "The Effects of Weight Variation on the Range of Air-Borne Craft," by Ralph W. Allen 525–528

Published by the

INSTITUTE OF THE AERONAUTICAL SCIENCES, INC.

JOURNAL OF THE AERONAUTICAL SCIENCES

Editor: HUGH L. DRYDEN, *Director, N.A.C.A.*

Associate Editor: ROBERT R. DEXTER *Managing Editor:* BERNEICE H. JARCK

Editorial Committee

Aerodynamics

Francis Clauser
Howard Emmons
R. Paul Harrington
R. T. Jones
Carl Kaplan
W. B. Klemperer
John G. Lee
H. W. Liepmann
C. C. Lin
H. F. Ludloff
John R. Markham
Clark B. Millikan
Shatswell Ober
W. Bailey Oswald
Allen E. Puckett
Elliott G. Reid
H. J. F. Reid
Russell Robinson
G. B. Schubauer
W. R. Sears
John Stack
Th. von Kármán
Richard von Mises

Flight Testing

W. K. Ebel
R. R. Gilruth
Melvin N. Gough
Robert Stanley
E. G. Stout

Meteorology

C. F. Brooks
D. M. Little
E. J. Minser
F. W. Reichelderfer
H. C. Willett

Structures and Materials

W. B. Bleakney
E. W. Conlon
J. P. Den Hartog
L. H. Donnell
E. C. Hartmann
N. J. Hoff
E. E. Lundquist
C. F. Nagel, Jr.
J. S. Newell
Alfred S. Niles
W. Ramberg
E. Reissner
F. R. Shanley
H. W. Sibert
C. R. Strang
S. Timoshenko
H. S. Tsien
Chi-Teh Wang

Rotating Wing Aircraft

Robert Coleman
K. H. Hohenemser
Bartram Kelley
Ralph McClarren
R. H. Miller
R. H. Prewitt
Igor I. Sikorsky

Physiologic Problems

H. G. Armstrong
Louis H. Bauer
Eugene Du Bois
W. Randolph Lovelace, II
Ross A. MacFarland
A. D. Tuttle

Flight Propulsion

George W. Brady
Frank W. Caldwell
L. S. Hobbs
E. E. Johnson
Joseph Keenan
R. P. Kroon
Arthur Nutt
Hans Reissner
Abe Silverstein
C. Fayette Taylor
E. S. Taylor
P. Taylor
E. S. Thompson
H. S. Tsien

Aircraft Design

W. E. Beall
W. K. Ebel
Hall L. Hibbard
Richard Hutton
C. L. Johnson
I. M. Laddon
C. J. McCarthy
Fred E. Weick
Robert J. Woods

Air Transport

Charles Froesch
J. A. Herlihy
R. D. Kelly
Otto E. Kirchner
Jerome Lederer
John C. Leslie
R. Dixon Speas

Instruments

Allan G. Binnie
W. G. Brombacher
Charles H. Colvin
B. M. Craig
B. Del Mar
C. S. Draper
O. E. Esval
W. L. Howland
J. E. Lindberg
David W. Moore
George H. Purcell
W. A. Reichel
C. F. Savage
O. Hugo Schuck
C. L. Seward, Jr.
R. Sylvander
D. K. Warner
P. F. Weber

Vibration and Flutter

Lee Arnold
M. A. Biot
William Bollay
Chieh-Chien Chang
Martin Goland
J. P. Den Hartog

Fuels and Oils

A. L. Beall
J. H. Doolittle
Graham Edgar
R. T. Goodwin
S. D. Heron
A. M. Rothrock

SUBSCRIPTION RATES

JOURNAL OF THE AERONAUTICAL SCIENCES, Published Monthly.—United States and Possessions: 1 Year, $12.00; Single Copies, $1.50. Foreign Countries Including Canada (American Currency Rate): 1 Year, $13.00; Single Copies, $1.50.

AERONAUTICAL ENGINEERING REVIEW, Published Monthly.—United States and Possessions: 1 Year, $3.00; Single Copies, $0.50. Foreign Countries Including Canada (American Currency Rates): 1 Year, $3.50; Single Copies, $0.50.

Notices of change of address should be sent to the Institute at least 30 days prior to actual change of address.

Manuscripts for publication, proofs, and all correspondence should be addressed to the Editorial Office of the JOURNAL.

Correspondence regarding subscriptions may be addressed to Publication Office, 20th and Northampton Sts., Easton, Pa., or to the Editorial Office of the JOURNAL OF THE AERONAUTICAL SCIENCES, 2 East 64th Street, New York 21, New York.

Copyright, 1950, by the Institute of the Aeronautical Sciences, Inc.

Entered as Second Class Matter at the Post Office, Easton, Pa., May 1, 1937. Acceptance for mailing at a special rate of Postage provided for in the Act of August 24, 1912. Authorized April 29, 1937.

JOURNAL OF THE AERONAUTICAL SCIENCES

VOLUME 17 AUGUST, 1950 NUMBER 8

Development of High-Speed Water-Based Aircraft

ERNEST G. STOUT*

Consolidated Vultee Aircraft Corporation

SUMMARY

Outstanding progress has been made in recent years in the field of seaplane hydrodynamics which has done much to bring the faltering seaplane up to modern standards of aerodynamic performance and design efficiency. In fact, extensive research programs, utilizing the dynamically similar model technique, promise to place consideration of water-based aircraft high on the program of current defense planning.

This paper outlines the salient features involved in the development of the dynamic model and associated research techniques into a practical, accurate research tool for designing water-based aircraft that demand little, if any, compromise with contemporary aerodynamic design. New seaplane design criteria are discussed, and their application to high-performance water-based aircraft is analyzed. With the high-speed propeller-driven seaplane now an actuality, attention is drawn to the solution of the supersonic water-based problem.

It is concluded that adequate design criteria and technological experience are available to meet satisfactorily or to exceed any aircraft requirement with a suitable water-based configuration.

INTRODUCTION

FROM ITS INCEPTION, the technical development of the airplane has been rapid. However, in recent years, it has been virtually land-bound, unless one was willing to accept the large performance penalties that accompanied adaptation to water operation. Because of these performance deficiencies, the seaplane for many years was restricted to only those functions where water-based operation was mandatory and outweighed other performance considerations. This left to the land-based airplane the principal task of securing and maintaining the mastery of the air—even over the seas—in spite of the hazards of forced landings and the restricted freedom of action imposed by the necessity for elaborately prepared terminal and auxiliary landing facilities.

Presented at the Aircraft Design Session, Eighteenth Annual Meeting, I.A.S., New York, January 23–26, 1950.

* Assistant to the Chief Engineer.

This situation was not always true. Dating from the first practical seaplane developed by Glenn Curtiss in 1911, seaplane design progressed rapidly through the first World War. As a matter of fact, water-based development outstripped contemporary landplane design during that period to such an extent that, by 1938, all long-range transport was still accomplished by flying boats and the world's speed record was held by a seaplane. From a hydrodynamic point of view, this early development period culminated in the design and construction of the famous NC flying boats in 1918. The hull of the NC was 45 ft. long with a beam of 10 ft., and it was this hull that influenced basic seaplane design and hydrodynamic criteria for the following 20 years, during which period little research was directed toward the improvement of hull design.

During this static period, seaplane development centered about a few fundamental design criteria that had gradually evolved from trial and error and long experience. While it was recognized that basic improvements in hydrodynamic design were no doubt possible, research had lagged to the point where aircraft manufacturers were not justified in deviating, nor could they afford to deviate, far from established trends. Limited progress continued, but this was largely due to costly flight-test programs and the incorporation of improved air-frame and engine installations. This situation resulted from the fact that there was no satisfactory research procedure available for the rapid and accurate determination of the complex discontinuous variables involved during simultaneous operation in two media—i.e., air and water.

The introduction in this country of the dynamically similar model technique of research (by the author in July, 1938[1]) for the first time presented the airplane designer with a practical research tool for designing the hull of a seaplane which was complementary to, and as

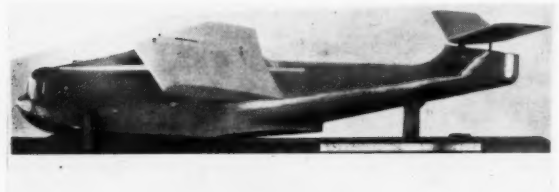

FIG. 1 (*top*). Original configuration of the XPB2Y-1 which gave an operational gross weight limit of 40,000 lbs. (*Bottom*). The revised XPB2Y-1 hull which resulted in an operational gross weight of 86,000 lbs.

modern in concept as, his science of aerodynamics. With this versatile scientific tool available, extensive hydrodynamic research programs were initiated during the past war to meet the ever increasing demands for increased seaplane efficiency and reliability. For example, the Coronado, a large four-engined patrol bomber flying boat, was increased from a maximum operational gross weight of 40,000 lbs. to a weight of 86,000 lbs.—over double—solely through the application of an intensive dynamic model research program. Fig. 1 shows the modification that eventually was found necessary in this case, and it is obvious that such an extensive revision of lines would not have been discovered by the costly time-consuming procedure of full-scale cut and try. The model tests, on the other hand, indicated a complete solution to the problem in 3 weeks of testing. In a like manner, the performance and efficiency of the famous Convair Catalina, Martin Mariner, Boeing Clipper, and other World War II seaplanes were greatly increased at a most critical period of the war effort.

With this outstanding confirmation of the effectiveness of the dynamic model in rapidly solving complex hydrodynamic problems and in spite of the urgency attached to improving existing seaplanes during the war, considerable effort was directed toward applying this new research technique to the fundamental solution of basic hydrodynamic criteria. The war was demanding that the range and load-carrying ability of seaplanes be improved. The only known method at the time was to overload continually these aircraft to the point where seaworthiness and water-handling characteristics were greatly impaired, attempt to refine the existing design still further, and then overload again. It was imperative, therefore, that some other fundamental means be found whereby the desired seaworthiness could be attained without impairing the load-carrying ability while at the same time allowing marked improvements in performance, which at best was dangerously low.

In searching for a fundamental concept that would allow radical improvement in hull performance, an *N.A.C.A. Technical Memorandum*[2] was recalled which briefly abstracted some experiments conducted by Sottorf in Germany. This report presented meager resistance and spray information on a series of high length-beam ratio hulls which, when carefully analyzed, held considerable promise for a solution to the problem just discussed. The brief summary presented in the N.A.C.A. publication was insufficient, however, for a thorough analysis, and the complete reports were ordered from DVL in Berlin. These reports, which were actually received after outbreak of war in Europe, were completely translated by Convair[2] and were found to contain a complete account of the German experiments.

More thorough analysis of these later data confirmed preliminary theoretical studies that high length-beam ratio hulls held out a definite promise for marked hydrodynamic improvement. However, it was also realized that these studies were based on a series of resistance-type tank models and that many more data, particularly on the stability and relationship of secondary design parameters, were required before utilization of the basic principles embodied in these hulls could be realized.

A Navy research authorization was granted to Consolidated Vultee, and, under the direction of Convair hydrodynamicists, carefully planned and integrated dynamic model research programs were organized at the N.A.C.A. Towing Tank, Stevens Institute Towing Tank, and Convair's own Hydrodynamics Research Laboratory. This resulted in a new family of hull forms of superior performance. It was through the application of basic design criteria obtained from this intensive research program that the XP5Y-1, the Navy's newest flying boat, was developed. This high-speed turboprop seaplane, shown in Fig. 2, represents the first water-based design in this country to deviate radically from the pattern established by the outmoded NC flying boats of World War I.

Like the NC boat, the XP5Y-1 has a beam of 10 ft. Fully loaded, the NC had a gross weight of 28,000 lbs., whereas the XP5Y-1 demonstrates excellent hydro-

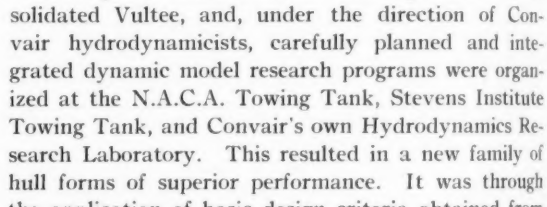

FIG. 2. The Navy's new XP5Y-1 turbopropeller-powered high-speed flying boat incorporating a high length-beam ratio hull.

dynamic characteristics up to 150,000 lbs. The increase in efficiency of the new high length-beam ratio hulls does not, however, stop with load. Hydrodynamic instability, such as porpoising and skipping, has been brought under control through the use of dynamic models and no longer restricts the operation of new seaplane designs to a narrow band of stable limits; hence, the versatility, safety, and seaworthiness of the modern flying boat were greatly increased. High hull fineness ratio, which allows the incorporation of easy buttocks and sharp waterlines, has done much to minimize the problem of spray and greatly increase seaworthiness and rough-water performance. This same feature has resulted in hulls of low frontal area, representing large decreases in aerodynamic drag. In conjunction with such design innovations as multicellular watertight integrity, propeller-turbine engine developments, and automatic mooring and docking techniques, the seaplane designer is now able to put a high-performance propeller-driven seaplane into the air which fully meets the exacting requirements of modern design and yet takes full advantage of the inherent strategic advantage of water-based aircraft from the operational standpoint of mobility and dispersion of forces.

If seaplane development were not to falter again, as it did after the first World War, it was obvious that the successful development of high-speed propeller-driven seaplanes would provide only temporary respite unless steps were taken to develop the water-based aircraft into an efficient and dependable transonic, and eventually supersonic, aircraft. The adaptation of transonic aircraft design to water-based operation, without sacrificing any of the high standards of hydrodynamic performance which have been introduced into seaplane design during the past few years, posed what at first appeared to be an insurmountable problem. It was apparent from the outset that extensive aerodynamic refinement of known hydrodynamic forms of high quality would merely result in poor hydrodynamic performance without ever fully obtaining the aerodynamic cleanliness required for transonic flight. It appeared logical, therefore, to start with an ideal aerodynamic configuration and, by means of extensive dynamic model research, develop new hydrodynamic principles and applications that, though different in concept, would result in the same degree of seaworthiness and stability normally associated with the best hulls of conventional form.

In line with the above reasoning, it was obvious that the basic "in-flight" configuration must consist of a smooth, unbroken form, utilizing high critical Mach sections throughout. In order to secure elementary floatation, it was necessary to supply sufficient volume of body so that engines, air inlets, jet exhausts, and personnel would not be inundated. The combination of these two fundamental requirements led logically to the blended-wing-hull configuration as the most promising approach to the basic problem.

FIG. 3. A dynamically similar flying model of the first jet-propelled, blended-hull configuration to be developed for a transonic water-based aircraft.

By proceeding in this logical manner, a large number of transonic hydrodynamic configurations were designed and tested as free-body dynamic models—some were catapulted, others were towed, and many were actually flown, self-propelled with their own jet engines. It became increasingly apparent that a true aerodynamic form could meet adequately, or in some cases exceed, the established design criteria for satisfactory hydrodynamic performance. The first in this long series of transonic water-based configurations is illustrated in Fig. 3. Continual refinement has radically altered the appearance of these high-speed aircraft over that shown in this figure. However, the new research philosophy out of which it was conceived is firmly established, and the little dynamic model shown in Fig. 3 may well represent, in the years to come, the real rebirth of sea power. For, with the transonic water-based aircraft a practical reality from a technical standpoint, the revitalized hydrodynamic research program at Convair is already well into the problems of water-based supersonic flight.

The following sections of this paper will outline the development of the dynamically similar model and its associated research techniques. Within the limits of security classification, the more important hydrodynamic design criteria that have been obtained from the above research will be discussed.

DYNAMIC SIMILARITY

Fluid Resistance

Before discussing the various research techniques, equipment, and design criteria that have been developed around the use of dynamically similar models, it is believed desirable to review briefly the basic theoretical background upon which this versatile applied science is based. Classical hydrodynamics considers the perfect fluid that is defined as incompressible and nonviscous—i.e., there is no resistance to shearing between the elements. Water is, for all purposes, incompressible; however, it has viscosity and other characteristics such as surface tension which require special attention and cannot be neglected. The general resistance equation for the force acting on a body in

motion, partly or wholly immersed in an imperfect fluid such as water, can be expressed in the following form:

$$R = (\rho V^2 L^2) f\left[\tau, \frac{V^2}{gL}, \frac{\rho VL}{\mu}, \frac{V}{a}, \frac{l}{L}, \frac{v}{V}, \frac{V^2 L}{\gamma}, \frac{L}{b}\right] \quad (1)$$

where the variables are density of the fluid, ρ; velocity of the body, V; linear size of the body, L; trim or angle of attack, τ; gravity, g; coefficient of viscosity, μ; compressibility of the fluid, V/a; surface roughness, l/L; texture of the fluid flow or turbulence, v/V; surface tension, γ; and fineness or aspect ratio, L/b.

The term $\rho V^2 L^2$ is the main term of the expression and is recognized as the force due to density. We are accustomed to the use of a single nondimensional coefficient of resistance instead of the complex function in the brackets. It must be borne in mind, however, that such a single coefficient, when used, varies with, and attempts to be, the equivalent of the terms listed. Some of these terms may be negligible, but all are subject, to some extent, only to experimental determination.

In hydrodynamic experimental testing, it is necessary to determine $f_1(\tau)$ or the variation of resistance coefficient with trim. Because of the gravity effects associated with wave-making, the term $f_2(V^2/gL)$, or Froude Number, must be met. Because of the dependence of frictional resistance on viscosity, $f_3(\rho VL/\mu)$, or Reynolds Number, must be calculable or an allowance made. As we are dealing with incompressible water, the compressibility term $f_4(V/a)$ may be neglected. If tests on two models do not agree, the surface roughness $f_5(l/L)$ may not bear the same relation in the two cases. This function has a strong bearing on frictional resistance as does $f_6(v/V)$, which is the stream turbulence as represented by the ratio of the average lateral turbulence velocity to the measured axial velocity. Surface tension represented by $f_7(V^2L/\gamma)$ can, in most cases, be neglected, except possibly in accurate studies of spray formation. Experiments have been conducted where this term is eliminated by the introduction of Aerosol, or some other commercial wetting agent, to the water. Finally, it is apparent in aerodynamics, and is becoming increasingly so in hydrodynamics, that fineness or aspect ratio, represented by $f_8(L/b)$, cannot be neglected. In hydrodynamics, this becomes the ratio of the planing bottom fineness or length to beam ratio. These are by no means all of the dimensionless combinations that may be written, but they comprise what are usually considered the most important.

Using this typical example of the numerous factors influencing fluid resistance, three important facts can be derived which apply equally well, though varying in detail, to all other quantities for which scale reproduction is desirable:

(1) Theoretically, no model test can completely represent a full-scale condition unless all of the dimensionless ratios are held constant.

(2) It is impossible to hold all of these ratios constant at the full-scale value in a model test, for some of them are contradictory.

(3) The dimensionless ratios may not have equal weight, but theory does not show it.

Experience tells us, however, that the angle of attack or trim is the most important of all the terms given and that for hydrodynamic work the Froude Number should be held constant. It is obvious from this discussion that experimental research on models, in an attempt to determine or predict full-scale behavior, is not a cut-and-dried procedure but is a series of compromises based on judicious judgment and experience. Even the meticulous matching of Froude Number does not assure similarity. For the lower speed régimes where wave-making predominates, it will give close approximations, but, as the speed increases to high-speed planing on the water, the function of Reynolds Number becomes more and more predominant. While the above discussion appears to present a pessimistic picture of experimental model testing, it should be pointed out that, by comparison, the theoretical or analytical solution to hydrodynamic problems, particularly those concerned with stability, is practically hopeless, with no prospect of improvement. On the other hand, rapid progress has been made toward the solution of the problems associated with dynamic similarity, and it appears that the full application of this relatively inexpensive and direct approach to the solution of discontinuous complex variables is virtually unlimited. Later sections of this paper will discuss in more detail the specific deviations from theoretical similitude and the remarkable degree of accuracy that can be obtained from the modern dynamic model when it is properly designed and operated.

Froude's Law of Comparison

In the previous section on fluid resistance, it was stated that Froude Number, V^2/gL, must be held constant in all cases of experimental hydrodynamics when anything but the specific full-scale configuration itself is being investigated. It was further stated that, with calculated reservation, the holding of this function constant would most nearly result in model experiments producing quantitative data directly commensurate with full scale. As these statements contain the heart of all hydrodynamic research and analysis, it is advisable to become more familiar with the character and limitations of this function.

In 1867, William Froude had constructed what is generally conceded to be the first modern towing tank, and, by 1879, when he died, he had contributed volumes to the science of naval architecture. Of greatest significance was his famous Greyhound tests, where a 172-ft. boat named the "Greyhound" was towed by

H.M.S. "Active." By duplicating the full-scale tests in his towing tank with a $^1/_{16}$-scale model and by applying appropriate coefficients of friction to both full scale and model, from data previously determined in the tank, he was able to separate that portion of the total resistance due to gravitational wave formation and eddies. By analysis of these data, Froude determined that, if any full-scale speed was divided by $\sqrt{16}$ (the square root of the model scale), the wave and eddy resistance of the model at that speed was equal to the corresponding resistance of the full-scale ship divided by 16^3 (the model scale cubed). This relationship Froude called the "Law of Comparison." By referring to Eq. (1), we see that the second function in the bracket, V^2/gL, previously called Froude Number, demands that V vary as the square root of the linear dimension L if model comparison is to be valid.

As pointed out, this relationship applies only to residuary resistances and wave formation. If we were limited to ideal fluids, Froude's Law of Comparison would be sufficient. However, the functions of viscosity, surface tension, and other properties of water are such that any attempt to bring them into a law of similarity requires the introduction of Reynolds Number as well. The conditions where Reynolds and Froude agree exist only at full scale. If the frictional component is small, as is usually the case in the larger tank models of conventional speed seaplanes, it is possible to neglect its effect and proceed under Froude's comparison and scale total resistance directly to the scale cubed. In most cases this will result in a degree of full-scale conservatism which will cover items of surface roughness and protuberances not usually present in the model tested. If, on the other hand, we are dealing with small models of extremely high-speed planing craft, gravitational resistance may be small or negligible, and large errors will result if the frictional resistance is not separately treated at the proper Reynolds Number as in aerodynamic theory. Fortunately, the majority of critical items of hydrodynamic performance, such as stability, spray formation, seaworthiness, etc., occur at low speeds in the range of transition from displacement to planing and thereby closely follow Froude's Law. For emphasis it should be pointed out again that one will find all of the standard coefficients and parameters of seaplane design based on Froude's Law of Comparison and, unless the research engineer is fully aware of the limitations and treatment of this function, that serious inconsistencies will result, particularly as the trend for higher speed water-based aircraft continues.

Dimensional Analysis

Inasmuch as experimental research is the foundation of all applied hydrodynamics for the seaplane designer, it is necessary that the engineer understand the dimensional test equivalents for all factors encountered full scale. In the two previous sections, we have discussed the components of hydrodynamic resistance and how this force varies with linear scale. In this section, with Froude's Law as a basis, we will develop the relationship of many other interrelated physical functions of dynamics and mechanics to linear scale. Keeping in mind the inherent, but calculable, discrepancy of Froude's fundamental Law of Comparison, we can establish mathematically how every other physical quantity must vary to keep the total dimensionally correct.

In the early days of seaplane research and ship design, the designer was primarily occupied with the resistance of his hull forms, and, consequently, the basic law of comparison, as stated by Froude, dealing with the relation of resistance to speed with varying scale was adequate. However, with increasing knowledge of hull form and the rapid development of powerful engines, resistance was gradually, but steadily, subordinated to the more critical studies of dynamic stability on the water and the factors affecting spray formation and seaworthiness. As stated previously, the most direct approach to these problems is through the use of dynamically similar scale models. To obtain accurate results for these complex dynamic problems, it is necessary for the models to be dimensionally correct in all respects to the full-scale prototype—i.e., they must not only be geometrically to scale, such as a wind-tunnel model or resistance-tank model, but it is also required that they have, among other things, gross weight, inertia, power, accelerations, and all aerodynamic forces and moments to scale. It is obvious, therefore, that, if this can be accomplished throughout for every factor, we have in effect a flying miniature of the full-scale airplane that will perform every maneuver of the full-scale aircraft and at a rate of movement directly to scale. *In effect, the dynamic model becomes a complex integrating mechanism that automatically picks up every known or unsuspected force, in the proper magnitude, point of application, direction, and sequence; integrates all these reactions instantaneously; and provides the observer with the resultant motion and rate.* Even if there were no unknown transient forces, the task of integrating all known forces in a complex dynamic reaction by analytical means, for just one speed point, is enormous. It is this goal of tremendous simplification of integrating all forces on a free body which has made the problems associated with the attainment of such a model seem inconsequential by comparison.

Because the dynamically similar flying model represents the ultimate in experimental research at reduced scale, we shall develop the principal scale relationships involved in its design and analysis. It is apparent that, if sufficient basic factors are dimensionally correct, other minor dependent variables will automatically follow. Therefore, the derivations and relationships that follow are the principal functions involved and should be sufficient for most analyses. The engineer

will find it a simple matter to derive certain other functions not specifically listed in this compilation.

In the following derivations we will consider that the symbol for scale, λ, represents the whole number—i.e., if $\lambda = 8$ then the linear scale is $^1/_8$ or λ^{-1}. As the linear or geometric scale, λ^{-1}, is usually given, it is desired to get all other physical relations in terms of this one value. It is obvious, therefore, that, if the linear scale is a ratio of lengths L, then L varies directly as $1/\lambda$ or λ^{-1}, written $L \propto \lambda^{-1}$. Following this procedure, it is plain that an area is made up of a length times a length or L^2. Therefore, area, or L^2, varies as the linear scale squared —i.e., area $\propto \lambda^{-2}$. In a similar manner, it may be reasoned that a volume or mass is an area, L^2, multiplied by thickness or height, L, giving L^3. Hence, volume, weight, or, as Froude determined, force $\propto \lambda^{-3}$. As the moment of a force is that force multiplied by an arm, L, we may extend our reasoning to show that moment $\propto L^4$, or λ^{-4}. Similarly, the moment of inertia is a mass multiplied by the arm squared, or moment of inertia $\propto \lambda^{-5}$.

Since our system of similarity is based on Froude's Law of Comparison and since we have seen from Eq. (1) that this expression depends upon the speed varying with the square root of the linear dimension, it follows that velocity $\propto \sqrt{L}$ or $\lambda^{-1/2}$. As distance is a linear dimension, L, and velocity varies as the $\sqrt{L}$, then time, which is distance divided by velocity, or $L/\sqrt{L}$, must also vary with $\sqrt{L}$. Hence, time $\propto \lambda^{-1/2}$. Now that we have the basic variations of mass, length, time, and velocity, it is a simple matter to substitute in the expressions for any physical function and derive its variations with linear scale. For instance, revolutions per minute is revolutions, which are nondimensional, divided by time, or $1/\sqrt{L}$, which gives us the relation r.p.m. $\propto \lambda^{1/2}$. Likewise, acceleration is feet per second squared, or $L/(\sqrt{L})^2$, giving acceleration $\propto 1$, or unity; hence, it becomes nondimensional. This means that all model linear accelerations will be identical to the full-scale accelerations in magnitude. On the other hand, if we consider angular motion, we find that angular velocity is nondimensional radians divided by seconds, or $1/\sqrt{L}$, giving, as in the case of r.p.m., $\omega \propto \lambda^{1/2}$. As angular acceleration is radians per second squared, or $1/L$, we have simply $\alpha \propto \lambda$ for this quantity. Whereas we found that linear acceleration is identical to both model and full scale, we see that angular acceleration will be the whole number λ times as great in the model as the full-scale value. The fact that linear accelerations do not vary with scale is fortunate, inasmuch as the value g, which is the acceleration due to gravity, is a constant over which we have no control and corrections would be extremely difficult at best, if not impossible.

Continuing our derivations into the more complex functions, we recall that power is defined as the work accomplished per unit of time, where work is the product of a force times the distance through which it acts. Following the previous line of thought, we can consider that force, L^3, times the distance of action, L, causes work to vary with the fourth power of linear scale—i.e., work $\propto \lambda^{-4}$ and power will therefore be $L^4/\sqrt{L}$, which gives $L^{7/2}$ or power $\propto \lambda^{-7/2}$. That these relationships are dimensionally correct can be quickly checked by substituting these derived values into any formula defining some nondimensional coefficient and thereby demonstrate that the numerical value of the coefficient does not change with scale. For this demonstration we can pick such an expression as the following, which defines the well-known nondimensional power coefficient, C_P:

$$C_{P_{(\text{full scale})}} = \frac{5 \times 10^{10} \times \text{b.hp.}}{(N)^3 \times (D)^5} \tag{2}$$

where b.hp. is the brake horsepower, N is the propeller revolutions per minute, and D is the propeller diameter in feet, all full-scale values. From our previous discussion we know that the C_P for the model would be

$$C_{P(\text{model})} = \frac{5 \times 10^{10} \times (\text{b.hp.} \times \lambda^{-7/2})}{(N \times \lambda^{1/2})^3 \times (D \times \lambda^{-1})^5} \tag{3}$$

and, solving for the variation of λ, we find

$$C_{P_{(\text{model})}} \propto \frac{\lambda^{-7/2}}{\lambda^{3/2} \times \lambda^{-10/2}} = \frac{\lambda^{-7/2}}{\lambda^{-7/2}} = 1 \tag{4}$$

Therefore, the ratio of $C_{P(\text{full scale})}$ to $C_{P(\text{model})}$ is unity.

For convenience, Table 1 is presented which summarizes the principal relationships in condensed form, giving, in addition, a typical set of values for an assumed value of $\lambda = 8$ giving a linear scale of $^1/_8$.

TABLE 1
Dimensional Conversion for Linear Scale

Unit	General Conversion	$^1/_8$ Scale, $\lambda = 8$
Linear dimensions	λ^{-1}	1/8
Area	λ^{-2}	1/64
Volume, mass, force	λ^{-3}	1/512
Moment	λ^{-4}	1/4,096
Moment of inertia	λ^{-5}	1/32,768
Linear velocity	$\lambda^{-1/2}$	1/2.83
Linear acceleration	Constant	1
Angular velocity	$\lambda^{1/2}$	2.83
Angular acceleration	λ	8
Time	$\lambda^{-1/2}$	1/2.83
R.p.m.	$\lambda^{1/2}$	2.83
Work	λ^{-4}	1/4,096
Power	$\lambda^{-7/2}$	1/1,446
Wing loading	λ^{-1}	1/8
Power loading	$\lambda^{1/2}$	2.83

The interesting fact to note in closing this brief discussion of dimensional analysis is that all of the factors listed in Table 1 have been experimentally checked on numerous occasions by constructing and testing models

of existing airplanes for the purpose of positive correlation. For instance, in the case of the Navy's XP4Y-1, a 1/8-scale, radio-controlled, dynamically similar model (Fig. 4) was constructed and thoroughly correlated with the full-scale airplane, as well as wind-tunnel and towing-basin, tests. With accurate scale propellers set at the actual full-scale blade angle and with the r.p.m. adjusted to 2.83 times the full-scale value (see Table 1), the engine power was measured on a dynamometer and was found to be 1/1,446 the full-scale value, and the thrust developed was 1/512. With this power and a model weight of 1/512 full scale, the model was found to become air-borne at a time and speed equal to 1/2.83 that observed during flight tests. Linear acceleration at the hump and getaway was found to be the same on model and full size. Additional description and results of these correlation studies, particularly with regard to the more complex functions involved in the stability derivatives, are covered in more detail in reference 4.

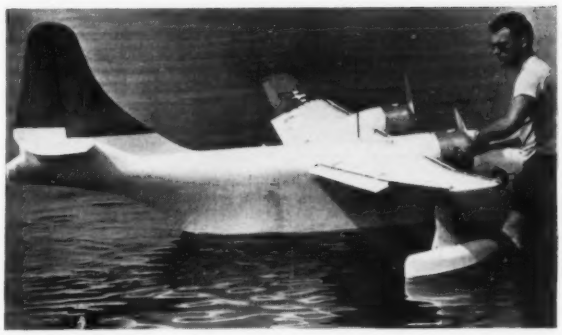

FIG. 4. The first completely free-body, self-propelled dynamically similar model to be flown by remote radio control. A 1/8 scale model of the XP4Y-1.

RESEARCH TECHNIQUES

Towing Tank Testing

The oldest and most usual form of dynamic model testing is in a towing tank. Prior to the introduction of dynamic models, these towing tanks were used primarily to tow solid resistance models through the water, much as William Froude did in the late 1800's. These resistance models were attached to a towing carriage through a dynamometer linkage such that resistance and moments at fixed trims or free to trim resistance at various speeds could be recorded. The results were similar to those obtained in a wind tunnel, inasmuch as forces and moments due to form only were the principal products of the testing.

With the introduction of dynamically similar scale models in 1938, it became necessary to revise all the old procedures and equipment of tank testing in order to take advantage of the unlimited opportunities afforded to investigate the dynamic effects of hydrodynamic stability and its interrelated influence on the associated aerodynamic parameters of the aircraft as a whole. The towing tank became a free-stream turbulence wind tunnel, as well as a water channel, and the models had to be given as many degrees of freedom as physically possible in order that resultant motion would be unrestrained. Inasmuch as pitching and heaving motions associated with the cyclic hydrodynamic stability problem known as porpoising were of immediate concern and because of the fact that the towing channels were narrow, precluding lateral deviations from a course down the center of the tank, it was customary to mount the models so that they had freedom in pitch and rise but were restrained in yaw, roll, and freedom along the longitudinal axis.

This is accomplished in a manner illustrated in Fig. 5, which shows the 1/10 scale powered model of the XP5Y-1 attached to the towing carriage of N.A.C.A. Tank No. 1 at Langley Air Force Base, Va. The rectangular towing staff is pivoted at the center of gravity of the model and allows freedom in pitch while restraining the model in yaw and roll. The staff is machined on all faces and rides in a roller cage attached to the carrier. The roller cage restrains the staff in yaw and holds it to a vertical position but allows complete freedom in rise. It will be further noted in Fig. 5 that the roller cage is mounted to the carriage truss through a dynamometer linkage so that resistance and/or thrust may be measured during the run.

Early experiments were conducted with unpowered models, and the towing force or thrust was transmitted to the model through the towing staff to the model center of gravity. While this procedure was providing many results theretofore unattainable, true dynamic similarity was not obtained, and every effort was made, in conjunction with the N.A.C.A. staff, to improve continually the efficiency of dynamic models and their technique of testing. In 1940, it became obvious that the models should incorporate scale power and running propellers in order to further enhance and refine the ex-

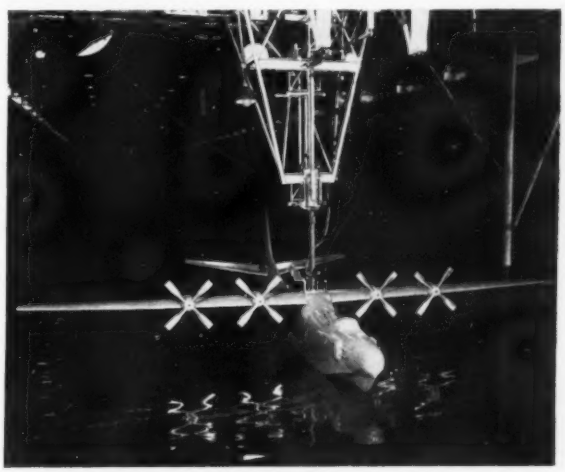

FIG. 5. The 1/10 scale XP5Y-1 dynamically similar powered model in the N.A.C.A. towing tank at Langley Air Force Base.

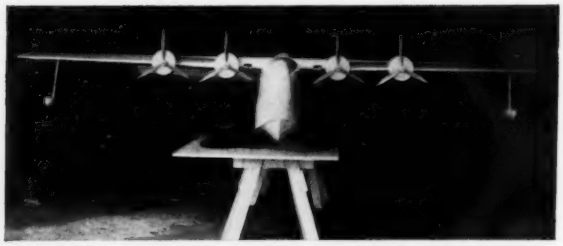

FIG. 6. The 1/8 scale Coronado powered dynamically similar towing tank model.

cellent data being obtained. Convair was given a contract by the Navy to design and install variable frequency power equipment in the N.A.C.A towing tank, along with associated development of lightweight electric motors, adjustable-pitch metal propellers, and other equipment involved in going to power operation. A 1/8 scale dynamic model of the Convair Coronado, shown in Fig. 6, became the first model to be tested with this equipment.

The absence of complete freedom of motion still restricted the scope of testing and precluded any study of directional problems. Various attempts were made to incorporate additional degrees of freedom of a limited nature, mostly without success. One important result of these studies was the development of a rail system for the roller cage which allowed an appreciable amount of fore and aft freedom. With careful control of model and carriage power, it became possible to operate the model truly self-propelled for short periods of time. However, except for certain special constant-speed runs, the basic towing tank technique consists of towing a powered model, rigidly attached to the towing carriage through the center of gravity pivot and having freedom in only pitch and rise.

There are four basic testing techniques utilized in tank-testing of dynamic models which will be briefly discussed:

(*1*) *Constant Speed Run.*—The constant speed run is not a dynamically similar function inasmuch as the important acceleration parameter is neglected. Nevertheless, this technique is valuable for establishing certain fundamental hydrodynamic criteria such as trim limits of stability, resistance, underwater flow photographs, and spray patterns. Because of the ease in duplicating test conditions and the time available for observation, the influence of extremely small variables may be detected.

(*2*) *Accelerated Run.*—The accelerated run, where the model is accelerated at a constant rate from standstill to getaway, most nearly simulates full-scale operation. While the actual take-off run of a seaplane is not made at a constant acceleration rate, it is not feasible to vary this factor in the towing tank because of the high inertia and complicated speed control of the towing carriage. It is customary to set a constant rate equal to the acceleration of the aircraft during the critical speed range at the hump and maintain this rate constant to getaway. An even more serious drawback to accelerated runs in the towing tank is the inability of any present-day equipment to match the accelerations being studied for modern high-speed water-based aircraft, which are approached 1/3g in some cases. The accelerated run technique is used in all cases for evaluating the stability range, aerodynamic control, and spray characteristics of a specific design configuration.

(*3*) *Landing Run.*—This technique involves getting the model up to stabilized flight as rapidly as possible in order that a landing from the flight attitude may be made. The majority of these landings are made with the model attached to the towing carriage, which is decelerated from flight speed at a constant rate. Here again, in most cases, it is not feasible to decelerate the heavy towing carriage at a rate commensurate with full scale, and, being rigidly attached, the predetermined rate of the carriage is impressed upon the model regardless of the varying decelerating forces it may experience. In certain cases where the model is small, it has been found practical to launch the model from the carriage in free flight. Landings under these conditions are dynamically similar and, consequently, are much more desirable in that they overcome the above objections to the rigid attachment. Obviously, control and instrumentation is complicated considerably by this latter technique.

(*4*) *Generalized Similarity.*—This last towing tank procedure is commonly called the "Stevens Method," inasmuch as it represents the unique testing technique employed by the Experimental Towing Tank at Stevens Institute of Technology. Fig. 7 illustrates the Stevens towing carriage with a dynamic model attached. Here it will be noted that the aerodynamic parameters and derivatives are introduced through calibrated weights, springs, and dash pots. While all of the full-scale parameters must be known in order to set up their equivalents on the model system for specific

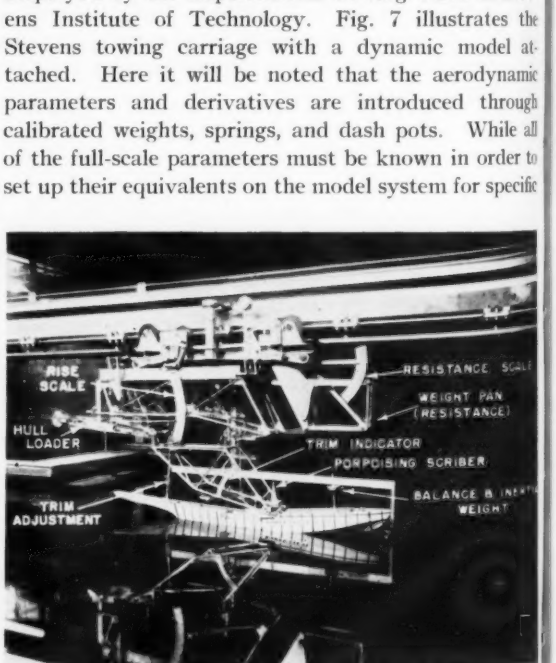

FIG. 7. The Stevens Institute of Technology towing tank and dynamic model towing carriage.

tests, this method does prove versatile for generalized problems where it is desirable to introduce the aerodynamic derivatives as independent variables. It is difficult to determine a specific evaluation by this method, such as is possible with the accelerated run technique; however, for rapid comparative study of many variables, this technique is superlative.

Steady progress has been made in the continual effort to minimize or eliminate inaccuracies in the scale-testing of dynamically similar models in the towing tank. Obviously, the ideal situation is to have a fully instrumented, self-propelled free body under the positive control of an operator. Such a model would inherently produce the proper variation of acceleration and unrestrained motion in space. In spite of the physical limitations and compromises of the towing tank, this equipment produces accurate results in the hands of experienced analysts who fully recognize, and allow for, the deviations from dynamic similitude.

Free-Body Testing

During World War II, the facilities at the N.A.C.A. and other towing tanks in this country became crowded, and many high priority developments were suffering long delays. To alleviate this condition and at the same time obtain for the first time the optimum condition previously mentioned (that of having complete free-body operation), Convair started to develop a system of free-body dynamic model research. The heart of this development is the large, natural outdoor towing basin available in the form of the U.S. Naval Training Station Estuary, illustrated in Fig. 8. This ideal testing facility is an arm of San Diego Bay, and it is completely contained in the center of a military reservation, which provides excellent security protection. Located adjacent to Convair property, its smooth sand beaches and calm protected water allow dynamic models to be operated by the contractor at his plant, thus ensuring uninterrupted research and development.

As discussed previously, the problems associated with complete free-body operation are numerous. The models must be propelled and be under positive control, and, to be of any value, technical test data must be accurately and rapidly available. This has resulted in the development of many new pieces of test equipment and of new research techniques. However, as in the early development history of the dynamic model itself, the potential rewards in the form of versatility, speed of results, and accuracy outweigh the purely mechanical problems associated with the attainment of this goal. For instance, unlike the inherent restrictions of the towing tank, the free-body model produces unrestrained resultant motion about all axes, allowing complete studies to be made of directional stability, water-looping, low-speed maneuvering and control, drifting in seas, course-keeping, and other specified problems, in addition to the standard straightaway run. Take-off time

FIG. 8. The San Diego Naval Training Station Estuary used by the Convair Hydrodynamics Laboratory for open-water free-body testing of dynamically similar models.

and distance under all conditions of varying seas, wind, and loading can be determined immediately without recourse to the complicated take-off integral. Perhaps of greatest value, however, is the ability to operate in an environment as natural as nature itself. The towing tank has always presented a problem when evaluation or study of the influence of rough or mixed sea conditions is desired. Inasmuch as an actual seaplane rarely operates in a flat calm, the entire field of typical service operational problems has received but cursory examination. The waves propagated in a towing tank always meet the model head-on, which is the most hazardous and least recommended procedure for landing a full-scale seaplane in rough water. To make matters more difficult, the assisting stiff head wind invariably present in head-on seas of the type generated in a towing tank is not duplicated, which allows the model to encounter these heavy seas with extremely excessive speeds. On the other hand, at the outdoor estuary the gradually rising mid-day and afternoon breeze provides a daily testing period from 3 to 4 hours of flat calm in the morning, for precision laboratory type of testing, to scale head winds of 30 to 40 knots in the early afternoon. By judicious selection of time of day, any degree of full-scale operational conditions may be obtained. Likewise, heading and sea condition may be varied at will. With the desired wind and heading selected, artificial seas of any desired pattern and com-

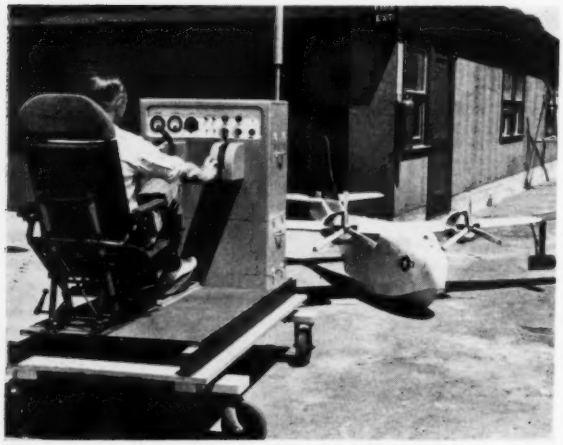

FIG. 9. The 1/8 scale XP4Y-1 radio-controlled model and the seven-channel proportional control transmitter developed by the Convair Hydrodynamics Laboratory.

plexity can be generated in the path of the model by external sources. With the models under remote control and free of all restraint, valuable information can be obtained concerning characteristics most difficult and hazardous to secure full scale and impossible to secure in the towing tank.

There are four basic open-water, free-body research techniques currently being used to develop high-speed water-based aircraft; these will be discussed as follows:

(*1*) *Radio Control.*—As stated previously, to take full advantage of the great potentialities of the free-body research technique, it is necessary to have a self-propelled dynamically similar model under the positive control of an operator with an accurate system for recording test data. The precise development of any one of these requirements is a major undertaking when the small available weight and space allowances are considered.

In June of 1943, development was started of a 1/8 scale dynamically similar model of the Convair XP4Y-1 twin-engined flying boat to be remotely controlled by positioning, multichannel radio. Scale requirements called for a gasoline power plant of 1 1/2 hp. at 4,250 r.p.m. and not to exceed a weight of 4 lbs. Ohlsson & Rice Manufacturing Company, of Los Angeles, produced this engine in 4 months after date of contract, and the first problem, that of self-propulsion with scale power, was solved.

To attain precision positive control, the Convair Radio Laboratory developed a seven-channel, positioning radio transmitter, lightweight receiver, and associated servomechanisms. The detail technical development of this interesting and elaborate system is fully described in reference 5 and will not be repeated here. With self-propulsion and a precise remote control system available, attention was directed toward developing an accurate phototheodolite tracking and film analyzer system for recording the motions and accelerations of the free body in space. The first completely instrumented, radio-controlled free-flight dynamic model was successfully demonstrated by Convair in August, 1944, just 14 months after initiation of the program. This original model is shown in Fig. 9 and a complete description of its development and correlation with full-scale flight tests and the towing tank is given in reference 4.

Following the successful demonstration of precision free-body control and analysis, a concerted program of research was initiated in an effort to overcome the serious seaplane problems discussed in the introduction to this paper and, once again, to place efficient, high-speed water-based aircraft in the forefront of defense planning. A total of 27 dynamically similar radio-controlled research model configurations were tested to determine the fundamental factors affecting hydrodynamic efficiency. Out of this intensive study came the full development of the remarkable high length-beam ratio hull, which resulted in the Navy's new turbopro-

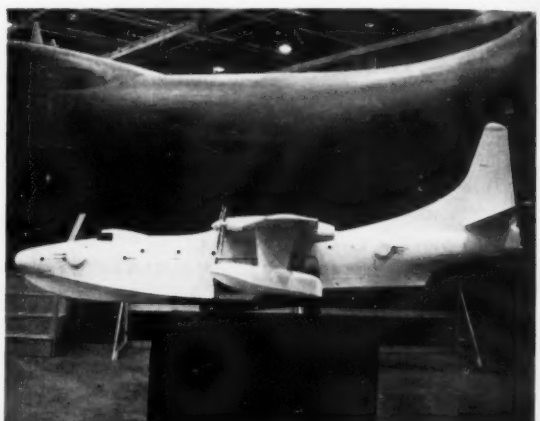

FIG. 10. The 1/10 scale XP5Y-1 radio-controlled free-flight model sitting in front of the full-scale mock-up.

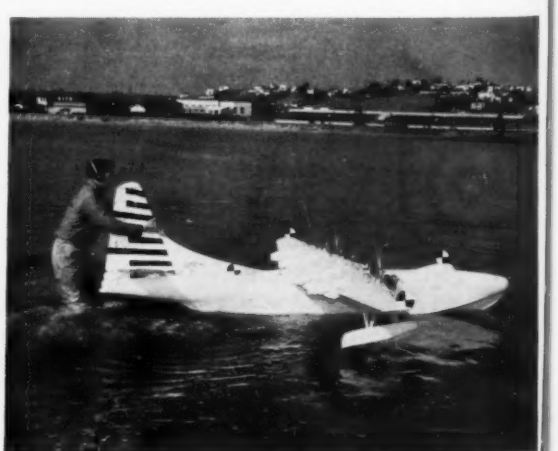

FIG. 11. The XP5Y-1 free-flight model just prior to being released for a self-propelled radio-controlled test flight at the estuary.

peller-powered XP5Y-1 previously discussed and shown in Fig. 2.

The $^1/_{10}$ scale radio-controlled dynamically similar model of the XP5Y-1 is shown in Figs. 10 and 11. This model has made over 2,000 test runs during the past 3 years and has completed the full hydrodynamic flight-test program scheduled for the full-scale aircraft. In addition to performing the functions normally expected of the full-scale aircraft, the model has thoroughly explored régimes, attitudes, and conditions considered far too hazardous to risk human life and costly equipment to investigate during flight testing. Many of these conditions, once investigated by the model, have proved to be satisfactory and thereby serve to enhance the operational safety and utility of the aircraft. Those that fail result in relative minor costs to repair the model, no one is injured, and valuable experience is gained.

Since the first radio-control system was developed in 1944, there have been many improvements in electronic control, recording equipment, and operating technique. For all precise, laboratory-type analysis of straightaway control and stability in calm water, it is now customary to utilize a fast-acting bang-bang type of radio control. As it is desired to accelerate to getaway on a straight course in smooth water with the principal controls treated as independent variables, the elevators, rudder, flaps, and throttles are fixed at their test settings and the bang-bang control is connected to only the ailerons and ignition so that slight corrections to maintain wings level and the "blipping" of port or starboard engines to maintain course are the only variables involved. Just after getaway, all ignition is cut and the run is terminated. For the more elaborate evaluations of seaworthiness, maneuverability, rough-water take-offs, and flight, the original seven-channel proportional control system is used which provides simultaneous precision control of the elevator, rudder, ailerons, and independent throttles, in addition to selective ignition cut-off.

(*2*) *Catapult Launching.*—While the radio-controlled powered model is used for the majority of conventional hydrodynamic tests, it is not desirable or necessary to employ these elaborate models for routine investigations of landing stability and impact. Through the use of a catapult and open-water conditions, where the heading and air speed relative to the water may be selected to match the conditions under study, the engines and radio equipment can be removed and their weight replaced with more elaborate recording equipment. For these tests the aerodynamic controls are preset prior to each run. Through the use of an accurate velometer to record wind velocity and direction, of calibrated catapult spring tension, and of a little experience in presetting the controls, it is possible to execute precise landings at any attitude and rate of sink within the capabilities of the aircraft configuration being tested.

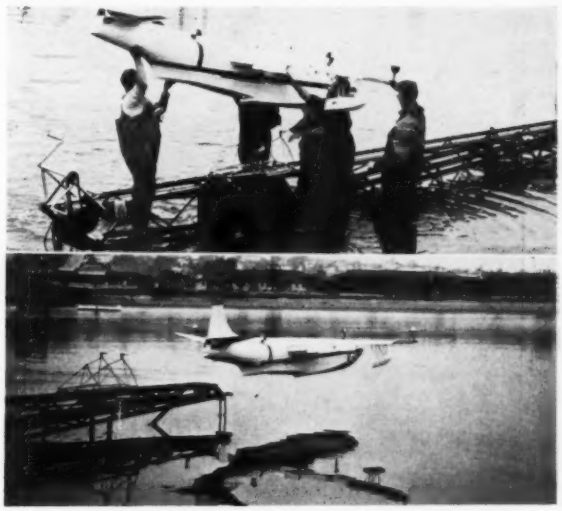

FIG. 12. The XP5Y-1 free-flight catapult model during landing stability tests at the estuary.

Fig. 12 shows a typical catapult launching of the $^1/_{10}$ scale XP5Y-1 catapult model. The equipment shown is a standard 30-ft. A-2 target drone catapult, which is capable of launching a 100-lb. model at a flight speed of 60 ft. per sec. The catapult is portable, and its heading and height above the water may be varied at will. For these tests, the models carry elaborate internal instrumentation, in addition to the phototheodolyte tracking equipment previously mentioned. When the lanyard is pulled, an inertia switch automatically turns on a 16-mm. gun camera mounted within the model. This camera records a continuous record of trim, air speed, relative wind, bow, step and sternpost contact with the water, and impact acceleration. Fig. 13 is a picture of the internal instrumentation installation.

The free-body catapult technique is used to obtain smooth- and rough-water landing stability, aerodynamic ground effect, landing impact, and water-looping characteristics. Here again, particularly in the study of rough-water impact and water-looping, attitudes and conditions that would never be attempted full scale can be thoroughly studied at no risk. Only in this way can the full capabilities of a new design be determined.

(*3*) *Bridle Tow.*—The bridle tow technique is used to good advantage in all those cases where it is desired to obtain resistance data, position the model close to the observer for detail study, determine preliminary stability and spray information from small survey models incapable of carrying power plants or radio, and constant speed running under controlled conditions. This procedure most nearly approaches the towing-tank method except for the fact that selection of heading, wind, and sea is still available to the operator.

Fig. 14 illustrates a typical bridle tow installation for a small jet-propelled research model. The launch tows the model through the thrust line from the end of

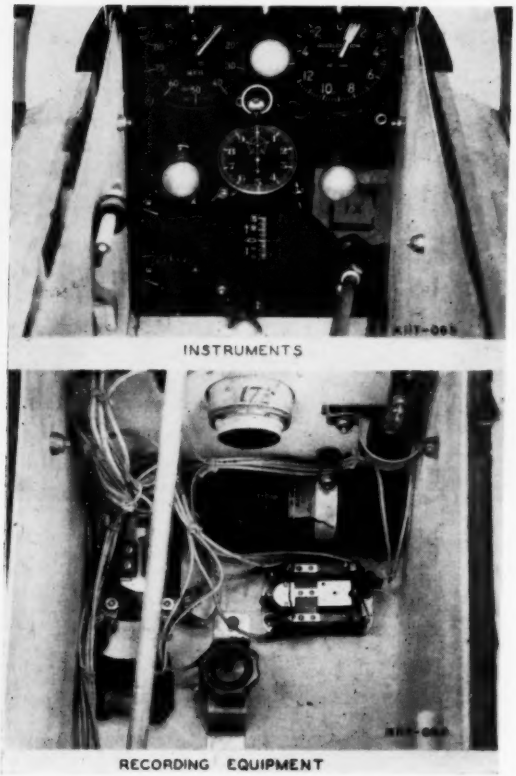

FIG. 13. Internal instrumentation in the XP5Y-1 dynamically similar free-flight model.

a towing boom that contains a resistance dynamometer. The instrumentation box on the launch contains the resistance and water-speed indicators, which are recorded by a camera. Just below the recording instruments, the model being towed is framed in an aperture that allows the image of the model, the shore line, resistance, and water speed to be recorded simultaneously. In this manner, complete trim tracks with a record of spray and resistance at any speed may be determined.

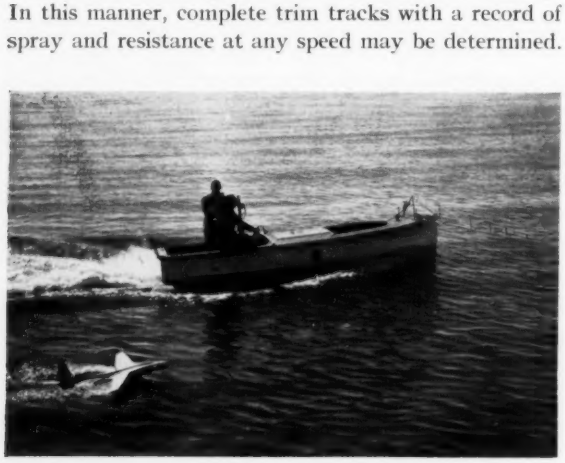

FIG. 14. The bridle tow technique developed by the Convair Hydrodynamics Laboratory for the testing of small unpowered survey models of supersonic water-based aircraft prior to self-propelled tests.

Also, the condition of the sea at the moment is permanently recorded for future reference or evaluation. This system is extremely versatile and is used extensively during early survey investigations of a radical new design prior to constructing the large and more elaborate powered models.

(4) *Free Launch.*—The testing procedures discussed thus far have dealt primarily with gasoline engine propeller-driven models or models containing no power plants at all, such as the catapult and bridle tow techniques. To date, no large jet-propelled radio-controlled models have been tested comparable to the large propeller-driven types previously discussed. This is due to several causes: (1) suitable jet units for producing sufficient scale thrust have not been available; (2) the study of jet-propelled water-based aircraft is so new and the problems so diversified that emphasis has been put on a large number of small survey models in an effort to establish basic design criteria; and (3) the inherently greater speeds of the jet-propelled aircraft have posed the tremendous problem of speeding up pilot and servo reaction times beyond the point that is now critical. It will be recalled that, in dynamic similarity, time varies as the square root of the scale, so that on a $^1/_{10}$ scale model events occur roughly three times faster than the equivalent full-scale event. Operation in confined areas with extremely fast aircraft rapidly multiplies the problems of control reaction.

It was inevitable, however, that, if water-based aircraft were to keep pace in the aviation field, means to obtain powered dynamically similar research data, comparable to that being secured on conventional-type seaplanes, must be developed. The first step in this direction was the availability of an efficient, lightweight pulse-jet engine. Aeromarine Company of Vandalia, Ohio, produces such engines in $4^1/_2$ and 30 lbs. of thrust per unit ratings. For additional versatility, the $4^1/_2$-lb. thrust units may be manifolded together to produce an $8^1/_2$-lb. thrust unit.

With suitable power plants available, detailed studies of the many mounting, manifolding, cooling, and associated problems were started. Obviously, it was desirable to check out these many jet-power development problems with as small and economical a model as possible in view of the attrition rate anticipated. It was at this point that the free launch technique was evolved. It was reasoned that excellent results are attained from catapult launchings with preset controls and that with the accelerations anticipated the take-off run would closely approximate a catapult launching. In the original attempts at free launch, the fuel was metered closely, and progressively longer bursts were permitted as the trim and balance of the model proved satisfactory. This technique resulted in some exciting, inadvertent uncontrolled take-offs and climbs to high altitudes when combinations of factors became ideal; and, as a consequence, a light, single-channel, radio-controlled fuel shutoff had to be developed. This shutoff

mechanism was so light that it could be easily installed in small 15-lb. models utilizing a pair of 4½-lb. thrust units for propulsion. This complete installation, including radio, fuel tank and cutoff, and a pair of engines, is shown in Fig. 15.

Subsequent testing with the single-channel control of fuel shutoff has proved so successful that the free launch technique has become a standard test procedure, in spite of the fact that it was originally a temporary measure to expedite the development of jet power in free-body models. Completely satisfactory runs can be made up to getaway, and in many cases short straightaway flights may be accomplished in complete safety to the model. Inasmuch as the speed and acceleration of the towing launch is limited, this free launch procedure allows the survey studies of small models to be carried out to high planing speeds and actual getaway. When the larger jet-propelled models are constructed, it is likely that free launch techniques will be used with, possibly, the addition of aileron control and that the weight saved will be put into internal instrumentation.

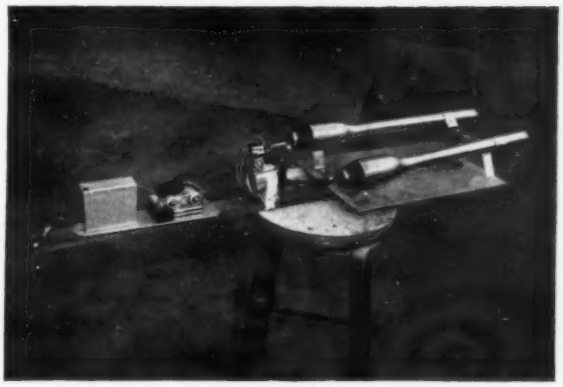

FIG. 15. The radio gear and power-plant installation for self-propelled radio-controlled models of jet-powered water-based aircraft.

EXPERIMENTAL RESEARCH

It has been pointed out in this paper that the introduction of the dynamically similar model and its associated research techniques has been responsible for breaking the period of passive development in the water-based aircraft field. This has been accomplished by supplementing design criteria established by the rule of thumb and gradual process of experience by full-scale trial and error, with fundamental information obtained from a direct experimental approach where all of the parameters affecting hydrodynamic performance and efficiency appear as configuration or test variables subject to evaluation and accurate study. While many new design criteria have been established since introduction of the dynamically similar research technique, it is not within the scope of this paper to present each study in detail. Rather, it is believed more desirable to discuss at some length the several broad basic concepts that contributed the most toward the radical resurgence of water-based aircraft.

Hull Loading

The load that must be supported by a flying boat hull or seaplane float is probably the most fundamental variable in the design of a water-based aircraft, since it fixes the basic overall size of the hull. This corresponds to the selection of the basic wing area for a new airplane design. As you recall, the wing area required is fixed by the maximum lift (or load) coefficient that can be attained and the landing speed desired. In effect, this determination is strictly a low-speed, maximum load-carrying criterion and is largely independent of the high-speed characteristics of the aircraft in question. As a matter of fact, as much research effort and expense has been devoted to developing the low-speed load-carrying ability of wings as any other phase of aerodynamic investigation. The analogy between basic hull size and wing area selection is interesting, inasmuch as both are a measure of the maximum load-carrying ability at the lowest speed where sustention is by dynamic forces. In the case of the hull, this speed occurs in the transition region between displacement and planing and is known as the hump. Just as aerodynamic stability and control reach a critical value near the stall and must be considered in the final selection of aerodynamic configuration, so do hydrodynamic stability and control reach their most critical values in the region of the hump. In addition, the water-based situation is further complicated by the generation of gravitational wave systems that reach their peak intensity in this region. The bow wave and spray produced often limits the loading to a value much lower than theoretically possible because of physical inundation of power plants and cockpit enclosures. It can be seen that the major problem facing the seaplane designer in his effort to make radical improvements in seaplane efficiency was to increase hull loading materially while at the same time to suppress the spray formation and maintain adequate stability. As mentioned previously in our discussion of Froude Number, these critical low-speed functions lent themselves admirably to investigation by dynamically similar models.

In hydrodynamic analysis, the hull loading is expressed in terms of the nondimensional load coefficient C_Δ, which is based on the hull beam as the characteristic dimension and is equal to Δ/wb^3, where Δ is the load on the hull in pounds, w is the density of water in pounds per cubic foot, and b is the maximum hull beam in feet. As the load on a hull continually varies with speed, due to the varying proportion of load carried by the wing, it is customary to compare hulls at their static load coefficient $C_{\Delta_0} = \Delta_0/wb^3$, where Δ_0 is the total gross weight of the airplane.

Up to and including the seaplanes in general use during World War II, the ratio of the length of the hull to

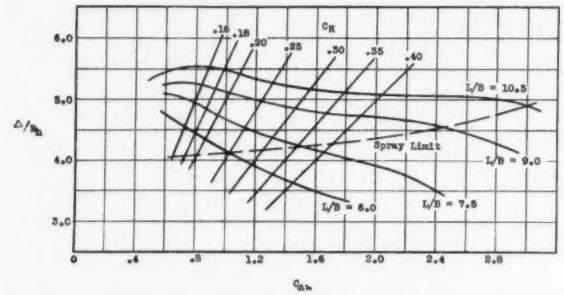

FIG. 16. Influence of length-beam ratio on the hull load and load-resistance ratio at hump speed. (Hydrodynamic effect of length-beam ratio; 25° deadrise.)

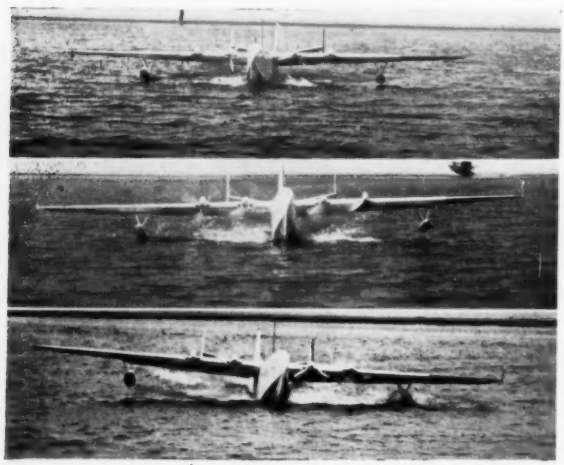

FIG. 17. The 21-ft. span powered dynamic research model from which the XP5Y-1 high L/b hull was developed. Note procedure employed for determining influence of power on spray.

the beam was usually between 5.0 and 6.0, and it was well established that for such proportions it was valid to use C_{Δ_0} as a basis for loading comparison, regardless of size. In other words, any two seaplanes having the same general proportions of length and beam generally had the same hydrodynamic characteristics if the values of C_{Δ_0} were equal. Over a considerable period of years, experience had indicated a range of load coefficients to which could be assigned certain general characteristics of operation. For example, it was established that, for exceptionally good seaworthiness, short take-off time (low resistance), and clean running, a beam should be selected which gave a static load coefficient of not over $C_{\Delta_0} = 0.65$. Likewise, it was generally accepted that the upper limit of hull loading was around $C_{\Delta_0} = 1.0$.

To select the beam for a contemplated design, the designer had a choice, therefore, between these limits of load coefficient. With the condition of the ratio of length to beam more or less constant, it was established by experience that, increasing the load coefficient, (a) increased the trim and resistance at hump speed, (b) increased the height and intensity of the spray, (c) decreased the range of hydrodynamic stability during take-off, (d) had little effect on landing stability, (e) decreased low-speed maneuverability and control, and (f) reduced air drag by reducing the size of the hull relation to the load. Item (b) or (e) usually determined the maximum load that was practical for the design in question.

Length-Beam Ratio

As discussed in the introduction to this paper, the first promising approach to the problem of loading was revealed in the reports covering the experiments conducted by the Germans on high length-beam ratio hulls.[2, 3] In aerodynamics, one of the fundamental measures of efficiency of a wing is the L/D or ratio of lift to drag. In hydrodynamics, this applies to a hull as well and is the ratio of load supported to the resistance, or Δ/R. A cross-plot of the German data, where the Δ/R at the hump, for various values of length-beam ratio, was plotted against hull load coefficient, showed the remarkable trend reproduced in Fig. 16. On this curve has been plotted the maximum spray limit considered acceptable by the Germans, and it is interesting to note the great area available for improvement in loading and Δ/R over the upper limit of conventional seaplane practice represented by the $L/b = 6.0$ curve. It appeared from study of these data that increasing length-beam ratio materially reduced the energy going into the parasitic gravitational wave-making system. This, in turn, reduced spray and resistance, both factors being conducive to higher allowable loadings.

As these data dealt primarily with the effect of length-beam ratio on resistance, with the inference that spray reduction would also be realized, it was apparent that many more data, particularly regarding quantitative results of spray and stability, were required before correlated design parameters could be established. A broad research program consisting of a family of 21 dynamically similar model configurations, covering length-beam ratios of 6, 8, and 10, was initiated simultaneously by Convair, using free-body radio control, and Stevens Institute, employing the Stevens' method. The radio-controlled model with an L/b of 10.0 hull installed is shown in Fig. 17. These tests confirmed the fact that length-beam ratio has a powerful influence on the allowable magnitude of C_{Δ_0} which may be used and still maintain satisfactory spray. It was found also that, as the L/b ratio increases, the limiting value of C_{Δ_0} increases in direct proportion to the function L^2b, resulting in a smaller beam and, hence, overall size of hull for a given load. This was a fundamental finding of immense importance, for it established the fact that hulls of varying length-beam ratio will have equivalent resistance and spray characteristics if a load coefficient similar to C_Δ, but based on L^2b instead of b^3, is held constant. Dr. Davidson, of Stevens Institute of Technology, first presented this relationship[6] and calls this coefficient K_2, which is equal to Δ/wL^2b. Figs. 18(a–c)

FIG.

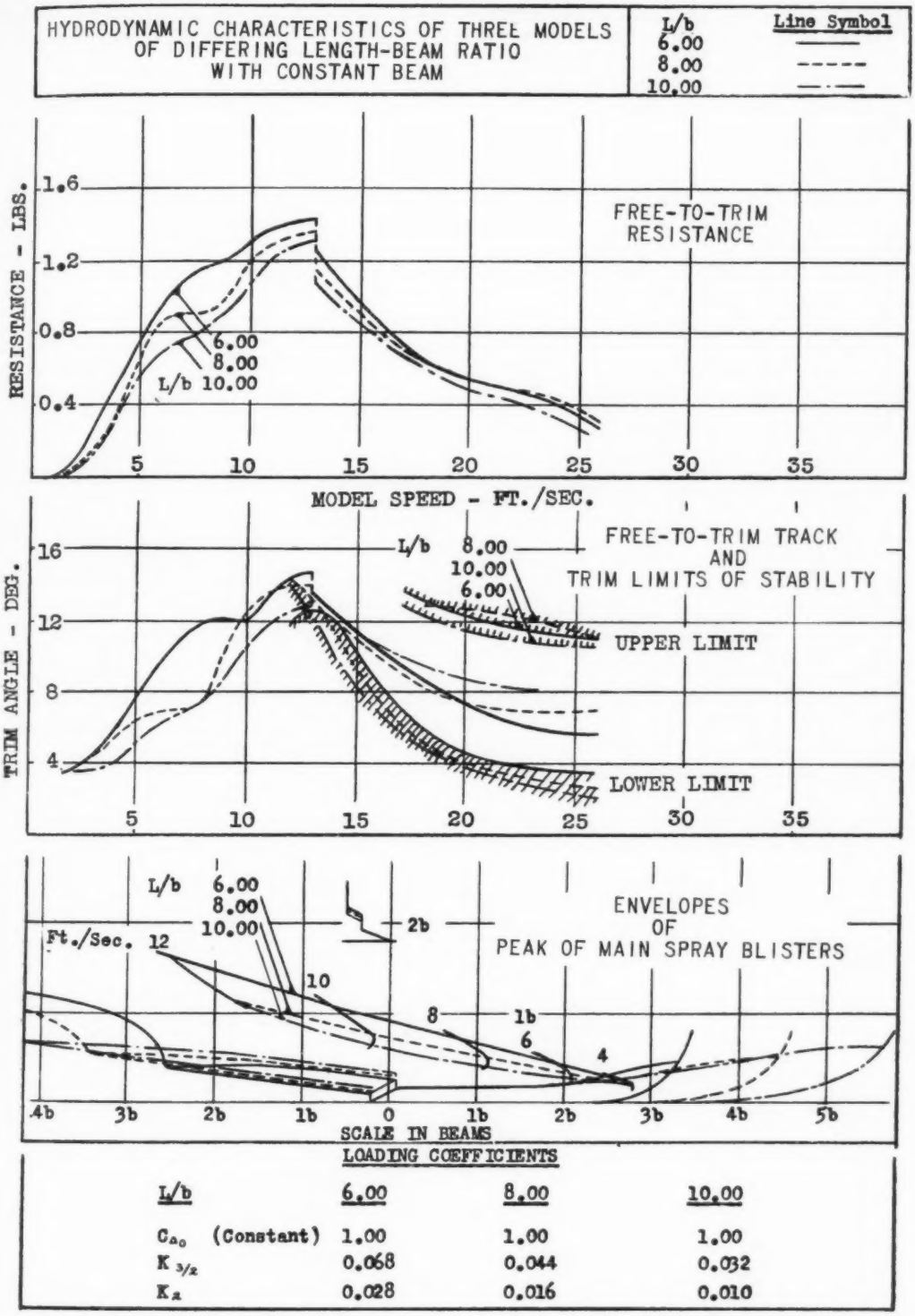

FIG. 18a. Influence of length-beam ratio on loading, resistance, stability, and spray while maintaining constant beam. Length increased by proportional increase in transverse section spacing along the keel.

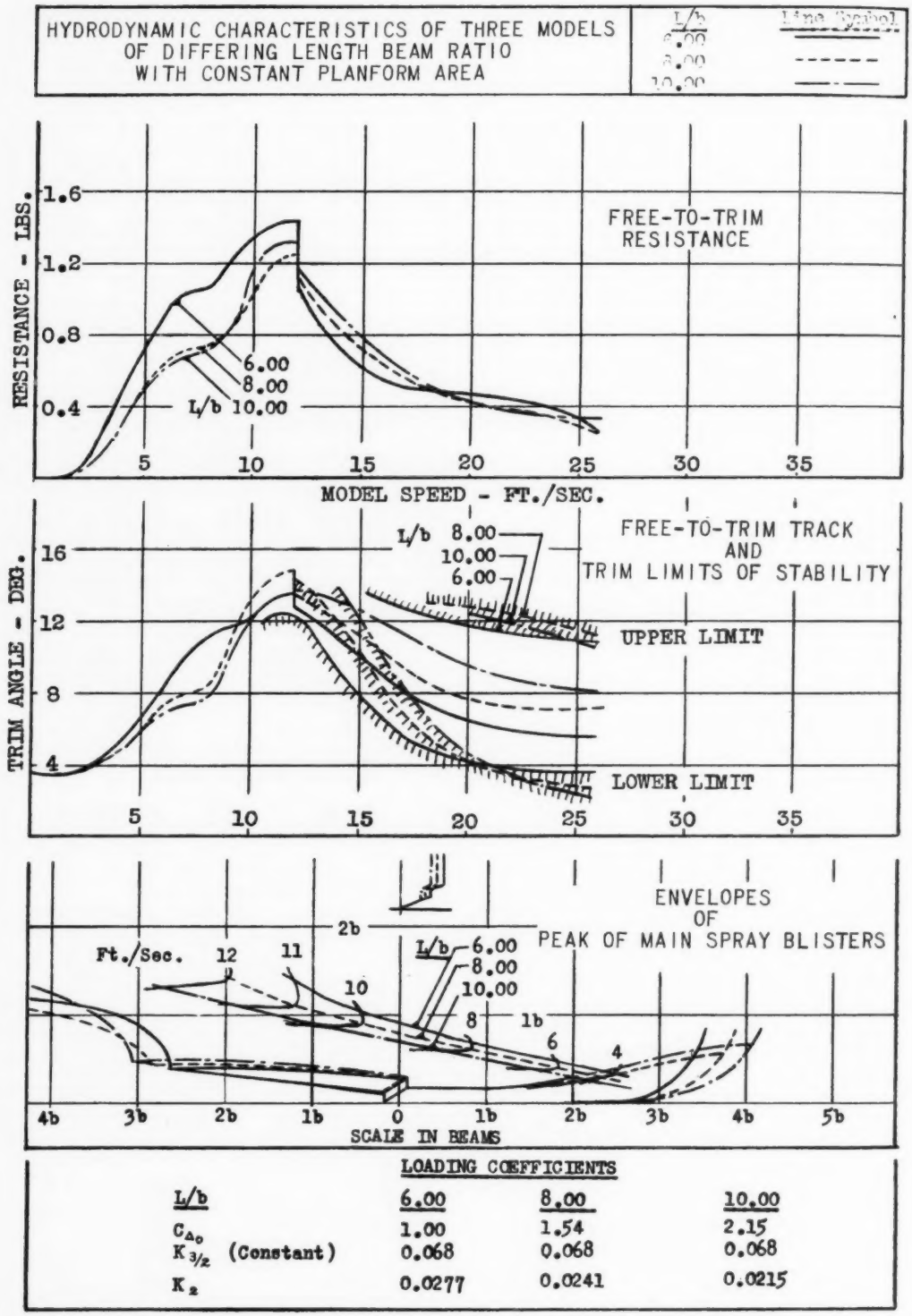

LOADING COEFFICIENTS			
L/b	6.00	8.00	10.00
C_{Δ_0}	1.00	1.54	2.15
$K_{3/2}$ (Constant)	0.068	0.068	0.068
K_2	0.0277	0.0241	0.0215

FIG. 18b. Influence of length-beam ratio on loading, resistance, stability, and spray while maintaining constant plan-form area (Lb = constant).

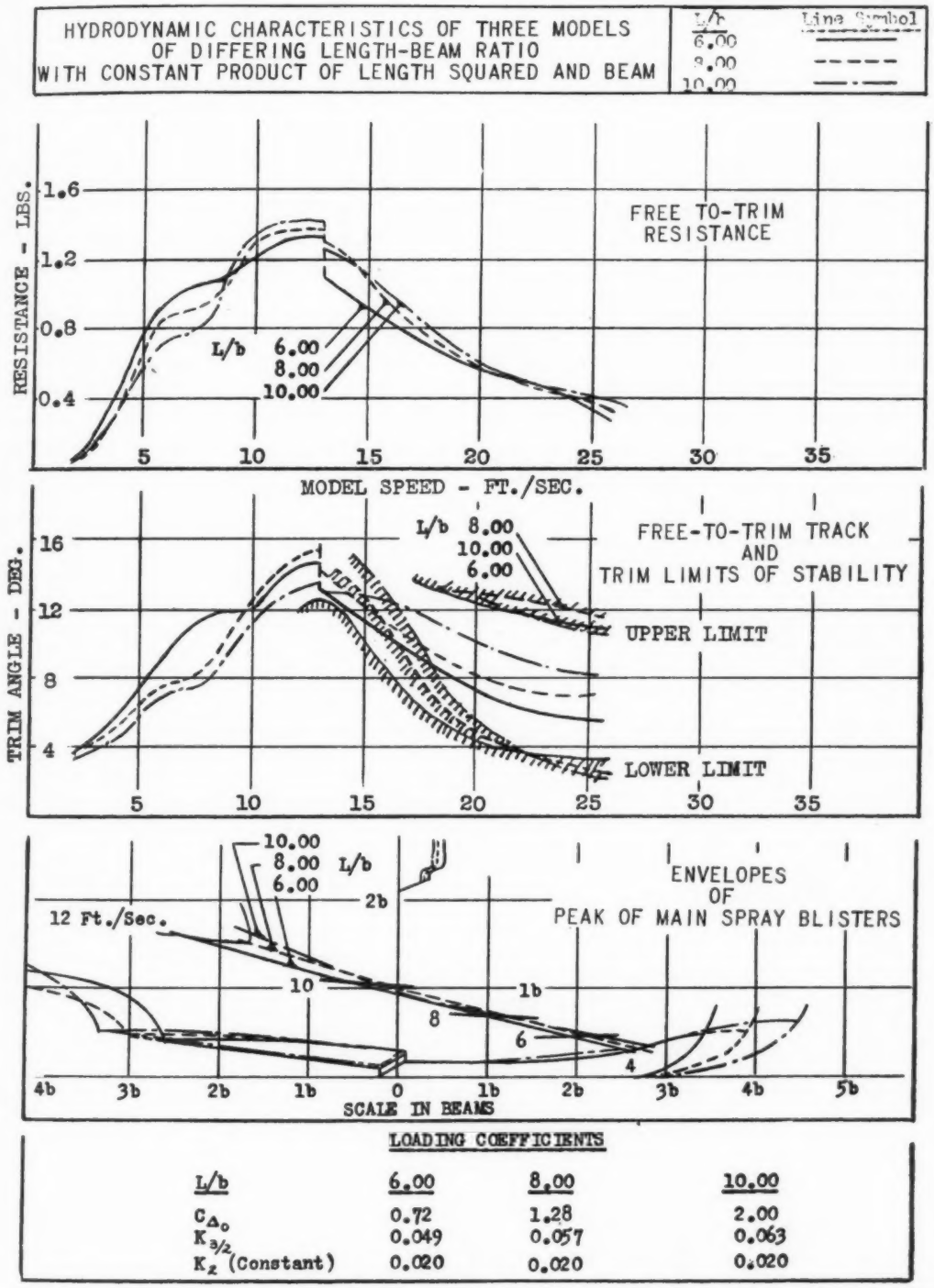

FIG. 18c. Influence of length-beam ratio on loading, resistance, stability, and spray while maintaining the product of (length)^2 × beam constant (L^2b = constant).

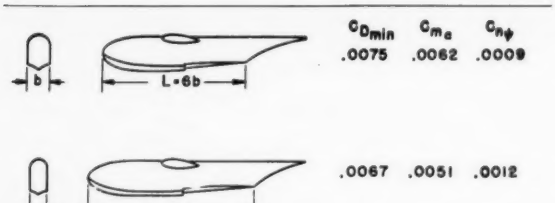

FIG. 19. Influence of length-beam ratio on aerodynamic characteristics from the N.A.C.A. high L/b hull series.

summarize the results of this fundamental finding which first established a definite design relationship between the influence of length-beam ratio and physical hull size.

Fig. 18a shows the academic relationship of load, resistance, spray, and stability versus length-beam ratio where the beam is held constant and the length is increased by a proportional increase in station spacing along the keel. Here, it will be noted that marked reductions in spray and resistance are realized as the length increases, indicating that the higher length hulls can carry much more load; or, for constant loading, the size can be reduced while maintaining constant resistance and spray. In an effort to determine how much the load can be increased or the size reduced with increasing length-beam ratio, a comparison is made in Fig. 18b where the hull plan-form area is maintained constant as the L/b varies. Here again, the length is varied by proportional increase in hull spacing, while the beam is decreased at the same time to maintain plan-form area constant. It will be noted that the relationship is still conservative, indicating that further increase in load, or less size, can be tolerated for equivalent resistance and spray.

In Fig. 18c we find the relationship previously mentioned where the product of L^2b is maintained constant. Resistance and spray are observed to collapse substantially to a common curve, regardless of length-beam ratio, when compared at a constant value of the K_2 load coefficient proposed by Davidson. By studying the relations presented in Figs. 18a, 18b, and 18c, it can be noted that the influence of the planing bottom length has been progressively weighed against the effect of the beam. It is also apparent that, in the case of constant plan form, increasing length-beam ratio would maintain a hull of constant volume and decreasing frontal area, whereas, using the L^2b relationship, which has now been completely substantiated by all research facilities, a progressive decrease in hull volume, in addition to a rapid decrease in beam required, is made possible. This latter characteristic is of considerable importance from an aerodynamic standpoint, as indicated in Fig. 19, where it is noted that there is a 20 per cent reduction in hull drag in going from a length-beam ratio of 6.0 to 12.0.

To assist the designer in the selection of a beam for a new design and to establish clearly the interrelationship of loading, seaworthiness, and size, the selection chart of Fig. 20 has been prepared. This chart gives the relationship of static load coefficient (C_{Δ_0}) to length-beam ratio for equivalent hulls based on the L^2b or K_2 standard of loading. The introduction of this relationship between length and beam is of extreme importance to the designer, since a knowledge of its effects on the hydrodynamic characteristics of a hull permits greater choice in size and shape of hull to arrive at optimum dimensions to satisfy a particular design specification. Also, it permits data obtained on any one hull of a family to be expanded to any other hull of which it is a parent. It will be noted in Fig. 20 that certain values of K_2 have been assigned their characteristic influence on spray height; this characteristic, we have noted, is the fundamental loading design criterion. In the initial stages of a design, a value of $K_2 = 0.018$ should be assumed and a value of $K_2 = 0.022$ should never be exceeded, since the design loading of a new seaplane invariably increases somewhat as the design progresses.

It should be pointed out that, in addition to obtaining a much smaller and cleaner hull aerodynamically, increasing L/b ratio at constant K_2 will materially reduce the hull weight because of reduction in hull volume and beam. Structural studies[7, 8] indicate that this weight trend continues up to a L/b ratio of approximately 15.0 or slightly higher. With further increase in L/b ratio, the hull bending moments become increasingly higher because of the added length of hull, and this trend begins to reverse. Just where this reversal occurs and how rapidly it will build up depend upon many functions related to the specific design. It is interesting to note that increasing length-beam ratio from 6.0 to 12.0 has resulted in reductions as high as 8 per cent in structural weight of the hull for equal performance.[8]

Forebody Proportion

Throughout this discussion of the parameters affecting hull loading, the conventional standard of using the overall length of the planing bottom, which includes both forebody and afterbody, is employed to determine the L/b ratio of the hull. It is important to note, however, that the forebody is the principal load-carrying portion of the hull and that in many respects it bears the most direct analogy to the wing of an airplane, being responsive to unit loading, proportion or aspect ratio, pressure distribution, and section. Being a surface that derives its lift from operation on the surface of a medium, it depends upon those dynamic forces that normally act on the lower surface of a wing

at a finite angle of attack rather than the fluid circulation resulting from total submergence in a fluid. In spite of the loss of lift due to absence of circulation, the fact that it is operating in a fluid of approximately 800 times the density of air results in extremely great lift for nominal area. As a consequence of the high density of water and resulting high unit pressures, release in energy at the boundaries of the surface creates violent turbulence in the form of waves and spray; this must be controlled. As spray is the principal characteristic influencing the load that may be carried and since this characteristic is fundamentally a low-speed function, where the forebody wetted length is a maximum, it is reasonable to assume that it is the length of the forebody that furnishes the predominate influence in the overall length-beam ratio of the hull.

This assumption was investigated by Parkinson,[9] of the N.A.C.A., by correlating all existing full-scale and model information with respect to forebody fineness. Parkinson's analysis indicates that, when the static load coefficient, C_{Δ_0}, is plotted against forebody length-beam ratio, L_f/b, on a logarithmic scale, seaplanes having similar spray characteristics lie along straight lines having equations of the form $C_{\Delta_0} = k(L_f/b)^2$, where k has the following values:

Excessive spray	0.0975
Heavy, but acceptable for overload	0.0825
Satisfactory for normal operation	0.0675
Extremely light spray	0.0525

It will be noted that Parkinson's k is of the same order as Davidson's K_2, shown in Fig. 20, indicating that the factor L^2b is the correct fundamental characteristic for comparing equivalent hulls.

Most successful seaplane designs have incorporated a forebody length that varies from 55 to 60 per cent of the total planing bottom. Variations greater than this range have not proved entirely satisfactory, particularly from a stability standpoint. Research has shown that, where the above proportions of forebody and afterbody are maintained, either Davidson's K_2 or Parkinson's k will give substantially the same design load criterion. There has been a strong trend in modern seaplane research to separate the forebody and its functions from the afterbody and to treat these basic planing surfaces separately. This line of attack has resulted in the development of the planing tail and long afterbody form of hull. These types have shown some promise

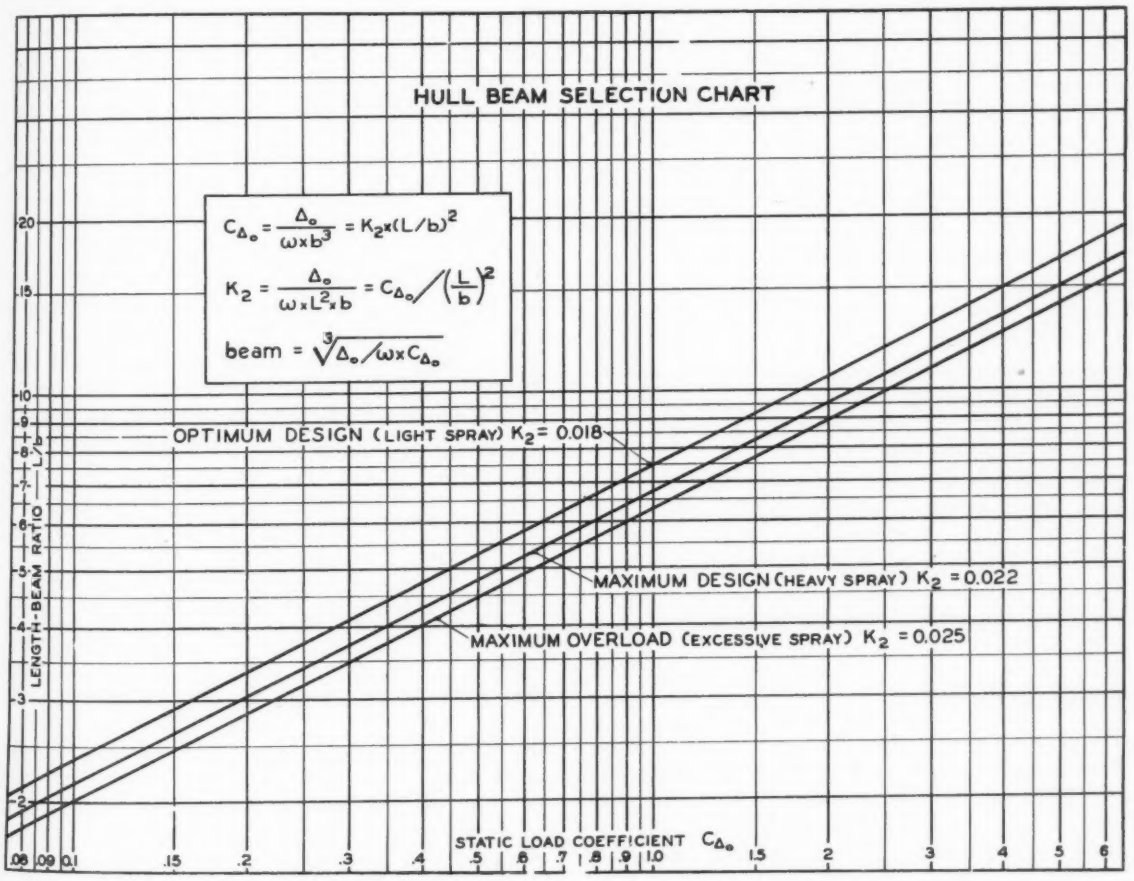

FIG. 20. Hull beam selection chart giving the relations between length-beam ratio and load coefficient for constant values of K_2 (L^2b = constant).

with regard to certain specific characteristics; however, evidence has shown that there are sufficient numbers of interdependent parameters to preclude the listing of completely independent criteria. While rigorous procedures for such a segregation may be developed in time in the laboratories, it is desirable for the designer to think of the planing bottom as a coordinated unit and to use the overall K_2 as a load criterion. He should keep in mind that, when comparing the load capacity of hulls of abnormal afterbody proportion, the additional length of afterbody over and above standard proportions contributes nothing to the characteristics that have been attributed to length-beam ratio in this paper. This is justified by the fact that it is the forebody that carries the load and generates the wave system, while the afterbody is merely a trimming device and the longer afterbodies are invariably set at a higher afterbody keel angle so that their effectiveness is still just the equivalent of the standard shorter afterbody. Serious inconsistencies will result if the total length of these abnormal hulls is used to determine the hull's L/b ratio for comparison with standard forms.

The selection chart of Fig. 20 has been set up for the standard hull proportion. For hulls of abnormal afterbody length, an equivalent length-beam ratio, L'/b, must be employed in all cases where length-beam ratio is used as a standard of comparison. The effective planing length, L', is the length that would result when the forebody of the hull in question is assumed to be 58 per cent of the total length, as in the expression $L_f = 0.58L'$, where L_f is the actual forebody dimension and L' is the total effective length for comparative purposes.

All of the parameters discussed thus far in this section have dealt with the fundamental problem of increasing the load-carrying capacity of a hull. Earlier in our discussion of hull loading, we found that, for years, established practice had dictated a design static load coefficient of $C_{\Delta_0} = 0.65$ with an absolute maximum of $C_{\Delta_0} = 1.0$, above which any further loading would increase resistance, spray, instability, or lack of maneuverability to unsatisfactory values. From our study of Fig. 20 we see that, through the results of dynamic model research, the powerful influence of length-beam ratio as a basic design parameter has made available to the designer as much as 300 per cent increase in this critical value with no loss of hull efficiency or seaworthiness.

Hydrodynamic Stability

Established design criteria, prior to the introduction of high length-beam ratio as a fundamental parameter, indicated that increasing the static load coefficient beyond a $C_{\Delta_0} = 1.0$ would increase trim, resistance, spray, and instability to unacceptable values. We have seen from Figs. 18 and 20 that, through the introduction of length-beam ratio as a basic design parameter, the major problem of greatly increased hull loadings was impressively solved with an actual overall improvement in trim, resistance, and spray. Stability, however, has been another story and has been purposely overlooked so far in this discussion because of the specialized research programs required for its solution. In returning to Figs. 18, it will be noted that, while resistance, spray, and trim could be controlled by appropriate length-beam ratio for a given increase in loading, the lower trim limit of stability increased rapidly, with any increase in loading, to values that would not permit a stable take-off to be made. During the early phases of length-beam ratio research, this persistent deterioration of stability promised to nullify all other gains in this development. Conventional hydrodynamic stability had been none too good, and it was desirable to improve this characteristic; further compromise with stability could not be tolerated.

To review for a moment, it will be recalled that, during the take-off of a seaplane, after it has passed the hump speed, the planing trim must remain between two limiting curves of trim or it will encounter instability known as "porpoising." Porpoising is a cyclic oscillation in pitch and rise, and, if allowed to persist, it may become divergent and result in destruction of the seaplane. These limiting curves are shown in Figs. 18 and consist of an upper and lower limit of trim, versus speed, between which the aircraft will be stable. It has been established that the upper trim limit is dependent upon, and is a function of, the afterbody form and position. The lower limit depends upon forebody lines. To satisfy the stability requirements for take-off, the designer must provide an adequate range of stable trims to accommodate the normal trim range of the hull when operating anywhere within the design range of center-of-gravity loading, flap, and elevator position. If the trimming moment available between the limiting curves is not sufficient to accommodate all normal operation conditions, the aircraft must be placarded for limited operation or modified to broaden the limits. It is obvious that the critical condition for upper limit is with maximum aft center of gravity, flaps up, power off, and up-elevator—or, in other words, conditions that produce a bow-up moment and, hence, high trim. Conversely, lower limit is critical for conditions that produce bow-down moments. Inasmuch as low trim is desirable from a resistance and spray standpoint and the take-off conditions of high power and flap deflection produce strong bow-down moment, the lower limit is of major importance during the heavily loaded take-off run. As we have noted, the lower limit of trim increases steadily to higher trims with increase in loading, which is directly opposed to the desired trend. It was found in the past that only moderate increases in loading raised the lower trim limit to such an extent that it was found necessary to reduce flap and limit the forward range of center-of-gravity position in order to take off. This, in turn, increased the resistance and left little up-elevator

control available, which further decreased the load-carrying ability of the aircraft.

With the large increases in loading made available through the employment of high length-beam ratio, this trend approached intolerable proportions, which indicated that a stable take-off would be impossible. Inasmuch as the forebody of the hull determines the position and form of the lower trim limit, an extensive research program was initiated in an effort to isolate the forebody design parameters associated with lower limit stability. All there was to go on at the start of these studies was the knowledge that for satisfactory planing stability the forebody contacted by the water during planing must be free of all longitudinal curvature. At speeds just beyond the hump, where lower limit porpoising is most likely to be encountered, this wetted length had been found to extend approximately one and one-half beams forward of the step. As a consequence, it had been rigid design practice to maintain an area of constant deadrise for approximately one and one-half beams forward of the step. This region was commonly called the "forebody flat."

It will be recalled that, when the first families of hulls of increased length were investigated, the hulls were lengthened by proportionate increase in spacing between the transverse stations of a good low-length parent hull. This was an obvious method and was believed to be sound inasmuch as the flat was rigidly maintained, and actually lengthened, by this procedure. It was noted, however, that the static trim of these long hulls was increasing to extremely high values, indicating that the buoyant power of the forebody was increasing at a greater rate than the afterbody. In an effort to reduce this power by reducing the volume through increased deadrise forward of the step, it was found that the lower limit of stability also improved with reduced forebody effectiveness. In attempting to bring the lower trim limit down by cutting further back into the flat with increased deadrise, curvature was introduced and improvement ceased.

With this new trend to work on, it gradually became apparent that, while longitudinal curvature must be eliminated from the planing bottom ahead of the step, this need not be accomplished by maintaining a constant transverse section but could be a warped surface of varying deadrise so long as the longitudinal elements of this surface were straight lines for one and one-half beams forward of the step. Upon establishing the basic fact that the trim at which lower limit instability is encountered is dependent upon the linear rate of change of deadrise, or forebody warping, in the planing area, it became a relatively simple procedure to set up design criteria that would provide adequate stability for the various combinations of length-beam ratio and loadings previously established. Fig. 21 gives the linear variation of deadrise forward of the step in degrees per beam of forebody length required to give adequate lower limit stability for various forebody lengths. The degree of warping given in Fig. 21 extends for only one and one-half beam-lengths forward of the step, at which point the buttock lines may then curve as gradually as possible to the deadrise required at the bow for the suppression of spray.

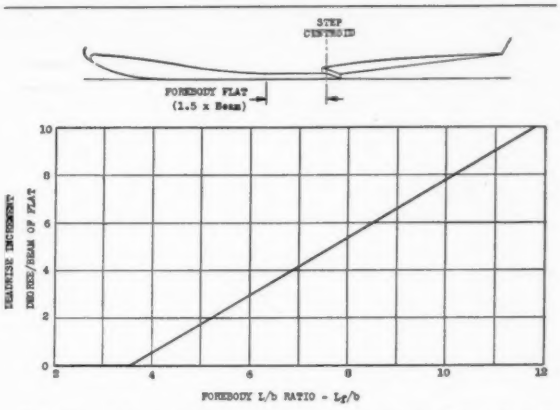

FIG. 21. Linear variation of deadrise forward of the step in degrees per beam of forebody length to maintain lower limit stability with increase in length-beam ratio.

It will be noted in Fig. 21 that for a forebody L_f/b ratio of 3.5, which corresponds to an overall L/b ratio of approximately 6.0 for a hull of conventional proportions, the forebody flat has a zero rate of warp in degrees per beam, resulting in a flat area of constant deadrise which conforms to the old rule-of-thumb concept.

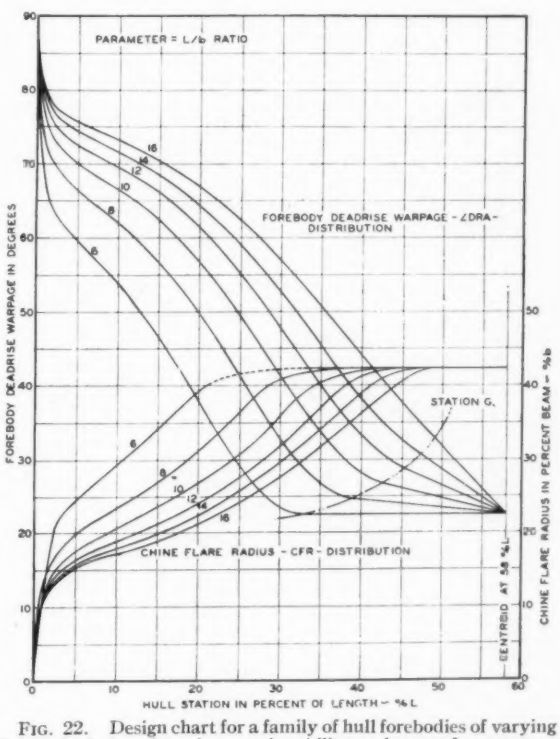
PARAMETER = L/b RATIO
FOREBODY DEADRISE WARPAGE - ∠DRA - DISTRIBUTION
STATION G.
CHINE FLARE RADIUS - CFR - DISTRIBUTION
FOREBODY DEADRISE WARPAGE IN DEGREES
CHINE FLARE RADIUS IN PERCENT BEAM - %b
CENTRBD AT 58 %L
HULL STATION IN PERCENT OF LENGTH - %L

FIG. 22. Design chart for a family of hull forebodies of varying L/b ratio designed to give equal stability and spray for constant values of K_2 (L^2/b = constant).

However, for all L_f/b ratios greater than this value, the gradual increase in warping, to maintain equivalent lower limit trim, results in no region of constant forebody deadrise. These criteria have been incorporated into the plot of Fig. 22 which shows the forebody deadrise variation for a typical family of hulls of varying length-beam ratio and standard proportion of forebody to afterbody. The dashed curve, labeled "Station G" in Fig. 22, represents the one and one-half beams of forebody flat or linear warp that must be free of longitudinal curvature. It is apparent that, because of the long forebody flat required for the lower L/b ratios, it is difficult to warp the bottom to the high sharp lines required at the bow without utilizing rapid buttock curvature. As the L/b ratio increases, it becomes increasingly easy to obtain the deadrise angles of the order of 70° to 80° at the bow which are desired from a seaworthiness and low bow buoyancy standpoint. It is this easing of the forebody lines with increasing length which results in the major increases in performance attributed to high L/b ratio hulls, and the proper use of linear warp will assure this performance without loss of stability.

It was stated earlier in this paper that no attempt would be made to cover the entire scope of research investigations since the advent of dynamic model testing. These detailed findings are adequately reported in applicable scientific literature and do not warrant repetition here. However, the discussions of increased hull loading contained herein are believed to be of such fundamental importance that any other studies may be classified as refinement and extension to this basic concept of modern hull design. Through the application of the broad design criteria summarized in Figs. 20 and 21, we find the water-based aircraft potential suddenly expanded many times. While detailed exploration and refinement will continue unabated, the foundation for a revitalized program of modern high-speed seaplane development is well established.

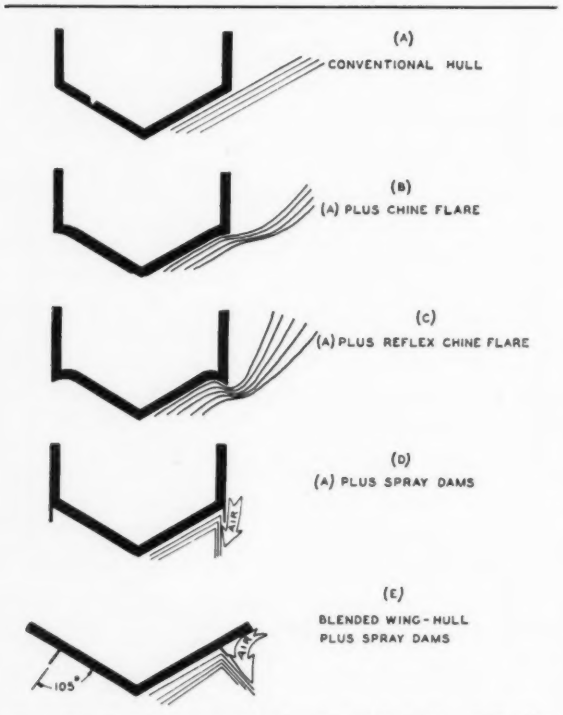

FIG. 23. Local spray suppression devices including the highly effective spray dam utilized on high-speed jet-propelled water-based aircraft.

Spray Control

During the course of the research investigations that have been discussed thus far and prior to the realization of the full impact that the high length-beam ratio studies would have on the course of seaplane design, many other approaches to the problems confronting water-based aircraft development were initiated. Inasmuch as excessive quantities of drenching spray was the principal factor restricting the loading of conventional seaplanes, the major effort was directed toward the development of improved spray suppression devices. Even though these studies proved to be of little value at the time and were eventually dropped in favor of full exploitation of the much more promising influence of length-beam ratio, one development during this period was found much later to have a most profound influence on the future course of transonic and supersonic water-based aircraft. For this reason, it is appropriate to discuss briefly localized spray suppression.

A conventional "V" bottom planing surface, such as shown in Fig. 23(A), is not satisfactory for a seaplane hull due to the great height to which the spray climbs upon leaving the chine; therefore, most conventional hulls have incorporated some form of transverse curvature in the bottom called chine flare, as indicated in Figs. 23(B) and 23(C). The most effective control through the use of flare is obtained by a generous radius that terminates with a horizontal or slightly downward direction at the chine, as shown in Fig. 23(B). If a radius that is too small or abrupt is used, only the layer of water adjacent to the hull is acted upon, and the inertia of the unaffected mass carries it by the local curvature with little change in direction. Likewise, if exaggerated flare is employed, as in Fig. 23(C), the adjacent layer will actually rebound from the unaffected mass and rise higher than if no flare at all had been used.

During the course of isolating the effect of downward deflection of the chine, a simple expedient was employed which consisted of attaching a metal strip to a hull without flare, such as shown in Fig. 23(A), and then progressively deflecting this strip and recording the spray height. As one would expect, there was no improvement beyond a few degrees of deflection at which

point the reflected spray became progressively worse, as in the condition of Fig. 23(C). As in the course of many research investigations, the study was continued "ad absurdum" for the record and upon approaching a nearly vertical position, as shown in Fig. 23(D), an interesting phenomenon occurred in that marked reductions in spray height were noted.[10] It was concluded from these tests that the increased effectiveness is due to the sharp intersection of the strip with the bottom, which in effect acts as a dam. This powerful effect is lost where the lowered chine is faired by using reflex flare or a fillet of any nature. Because of obvious structural limitations, this highly effective vertical spray strip, shown in Fig. 23(D), was not considered feasible for application to conventional hulls and for many years remained principally of academic interest only.

With the advent of jet propulsion, which has encouraged the development of extremely low, blended-hull type configurations for seaplanes, the vertical spray strip (or spray dam as it is now commonly called) has shown great promise in being able to control effectively all spray without the necessity for any flare, any sharp chine, or, in fact, any discontinuity of any sort on the basic hull bottom. This form of spray dam has been extensively developed by the Consolidated Vultee Hydrodynamics Laboratory, and in a broad sense this device, as illustrated in Fig. 23(E), has made the high-speed jet-propelled water-based aircraft feasible. Because of the inherent unbroken form of the aerodynamically smooth blended-hull configuration, the spray dam feature may be maintained structurally by placing the structural depth to the dam on the outer face where it can be adequately tied into the continuing hull structure. By rotating the spray dam wedge about the upper inboard edge, it may be retracted flush in flight, leaving an unbroken blended wing and hull contour. The spray dam obtains its effectiveness by violently agitating the main spray blister and thoroughly mixing it with air. This aerated mass is deflected downward with great force in a high-velocity jet. Because of the high content of entrained air, this water mass penetrates the free water surface with little or no rebound or reflection, and the high velocity curtain generated effectively retains the mass of water not directly contacted by the dam.

An impressive example of the spray dam in operation is shown in the photograph of Fig. 24, which was taken at the speed for maximum spray. Here it will be noted that the bow wave is completely suppressed, and at no point does the spray reach a height greater than the dam itself. At a comparable loading, the bow wave on a conventional hull, utilizing a sharp chine and flare, would be going completely over the wing in the example shown. In combination with the powerful influence of high length-beam ratio, the application of the spray dam principle on a completely smooth aerodynamic form of high critical Mach

FIG. 24. The forebody of a supersonic water-based aircraft showing the action of the retractable spray dams at the speed for maximum spray and the relationship of the jet air intakes.

Number has made possible jet-propelled supersonic water-based aircraft incorporating hydrodynamic seaworthiness and stability comparable to the best propeller-driven seaplanes of conventional form. Security prevents a detailed analysis of the parameters and factors uniquely associated with the transonic and supersonic water-based problem. However, it suffices to say that recent hydrodynamic research, based upon the fundamental principles discussed in this paper, has placed the water-based aircraft high on the priority list of National Defense once again.

CONCLUSIONS

Extensive refinement of the dynamically similar model and its associated research techniques during the years since 1938, when this new concept was first introduced in this country, has established the science of seaplane hydrodynamics on a par with contemporary fields of aeronautical research and development. Extensive experience has indicated that the fundamental laws of dimensional similitude can be matched or compensated to the extent that accurate determination of the complex integrals of unrestrained motion, in discontinuous media, are possible with an economical and rapid experimental procedure.

One of the greatest contributions of the dynamic research program to the advancement of water-based aircraft design has been the establishment of hull length-beam ratio as a fundamental design parameter. Through the application of this basic criterion and its dependent variables, the hull loading of seaplanes has

been increased over 300 per cent with an accompanying improvement in performance, seaworthiness, and stability. Design charts have been prepared which provide the designer considerable latitude in selection of optimum characteristics with a high measure of confidence.

Through a new blended wing-hull design approach, coupled with the development of an extremely effective spray suppression device known as a "spray dam," it has been possible to water-base idealized high Mach Number aerodynamic forms without compromising hydrodynamic performance, seaworthiness, or stability. By utilizing jet power, it has been demonstrated that water-based aircraft can be developed into efficient and dependable transonic and supersonic aircraft.

It appears reasonably certain that established research techniques, such as discussed in this paper, can keep the fundamental design of water-based aircraft abreast of current aerodynamic development. It is just as reasonable to assume that, without this unique development, water-based aircraft today would be relegated to nothing more than auxiliary craft, used in those few instances where operation on water became mandatory for a particular specialized mission.

Many of the principles and new design criteria discussed in this paper appear for the first time in the Convair XP5Y-1. This high-speed seaplane, constructed for the U.S. Navy, not only embodies exceptional hydrodynamic performance but also holds the distinction of being the first multiengined aircraft in the United States to be powered with propeller turbines. The technical mating of these two outstanding developments is indicative of the new role of water-based aircraft.

References

[1] Stout, Ernest G., *Experimental Determination of Hydrodynamic Stability*, Journal of the Aeronautical Sciences, Vol. 8, No. 2, p. 55, December, 1940.

[2] Sottorf, W., *The Design of Floats*, N.A.C.A. T.M. No. 860, April, 1938.

[3] Fuller, R. D., *German Experimental Tank Tests for Model Floats*, DVL 1, 1a, 7, 8, 17, 18, and 19 (Translation of German Reports FB 156, FB 351, FB 444, and FB 650), Consolidated Vultee Report No. ZH-016, September, 1943.

[4] Stout, Ernest G., *Development of Precision Radio-Controlled Dynamically Similar Flying Models*, Journal of the Aeronautical Sciences, Vol. 13, No. 7, p. 335, July, 1946.

[5] Welge, V., *Radio Control of Model Flying Boats*, Proceedings, Institute of Radio Engineers, Waves and Electrons Section, Vol. 35, No. 5, May, 1947.

[6] Davidson, Kenneth S. M., and Locke, F. W. S., Jr., *General Tank Tests on the Hydrodynamic Characteristics of Four Flying Boat Hull Models of Differing Length-Beam Ratio*, N.A.C.A. A.R.R. No. 4F15, 1944.

[7] Fefferman, R. L., *The Influence of Length-Beam Ratio on the Structural Weight of Seaplane Hulls*, CVAC Report No. ZS-088, October 13, 1947.

[8] Benscoter, Stanley U., *Estimate of Hull-Weight Change with Varying Length-Beam Ratio for Flying Boats*, N.A.C.A. R.M. No. L7F24, August, 1947.

[9] Parkinson, J. B., *Design Criterions for the Dimensions of the Forebody of a Long-Range Flying Boat*, N.A.C.A. A.R.R. No. 3K08, 1943.

[10] King, Douglas A., and Mas, Newton A., *Effects on Low-Speed Spray Characteristics of Various Modifications to a Powered Model of the Boeing XPBB-1 Flying Boat*, N.A.C.A. A.C.R. No. L5F07, 1945.

Notice to Contributors

Manuscripts submitted for publication *must* be double- or triple-spaced originals. There should be wide margins on both sides of the sheets and triple spacing around formulas to allow for the marking of directions for the printer.

Original drawings (jet black India ink on white paper or tracing cloth) should accompany the manuscript. (*Blueprints are not acceptable.*) Photographs *must* be on glossy white paper. The smallest lettering on 8- by 10-in. figures should be no less than 1/4 in. high.

Only the simplest formulas should be typewritten; all others should be carefully written in pen and ink. The difference between capital and lower-case letters and Greek symbols should be clearly distinguished.

See Inside Back Cover of this issue for further details.

Application of Frequency-Response Analysis to Aircraft-Autopilot Stability

CHARLES L. SEACORD, JR.*
Georgia Institute of Technology

SUMMARY

A description of the frequency-response method for analyzing an aircraft-autopilot combination is given, and examples are used to demonstrate various aspects of the method and the criteria for stability. In particular, one numerical example illustrates the method of calculating the aircraft response curves. The procedure for determining the autopilot response curves is outlined. The use of Nyquist diagrams for the analysis of frequency-response data is discussed, and Nyquist diagrams for the example are correlated with the separate frequency-response curves. The complete longitudinal and lateral equations of motion for an aircraft are presented, and, in addition, certain simplified equations for special cases are included. Sources of information concerning the aerodynamic derivatives are given in tabular form.

INTRODUCTION

SEVERAL RECENT PAPERS, among them references 1 and 2, have been written concerning the use of a combination graphical-analytical method for determining the stability of a given autopilot-aircraft combination. This frequency-response method, as it is called, is based upon principles much used in electrical engineering, but only during the last 3 years have these principles widely been applied to aircraft stability problems. The method makes it possible to use measured autopilot characteristics, along with calculated aircraft characteristics, to determine the stability of the combination. It is the possibility of using actual test data on autopilots, thus eliminating the use of complicated and inaccurate equations for representing the autopilot, which constitutes one advantage of the frequency-response method over the direct analytical solution of the equations of motion. Another advantage is that various hypothetical autopilot systems may be studied by its use with less labor than with the complete analytical solution.

The ever increasing use of autopilots makes it desirable for the aeronautical engineer to understand the methods used in autopilot work and the limitations of such methods. The object of this paper is to present, in an elementary manner and with as little specialized mathematics as possible, the procedure to be followed in the solution of a problem in autopilot analysis.

The basic equations of motion of an aircraft are presented, along with some simplified forms, and an example of the computation of the response curves is given in detail, including references for the aerodynamic derivatives used. The method for obtaining autopilot response curves is given, and the use of both the aircraft and autopilot response curves in determining the stability of the combination is illustrated. The procedure for converting the frequency-response data into Nyquist diagrams and the criteria for using the Nyquist diagrams are also given.

In Appendix A, an idealized case is used to illustrate the similarity of the results obtained through the use of frequency-response curves, Nyquist diagrams, and the simultaneous solution of the aircraft and autopilot equations of motion.

SYMBOLS

R_a	= amplitude of aircraft oscillation produced by unit amplitude oscillation of control surface
R_p	= amplitude of aircraft oscillation required to produce unit control surface deflection by autopilot
ϵ	= phase angle in degrees between δ and ψ, positive when ψ is ahead of δ; subscripts are a, aircraft; p, autopilot
ϕ	= angle of roll, rad.
ψ	= angle of yaw, rad.
β	= angle of side slip, $\beta = \tan^{-1}$ (sideslip velocity$/V$), rad.
δ	= control deflection, rad.; subscripts refer to a, aileron; e, elevator; r, rudder
γ	= angle between flight path of center of gravity and horizontal, rad. NOTE: Subscript 0 indicates steady-state value; symbol with no subscript indicates increment from steady state
δ_0	= amplitude of sinusoidal forcing control motion, rad.
r	= yawing angular velocity $d\psi/dt$, rad. per sec.
p	= rolling angular velocity $d\phi/dt$, rad. per sec.
t	= time, sec.
ω	= angular frequency of oscillation, rad. per sec.
ω_c	= angular frequency at which $\epsilon_a = \epsilon_p$—that is, at which hunting oscillation may occur
m	= mass of aircraft, slugs
k_X	= radius of gyration about longitudinal principal axis, ft.
k_Z	= radius of gyration about vertical principal axis, ft.

Received August 15, 1949.

* Instructor, Daniel Guggenheim School of Aeronautics. Now Aerodynamics Engineer, Fort Worth Division, Consolidated Vultee Aircraft Corporation.

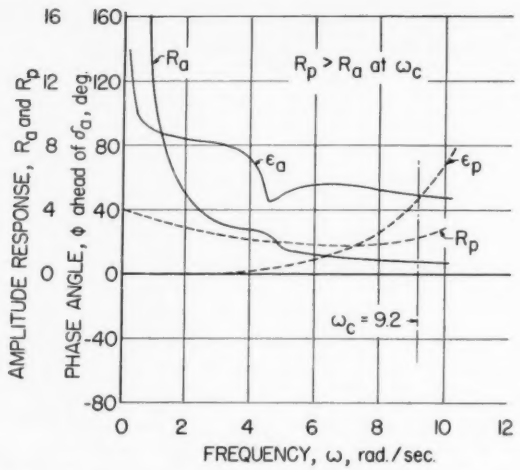

FIG. 1. Frequency response curves in roll for a typical aircraft and autopilot. Curves indicate stability.

η	= angle between principal longitudinal axis and flight path, positive when principal axis is inclined above flight path, deg.
b	= span of aircraft, ft.
S	= reference wing area of aircraft, sq.ft.
V	= velocity along flight path, ft. per sec.
q	= dynamic pressure, lbs. per sq.ft.
ρ	= air density, slugs per cu.ft.
D	= differential operator d/dt
i	= imaginary unit, $i = \sqrt{-1}$
C_n	= yawing moment coefficient, yawing moment/qsb
C_l	= rolling moment coefficient, rolling moment/qsb
C_Y	= sideforce coefficient, sideforce/qs
C_{n_β}, C_{l_β}, C_{Y_β}	= $\partial C_n/\partial\beta$, $\partial C_l/\partial\beta$, $\partial C_Y/\partial\beta$
C_{n_r}, C_{l_r}, C_{Y_r}	= $\partial C_n/\partial(rb/2V)$, $\partial C_l/\partial(rb/2V)$, $\partial C_Y/\partial(rb \div 2V)$
C_{n_p}, C_{l_p}, C_{Y_p}	= $\partial C_n/\partial(pb/2V)$, $\partial C_l/\partial(pb/2V)$, $\partial C_Y/\partial(pb \div 2V)$
C_{n_δ}, C_{l_δ}, C_{Y_δ}	= $\partial C_n/\partial\delta$, $\partial C_l/\partial\delta$, $\partial C_Y/\partial\delta$
$C_{n_{D\delta}}$, $C_{l_{D\delta}}$, $C_{Y_{D\delta}}$	= $\partial C_n/\partial(D\delta b/2V)$, $\partial C_l/\partial(D\delta b/2V)$, $\partial C_Y \div \partial(D\delta b/2V)$
K	= control gearing ratio of autopilot; at zero frequency, $\delta = K\psi$, $K\phi$
$P_a(i\omega)$	= vector ratio of output displacement motion to input control motion for aircraft, as a function of angular frequency
$P_p(i\omega)$	= vector ratio of output control motion to input displacement motion for autopilot
$KG(i\omega)$	= $P_a(i\omega) \cdot P_p(i\omega)$, see reference 2

FREQUENCY-RESPONSE METHOD

General Description

The frequency-response method of autopilot-aircraft analysis involves the use of four curves as shown in Fig. 1. These four consist of two pairs. One pair of curves describes what a forcing oscillation of the control surface (input) does to the motion of the aircraft (output). The other pair of curves describes how the autopilot moves the control surface (output) in response to the motion of the airplane (input). The two quantities plotted to describe each response are the amplitude ratio between the airplane motion and the control surface motion, R, and the phase angle, ϵ, between the airplane motion and the control surface motion. The relationship of the body motion both in amplitude and phase (time relationship) to the forcing control deflection depends solely upon airplane parameters. The relationship of the enforced control motion to the body motion both in amplitude and phase depends solely upon autopilot parameters. These response curves are usually determined for a range of frequencies from zero to about three times the natural frequency of the airplane. Both sets may be determined either experimentally or by use of equations of motion. Generally, the response of the airplane is calculated and the response of the autopilot is measured.

The response of the aircraft is obtained by calculation of steady-state solution of the equations of motion.[3, 4] The procedure involves the replacement of the differential operator D by a sinusoidal frequency variable "$i\omega$." This allows the response of the airplane per unit disturbance to be plotted as a function of the frequency of the periodic disturbance.

The response data for the autopilot are obtained by oscillating the autopilot at various frequencies and amplitudes and measuring the control or servo motion produced. In those cases where the control motion is not a sine wave, it is necessary to use some degree of approximation for an equivalent sine wave. The procedure for determining the equivalent sine wave is given in a separate section.

The two sets of curves on Fig. 1 were calculated and measured for a typical air frame and autopilot. They are used to determine stability as follows: The intersection of the ϵ curves is determined. This intersection, or critical frequency, determines the frequency at which a neutrally stable oscillation may exist. The values of the R curves at the critical frequency ω_c determine whether the oscillation can exist. That is, if, at the critical frequency, the R values are equal—i.e., the curves intersect at ω_c—then there will be a neutrally stable oscillation. If, however, R_p is greater than R_a, as in this example, the oscillation will be damped, and, if R_a is greater than R_p, instability will be indicated. The existence of a stable or an unstable oscillation is the only definite conclusion that can be drawn directly from the two sets of curves. By definition,[3, 4] the response curves are valid only for the condition of zero damping of the oscillation, and, therefore, if the R curves do not intersect at the same frequency as the ϵ curves, the ϵ intersection no longer determines the frequency of oscillation. This can be stated another way—if the airplane-autopilot combination is either stable or unstable, the basic response curves will indicate the fact but will not define the frequency or the damping of the oscillation.

Computation of Airplane Response Curves

As mentioned in the section above, the response curves for the airplane may be obtained by utilizing the equations of motion of the airplane to calculate the airplane motions in response to a sinusoidally varying control motion. The motion of an airplane is generally represented by a set of six differential equations.[5, 6] Because of symmetry, there will be a negligible amount of coupling between the lateral (rolling, yawing, and sideslipping) motions and the longitudinal (pitching, vertical, and forward) motions, provided the oscillations are small. Therefore, the equations may be divided in two sets of three each. In some special cases where simplifying assumptions may be made, it is possible to eliminate one or two of the equations. Examples of these simplified systems and the complete longitudinal equations are given in Appendix B. The general equations for lateral motion are given below:

Yawing moment equation:

$$\left[\frac{m}{qSb}(k_Z^2\cos^2\eta + k_X^2\sin^2\eta)D^2 - C_{n_r}\frac{b}{2V}D\right]\psi + \left[\frac{m}{qSb}(k_Z^2 - k_X^2)\cos\eta\sin\eta\,D^2 - C_{n_p}\frac{b}{2V}D\right]\phi - C_{n_\beta}\beta = C_{n_{\delta_a}}\delta_a + \left(C_{n_{\delta_r}} + C_{n_{D\delta_r}}\frac{b}{2V}D\right)\delta_r \quad (1)$$

Rolling moment equation:

$$\left[\frac{m}{qSb}(k_X^2\cos^2\eta + k_Z^2\sin^2\eta)D^2 - C_{l_p}\frac{b}{2V}D\right]\phi + \left[\frac{m}{qSb}(k_Z^2 - k_X^2)\cos\eta\sin\eta\,D^2 - C_{l_r}D\frac{b}{2V}\right]\psi - C_{l_\beta}\beta = \left(C_{l_{\delta_a}} + C_{lD\delta_a}\frac{b}{2V}D\right)\delta_a + C_{l_{\delta_r}}\delta_r \quad (2)$$

Sideforce equation:

$$\left[\frac{mVD}{qS} - \frac{W}{qS}\sin\gamma_0 - C_{Y_r}\frac{b}{2V}D\right]\psi - \left[\frac{W\cos\gamma_0}{qS} + C_{Y_p}\frac{b}{2V}D\right]\phi + \left[\frac{mVD}{qS} - C_{Y_\beta}\right]\beta = C_{Y_{\delta_a}}\delta_a + \left(C_{Y_{\delta_r}} + C_{YD\delta_r}\frac{b}{2V}D\right)\delta_r \quad (3)$$

The equations given above are written with the usual nondimensional coefficients, but the equations themselves are dimensional because the operator D implies differentiation with respect to time. The dimensional form was used because the resulting curves must be compared with the autopilot test curves that are obtained as functions of time or frequency. Examples of completely nondimensional equations may be found in references 7 and 8.

It will be noticed that there are two classes of terms in the equation—namely, mass and aerodynamic terms. The mass parameters may be obtained from a summation of the contribution of each part of the aircraft or by experiment. The experimental techniques are described in reference 9.

Aerodynamic Parameters.—The aerodynamic derivatives are divided into the static and the rotary derivatives. The static derivatives are those arising as a result of some angular displacement of the airplane in respect to the relative wind, while the rotary derivatives are those due to an angular velocity of the airplane referred to the air.

If extensive flight tests are excepted, the most accurate method of determining all of the static and certain of the rotary derivatives is by means of wind-tunnel tests. A tabulation of both lateral and longitudinal derivatives and methods of obtaining them are given in Table 1.

The lateral derivatives to be used in the example are given below, together with a brief note as to their source:

C_{n_β} = 0.2292, from wind-tunnel force tests

C_{l_β} = −0.1375, from wind-tunnel force tests

C_{Y_β} = −0.9168, from wind-tunnel force tests

C_{n_r} = −0.699, estimated by $C_{n_r} = C_{n_{r_{wing}}} + 2 \times (1/b)^2\, C_{Y_{\beta_{tail}}}$ (see reference 10)

C_{l_r} = 0.1719, estimated from reference 11

C_{n_p} = −0.0040, estimated by $C_{n_p} = -(C_L - C_{D_\alpha})/8$ from reference 5

C_{l_p} = −0.6429, estimated from reference 11

$C_{n_{\delta_a}}$ = −0.0146, from wind-tunnel force tests

$C_{l_{\delta_a}}$ = −0.0573, from wind-tunnel force tests

$C_{lD\delta_a}$ = 0, estimated from reference 64

$C_{Y_{\delta_a}}$ = 0, from wind-tunnel force tests

C_{Y_r} = 0, estimated from reference 76

C_{Y_p} = 0, estimated from reference 76

TABLE 1

Symbol	Name	Test Technique	Relative* Importance	References: Subsonic	References: Supersonic
$C_{n_{\dot\beta}}$	Yawing moment coefficient due to sideslip	Force tests, slope of C_n vs. ψ. NOTE: In wind tunnel $\beta = -\psi$	A	5, 11, 16, 17, 18, 19, 20, 22, 24, 25, 26, 28, 29, 30, 34, 35, 36, 37	27, 32, 33
$C_{n_{D\beta}}$	Yawing moment coefficient due to lag of sidewash or sidewise acceleration	See $C_{m_{D\alpha}}$	B	10, 64	27, 32, 33
C_{n_r}	Yawing moment coefficient due to yawing angular velocity (damping in yaw)	Oscillation tests or curved flow test in wind tunnel	A	5, 10, 11, 34, 40, 41, 42, 43	32, 33, 27
C_{n_p}	Yawing moment coefficient due to rolling angular velocity	Rotating model or rotating airstream tests in wind tunnel	A	5, 10, 11, 34, 42	27, 32, 33
$C_{n_{\delta_a}}$	Yawing moment coefficient due to aileron deflection	Force tests, slope of C_n vs. δ_a	B	18, 71	
$C_{n_{\delta_r}}$	Yawing moment coefficient due to rudder deflection	Force tests, slope of C_n vs. δ_n	A	70, 71	73, 80, 81, 82
$C_{n_{D\delta_r}}$	Yawing moment coefficient due to rudder angular velocity	No measurements reported	B	64	
C_{l_β}	Rolling moment coefficient due to sideslip	Force tests, slope of C_l vs. β	A	5, 11, 16, 17, 21, 22, 23, 24, 25, 26, 28, 29, 30, 35, 37, 39, 34	27, 31, 32, 33
C_{l_r}	Rolling moment coefficient due to yawing angular velocity	Oscillation tests or curved flow tests in wind tunnel	A	5, 10, 11, 34, 42, 43, 76	32, 33, 27
C_{l_p}	Rolling moment coefficient due to rolling angular velocity (damping in roll)	Rotating model or rotating airstream tests in wind tunnel	A	5, 10, 11, 29, 30, 34, 39, 42, 44, 45, 76	27, 32, 33, 46, 47
$C_{l_{\delta_a}}$	Rolling moment coefficient due to aileron deflection	Force tests, slope of C_l vs. δ_a	A	64, 71, 84, 85, 86, 87	73, 75, 79, 80, 81, 82, 83
$C_{l_{D\delta_a}}$	Rolling moment coefficient due to aileron angular velocity	No measurements reported	B	64	
$C_{l_{\delta_r}}$	Rolling moment coefficient due to rudder deflection	Force tests, slope of C_l vs. δ_r	B		
$C_{l_{D\delta_r}}$	Rolling moment coefficient due to rudder angular velocity	No measurements reported	C	64	
C_{Y_β}	Sideforce coefficient due to angle of sideslip	Force tests, slope of C_Y vs. β	A	5, 17, 22, 24, 29, 35, 36, 37, 38	27, 32, 33
$C_{Y_{D\beta}}$	Sideforce coefficient due to lag of sidewash or sidewise acceleration	No measurements reported	A	64	27, 32, 33
C_{Y_r}	Sideforce coefficient due to yawing velocity	Curved flow force tests	B	34, 77	27, 32, 33, 72
C_{Y_p}	Sideforce coefficient due to rolling velocity	Force tests in rolling flow or on rolling balance	B	34, 76, 77	23, 33, 72
$C_{Y_{\delta_r}}$	Sideforce coefficient due to rudder deflection	Force tests, slope of C_Y vs. δ_r	A	18, 21, 25, 26, 35, 70	79, 80, 81, 82
$C_{Y_{D\delta_r}}$	Sideforce coefficient due to rudder angular velocity	No measurements reported	B		
C_{L_α}	Lift coefficient due to angle of attack	Force tests, slope of C_L vs. α	A	35, 39, 30, 53, 67, 55, 68, 57, 78	27, 32, 33, 56
$C_{L_{D\alpha}}$	Lift coefficient due to lag of downwash or vertical acceleration	No measurements reported	B	64	
C_{L_u}	Lift coefficient due to change in velocity (Mach effect)	Cross-plot of C_L curves at various Mach Numbers	C Subsonic B Supersonic		32, 33
C_{L_q}	Lift coefficient due to pitching velocity	Curved flow force tests	B	34, 60, 74	32, 33, 72
$C_{L_{\delta_e}}$	Lift coefficient due to elevator deflection	Force tests, slope of C_L vs. δ_e	A	64, 71, 84, 85, 86, 87	73, 75, 79, 80, 81, 82
$C_{L_{D\delta_e}}$	Lift coefficient due to elevator angular velocity	No measurements reported	B	64	
C_{D_α}	Drag coefficient due to angle of attack	Force tests	A	29, 39, 59, 69, 78	27, 32, 33
$C_{D_{D\alpha}}$	Drag coefficient due to lag of downwash or vertical acceleration	No measurements reported	C		
C_{D_u}	Drag coefficient due to change in forward velocity	Force tests, cross-plot of C_D vs. M or velocity	C $M < 0.7$ B $M > 0.7$ B Supersonic		
C_{D_q}	Drag coefficient due to pitching velocity	No measurements reported	C		

* A—major factor; B—minor; C—usually negligible.

(*Continued on facing page*)

TABLE 1 (*Continued*)

Symbol	Name	Test Technique	Relative* Importance	References: Subsonic	References: Supersonic
$C_{D\delta_s}$	Drag coefficient due to elevator deflection	Force tests, slope of C_D vs. δ_s	B		
$C_{DD\delta_s}$	Drag coefficient due to elevator angular deflection	No measurements reported	C		
C_{m_α}	Pitching moment coefficient due to angle of attack (static longitudinal stability factor)	Force tests, slope of C_m vs. α	A	8, 29, 30, 34, 35, 39, 48, 49, 50, 51, 52, 53, 54, 57, 58, 59	27, 31, 32, 33, 56, 72
$C_{m_{D\alpha}}$	Pitching moment coefficient due to lag of downwash or vertical acceleration	Oscillation tests and curved flow tests	A	8, 62, 63, 74	31, 32, 33, 72
C_{m_u}	Pitching moment coefficient due to change in velocity (Mach effect)	Cross-plot of C_m curves at various Mach Numbers	C $M < 0.7$ B Supersonic B $M > 0.7$		32, 33, 72
C_{m_q}	Pitching moment coefficient due to pitching angular velocity (damping in pitch)	Oscillation tests or curved flow tests in wind tunnel	A	8, 10, 34, 49, 60, 61, 62, 63, 64, 65, 74	27, 31, 32, 33, 72
$C_{m_{\delta_e}}$	Pitching moment coefficient due to elevator deflection	Force tests, slope of C_m vs. δ_s	A	65, 54, 64, 70	73, 75
$C_{m_{D\delta_e}}$	Pitching moment coefficient due to elevator angular velocity	No measurements reported	B	64	
T_c'	Thrust coefficient	Flight tests, force tests	B	50	

* A—major factor; B—minor; C—usually negligible.

$C_{Y_{\delta_r}} = C_{n_{\delta_r}} = C_{l_{\delta_r}} = C_{n_{D\delta_r}} = C_{Y_{D\delta_r}} = 0$, no rudder on subject airplane

$m = 60.5$ slugs

$k_Z = 4.23$ ft., calculated

$k_X = 0.927$ ft., calculated

$\gamma_0 = 0$

$\eta = 0°$, calculated

$b = 11.5$ ft.

$q = 364$ lbs. per sq.ft.

$V = 586$ ft. per sec.

$S = 21$ sq.ft.

Calculations.—The values of the derivatives are substituted in the equations, giving the following results:

$$\left.\begin{aligned}
&(1)\quad (0.01231D^2 + 0.006859D)\psi + (0.00003935D)\phi - 0.2293\beta = -0.01146\delta_a \\
&(2)\quad (0.000591D^2 + 0.006308D)\phi - (0.0001686D)\psi + 0.1375\beta = -0.05730\delta_a \\
&(3)\quad 4.638D\psi - 0.2550\phi + (4.638D + 0.9168)\beta = 0
\end{aligned}\right\} \quad (4)$$

To utilize the frequency-response technique, it is necessary to know the response of the airplane to a sinusoidal control motion of constant amplitude and at various frequencies. The response can be computed by replacing the operator, D, by a frequency variable $(i\omega)$. This process, the derivation of which may be found in references 3 and 4, is described in detail in the steps given below.

Eqs. (1), (2), and (3) are a system of simultaneous equations in three unknowns, ϕ, β, and ψ. If the response in ϕ is desired, the equations are solved for ϕ by the method of determinants. In the numerical example, this yields:

$$\phi = \frac{\begin{vmatrix} 0.01231D^2 + 0.006859 & -0.01146 & -0.2292 \\ -0.0001686D & -0.05730 & 0.1375 \\ 4.638 & 0 & 4.638D + 0.9168 \end{vmatrix} \delta_a}{\begin{vmatrix} 0.01231D^2 + 0.006859D & 0.00003935D & -0.2292 \\ -0.001686D & 0.0005914D^2 + 0.006308D & 0.1375 \\ 4.638D & -0.2550 & 4.638D + 0.9168 \end{vmatrix}} \quad (5)$$

This can be evaluated and simplified to an expression of the ratio of ϕ to δ_a as an expression in D

$$\frac{\phi}{\delta_a} = \frac{10^{-8}(-327{,}300D^3 - 247{,}900D^2 - 6{,}858{,}000D)}{10^{-8}(3{,}378D^5 + 38{,}580D^4 + 90{,}440D^3 + 720{,}300D^2 + 23{,}070D} \quad (6)$$

At this point the substitution $D = i\omega$ is made, giving

$$\frac{\phi}{\delta_a} = \frac{(327{,}300\omega^2 - 6{,}858{,}000) + i(-247{,}900\omega)}{(3{,}378\omega^4 - 90{,}440\omega^2 + 23{,}070) + i(38{,}580\omega^3 + 720{,}300\omega)} \quad (7)$$

The expression in $i\omega$ can be simplified and rationalized to the form

$$\phi/\delta_a = A + iB$$

where

$$A = \frac{110{,}600\omega^6 - 4{,}320{,}000\omega^4 + 44{,}930{,}000\omega^2 - 1{,}582{,}000}{1{,}141\omega^8 + 87{,}740\,\omega^6 - 4{,}724{,}000\omega^4 + 51{,}460{,}000\omega^2 + 52{,}310} \tag{8}$$

and

$$B = \frac{1{,}179{,}000\omega^5 - 4{,}779{,}000\omega^3 + 493{,}400{,}000\omega}{\text{denominator of Eq. (8)}} \tag{9}$$

The quantities with which it is convenient to work are ϵ_a, the phase angle between ϕ and δ_a, and R_a, the absolute value of the ratio $\phi_{max.}/(\delta_0)_a$. These can be written as $\epsilon_a = \tan^{-1}(B/A)$ and $R_a = \sqrt{A^2 + B^2}$. By substituting the values of A and B into the expressions for ϵ_a and R_a, the formulas for R_a and ϵ_a as functions of ω (the frequency of the forcing control) are found. It is the graphs of these formulas that are plotted on Fig. 1. The form of the curves varies considerably, depending on the particular response being studied. As an example of the variation that may occur, the yaw response curves for the same aircraft used in the preceding example are shown in Fig. 2.

Determination of Autopilot Response Curves from Oscillating Table Tests

It was mentioned that the frequency-response analysis requires the use of two sets of curves. In the preceding section, the method of calculating the airplane response curves is given; in this section, the method is given for transforming autopilot test data into frequency response curves.

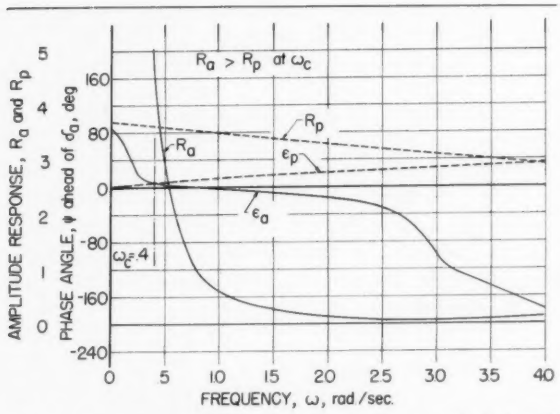
AMPLITUDE RESPONSE, R_a and R_p
PHASE ANGLE, ϕ ahead of δ_a, deg
FREQUENCY, ω, rad/sec.
$R_a > R_p$ at ω_c
R_p
R_a
ϵ_p
ϵ_a
$\omega_c = 4$
0 5 10 15 20 25 30 35 40
5 4 3 2 1 0
160 80 0 -80 -160 -240

FIG. 2. Frequency response curves in yaw for a typical aircraft and autopilot. Curves indicate instability.

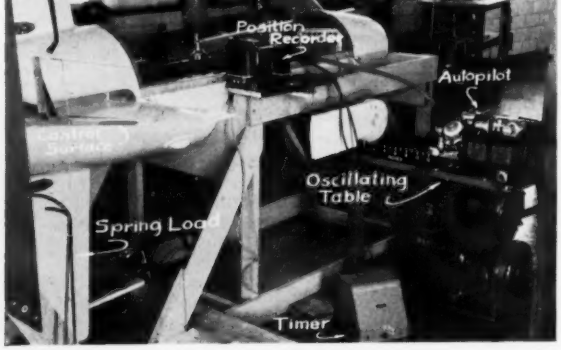

FIG. 3. Typical test setup for measuring frequency response of an autopilot.

The autopilot to be tested is placed upon the oscillating table, as shown in Fig. 3, and position recorders are set up to measure the position of the table and the position of the control surface. A block diagram of the setup is shown in Fig. 4. There may arise cases in which it is impossible to place the autopilot on the table and, at the same time, have it actuate the controls in the aircraft itself. In such cases it is necessary to measure the output of the servo without going through the control linkage or to build a mock-up of the control linkage. It can be seen in Fig. 3 that the control surfaces are spring-loaded in order to simulate aerodynamic hinge moments because the response of a servo sometimes varies considerably with the load on the servo. The traces of table position and control position, when recorded on film along with suitable timing marks, give a record much as shown in Fig. 5. It should be mentioned that the use of an oscillating table as a source of disturbance is not universal; if the sensing element of the autopilot does not respond to angular position, velocity, or acceleration or if the signal from the pickoff can be supplied by simpler means, then some means of disturbance other than the oscillating table is used.

Once the records are obtained, there are three methods of approximating the equivalent sine wave (as defined in reference 1) which may be used. These are listed below:

(1) If the control motion is a regular symmetrical wave (such as a square wave or sawtooth wave), it is possible to use the expression for the first harmonic of the Fourier series representation and from the dimensions of the control wave obtain the amplitude and phase of the harmonic.

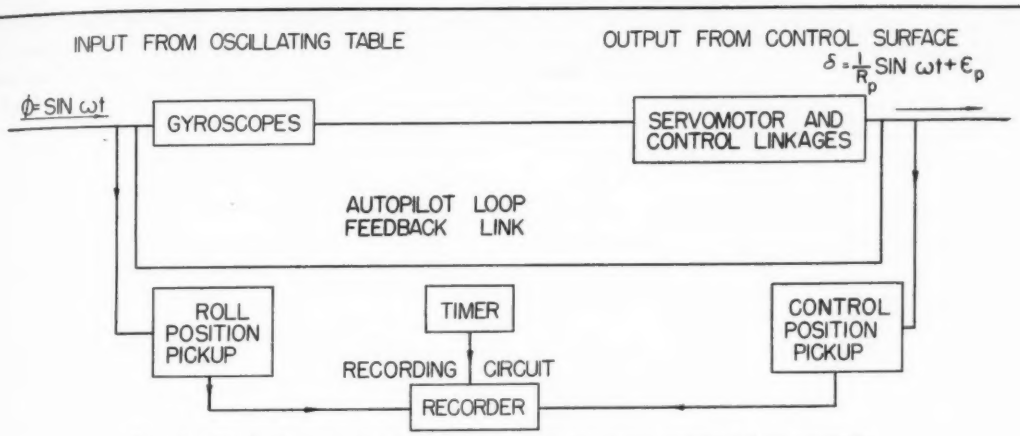

FIG. 4. Block diagram of setup for measuring frequency response of an autopilot.

TABLE A

(I) *Measure and compute the following quantities:*

Symbol	Description	Units
t_0	The period of the table oscillation	inches
F	Speed of recorder film	inches per second
F_1	Calibration of control record	degrees per inch
T	Period of table oscillation	second
$\omega = 2\pi/T$	Angular frequency	radians per second
A_1	Area under δ curve for one-half cycle (by graphical integration)	square inch
B_1	Area under curve of $\delta \cdot (\cos \omega t)$ by use of following table and graphical integration	square inch per second

t_0 in.	$t = (360/T)\, t_0$ deg.	$\cos \omega t$	δ in.	$\delta \cos \omega t$ in.

$t = 0$ at start of table cycle

(II) *The quantities desired are R_p and ϵ_p where:*

$$R_p = 1/\sqrt{A^2 + B^2} \text{ and } \epsilon_p = \tan^{-1}(B/A)$$

A and B are dimensionless amplitude factors of the in- and out-of-phase components of the control motion.

$$A = \frac{\omega \cdot A_1 \cdot F_1}{2F \text{ [amplitude of table oscillation (deg.)]}}$$

$$B = \frac{B_1 \cdot F_1}{\pi F \text{ [amplitude of table oscillation (deg.)]}}$$

(2) In cases where it appears that an exact answer is not needed (i.e., where a large stability margin exists), a sine wave may be faired through the control wave and the phase and amplitude read directly.

(3) If method (1) is not applicable or if the results using method (2) indicate the need for more accurate data, a graphic analysis may be made as outlined in Table A.

In those places where reference is made to the "area under a curve," the area is that between the curve and the zero axis of the curve, except in those cases where the curve is not symmetrical about the zero axis. This means that, if the control curve is symmetrical, the integration can be made without any manipulation, but, if the curve is not symmetrical, something must be done to obtain an axis of symmetry. The procedure used is to find a line parallel to the zero axis about which the curve will be symmetrical in area. This may be done by integrating the area between the record reference line and the control motion and then dividing by the length of one cycle. The result will be the distance from the reference line to the "equal area line." It has been found that the accuracy and speed of all integrations and measurements are increased by enlarging the records before the computation is started.

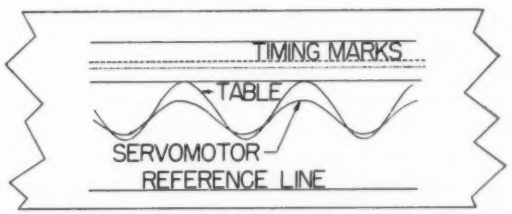

FIG. 5. Sample of record obtained from frequency-response test of an autopilot.

The above process must be carried out for records taken at a number of frequencies, and the values of R_p and ϵ_p must be obtained plotted against ω. A set of curves obtained from tests of a particular electric servo autopilot are shown in Figs. 1 and 2.

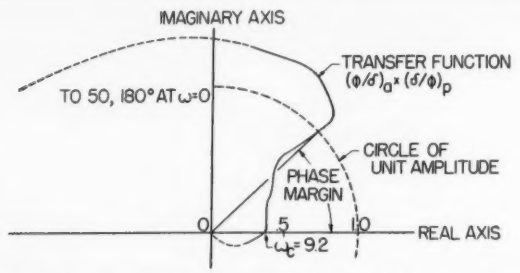

FIG. 6. Nyquist diagram for a typical aircraft and autopilot in roll. Diagram indicates stability.

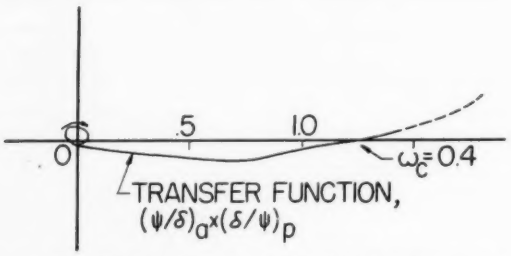

FIG. 7. Nyquist diagram for a typical aircraft and autopilot in yaw. Diagram indicates instability.

Analysis of Frequency Response Data

Plots of R and ϵ Versus ω.—In the previous sections there have been described the methods for obtaining frequency-response curves for both the aircraft and autopilot. As plotted on Figs. 1 and 2, the use of these curves, in determining the stability of the combined system will now be illustrated. On Fig. 1 it can be seen that at ω_c the value of R_p is about three times that of R_a, thus amply satisfying the condition for stability. In fact, the ratio of R_p to R_a is such that the motion following a disturbance will probably be well damped.

Another way of estimating the amount of damping is to consider the phase margin, or $\epsilon_a - \epsilon_p$, at the point where $R_a = R_p$. A value of plus 30° (when using the present convention), based chiefly on experience, is given in reference 12 as the amount of phase margin which will provide satisfactory damping. The concept of phase margin can be grasped more clearly from the Nyquist plots, which will be presented later.

Fig. 2 illustrates a case of indicated instability. At ω_c, the value of R_p is approximately one-half that of R_a, and the phase margin at the point where $R_p = R_a$ is negative. If the airplane were flown in this condition, it would exhibit an oscillation of increasing amplitude. The oscillation would increase without limit, unless some nonlinearity in either the aircraft or autopilot acted to change the responses and thus limit the amplitude to some constant larger value (i.e., steady "hunting").

It would be possible to make the system stable if values of any of the four curves could be changed sufficiently. It so happens in the present case that the shape of the aircraft curves in the critical region is influenced chiefly by such basic parameters as yawing inertia and wing loading; thus, there is no simple modification that might be made to this particular aircraft to obtain stability. It is possible, however, to change the autopilot curves. The means of accomplishing such changes will be discussed in a later section.

Nyquist Plots: The data obtained from the above-mentioned frequency-response measurements and calculations may be combined into one curve and plotted on polar coordinates. This is one form of the type of plot known as a Nyquist diagram, and it yields basically the same type of information as can be obtained from the separate frequency-response curves but is, in some cases, simpler to apply and interpret.

The Nyquist diagrams for the two cases of stability mentioned above are plotted in Figs. 6 and 7. The plots are made by plotting the ratio of the aircraft and autopilot responses expressed in polar coordinates as a vector. This can be done because the response curves represent vectors of amplitude R at a phase angle ϵ and the ratio becomes a vector with an amplitude of R_a/R_p at a phase angle of $(\epsilon_a - \epsilon_p)$. The magnitude of $(\psi/\delta)_a/(\psi/\delta)_p$ is plotted at the angle $(\epsilon_a - \epsilon_p)$. Thus, both responses are combined into one set of coordinates and plotted as a single curve.

It will be noticed that, for the case of instability, the curve passes outside the point 1, 0° and that the frequency at which the curve crosses the 0° ray is the same as the critical frequency found by the use of the four separate frequency-response curves. The reason for the use of the (+1) critical point rather than the more usual (−1) is explained in Appendix A. A rigorous derivation and proof of this criterion—that is, neutral stability indicated by the curves passing through 1, 0°—involves advanced mathematics and is beyond the scope of this paper. It is possible, however, to show briefly the correspondence between the coincident intersections of the two pairs of frequency-response curves and the point 1, 0° on the Nyquist polar plot. The quantity plotted on the polar diagram is known as the transfer function and, for systems similar to those under discussion, is equal to $(\psi/\delta)_a \cdot (\delta/\psi)_p$. This product, which is written in reference 2 as $KG(i\omega)$, can be expressed as $(R_a/R_p)\underline{(\epsilon_a - \epsilon_p)}$. The significance of the value of the product of the vector amplitudes, which is written R_a/R_p, becomes apparent when the condition for neutral stability as stated for the separate response curves is considered. If $R_a = R_p$, the term R_a/R_p becomes equal to 1; if $R_a > R_p$, then $R_a/R_p > 1$. Thus, the phase and amplitude characteristics that cause the ϵ and R intersections to occur at the same frequency in a plot of the separate response curves will also cause the polar plot of R_a/R_p versus $(\epsilon_a - \epsilon_p)$ to pass through the point 1, 0 on the Nyquist plot. Similarly, if $R_a > R_p$ at $\epsilon_a - \epsilon_p = 0$, the Nyquist plot will pass outside the point 1, 0 (see Fig. 7) and will indicate instability,

and if $R_a < R_p$ at $\epsilon_a - \epsilon_p = 0$, the Nyquist plot will pass inside 1, 0 and will indicate stability (see Fig. 6).

The quantity "phase margin," which was mentioned previously, is shown graphically on Fig. 6 for the stable case. The phase margin is the angle between the 0° ray and a line drawn from the origin to the intersection of the transfer function plot with a circle of unit amplitude.

The notation used in reference 2 and that of this paper are related as follows:

Herein	Reference 2
amplitude of $(\psi/\delta)_a = R_a =$	$P_a(i\omega)$
amplitude of $(\psi/\delta)_p = R_p =$	$1/P_p\ (i\omega)$

The Nyquist method and its derivation are described completely in references 2, 12, and 13, and a number of uses for such diagrams are given. The chief advantage of the Nyquist plot is that it allows the combination of an indefinite number of elements into one curve. Handling a system with more than two elements would be somewhat awkward if the separate frequency response curves were used, but a Nyquist plot for any number of elements may be made merely by multiplying together the separate ratios of output to input and plotting the resultant quantity at the sum of the individual phase angles. This may be stated in the terms of reference 2 by saying that the product of the transfer functions of the various elements will equal the transfer function of the system—that is, $KG(i\omega)_{\text{system}} = P_a(i\omega) \cdot P_p(i\omega)$. This makes it possible to break up a complex autopilot system into its component parts and to isolate those parts that need adjustment. The method may also be used to predict the performance of an autopilot system composed of several existing components on which data are already available.

Discussion

Applicability

A frequency-response analysis that, like the example given, involves only the two transfer functions or sets of response curves has definite limits of applicability. These limits are usually set by the mechanical arrangement being studied. The method is valid, as presented, for those cases where the autopilot is sensitive to one variable or where the primary motion does not, through aerodynamic coupling, cause other secondary motions that feed back into the autopilot.

An example of the first case would be the roll stabilization system, which was analyzed above, if the autopilot was sensitive to roll only. If the autopilot system is modified in such a way as to make it sensitive to yaw, but acting through the roll control, the analysis grows more complex. For such a system, the method of analysis must be modified in such a way that both responses are considered simultaneously. A block diagram of such a system is given in Fig. 8, and the procedure for such an analysis is described in reference 14, page 140.

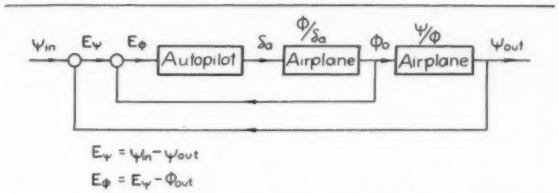

FIG. 8. Block diagram of an aircraft controlled through ailerons by an autopilot sensitive to both roll and yaw.

An example of the second case is that of an airplane controlled in pitch. Here, the longitudinal motion does not couple with any other motion, and, thus, even though the autopilot is sensitive to quantities other than pitch, the motions of the airplane will not feed back into the autopilot except as variations in pitch.

A third case in which the simple analysis can be used is that of an aircraft with two independent autopilots operating separate controls when the aerodynamic cross-coupling of the controls is not large. The procedure here is to analyze the stability of one motion, say roll, and adjust the system in such a way that stability is assured. The other motion, yaw, can then be analyzed, assuming that the aircraft is stabilized in roll, thus eliminating roll as a variable.

The critical control gearings thus calculated are only approximate. If it is practicable to use control gearings sufficiently different from critical in the stable direction to imply adequate damping, it will be unnecessary to refine the calculation. If there is any doubt as to the margin of stability, the more rigorous method of reference 15, which considers the aerodynamic cross-coupling of the controls, should be used.

Nonlinearities

The fact that most present-day autopilots are more or less nonlinear requires special consideration when an attempt is made to apply the frequency response analysis to a specific design problem. Linear implies that, if the response of the autopilot to a sinusoidal disturbance of unit amplitude is known, the response to a disturbance of any amplitude may be obtained by multiplying the unit response by a suitable constant. Nonlinear implies that a change in the amplitude of the disturbance will cause a change in the shape of the response curves, as well as in the magnitude of the response. Many elements in the system, such as the sensing element and the servos, may be inherently nonlinear, and, in addition, the presence of limiting stops or dead spots in the system constitute nonlinearities.

These factors may affect either the amplitude or the phase of the response, and the effects may show up at almost any oscillation amplitude. Thus, it is necessary when analyzing a new or unfamiliar system to measure the response of the autopilot over a range of amplitudes from one below the desired maximum hunting in flight

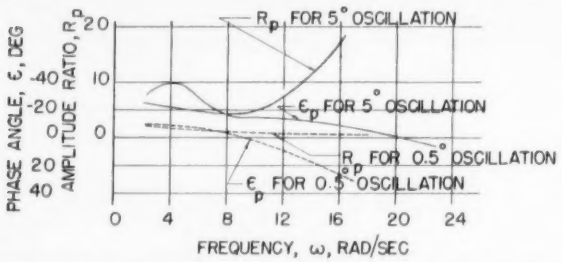

FIG. 9. Frequency-response curves at two amplitudes of oscillation for an air-powered autopilot.

up to an amplitude above the largest disturbance likely to be encountered.

There may also exist nonlinearities in the aerodynamic derivatives used, particularly those concerned with control surfaces, in computing the response curves for the aircraft. These also show up as a variation in characteristics with amplitude. If such variations do exist, they may be accounted for by making separate response calculations for a range of the derivative in question.

After plotting autopilot frequency-response curves for various amplitudes of oscillation, it will usually be seen that the results, when used with the airplane curves, indicate a change from stable to unstable at some amplitude. It is possible for the unstable régime to be either above or below the critical amplitude,[1] but, fortunately, it usually occurs in the lower range, thus ensuring that the airplane, if disturbed, will damp or build up to the critical amplitude and then hunt at that amplitude. If this hunting amplitude is higher than desirable, it will be necessary to modify the characteristics of either the airplane or the autopilot in such a manner that the response curves will indicate stability at the desired amplitude.

An example of the variation in autopilot response with amplitude of disturbance is shown in Figs. 9 and 10. In Fig. 8 the curves are for a rate-displacement system with air pickoffs and servos (similar to the German V-1 autopilot). The rise in R_p for the greater amplitudes of oscillation is caused by stops that limit the maximum travel of the controls; the change in the phase angle at low amplitudes is probably due to dead spot in the rate gyro and, to some extent, in the servos. In Fig. 10 the curves are for a rate-displacement system with autosyn pickoffs and an electric servo. It will be seen here that an increase in R_p occurs at the higher frequency when the amplitude is changed from 1° to 3°. This was not due to stops, which were not used, but to the low maximum speed of the servo. The low speed made it impossible for the servo to attain full deflection in the limited time available at high frequencies. The flat phase angle curve for the 1° amplitude is due to possibly two factors. One, the rate gyro has limiting stops. This makes it impossible for the signal from the rate gyro to increase linearly with frequency. Thus, the 3° amplitude shows the influence of a large rate signal at low frequencies but not at high frequencies. The second factor is the maximum speed of the servo motor. This acts in much the same manner as the rate gyro stops and prevents the full effect of the rate signal from being felt at high frequencies and amplitudes. Thus, the 1° amplitude curve shows little rate effect at low frequencies but does not drop off at the higher frequencies.

The above examples are not intended to indicate general trends, although they are fairly representative of the difference between air and electric servo systems, but are included to give some idea of the types of nonlinearities that may show up when actual autopilots are tested.

Control Gearing

In those cases where the response of the autopilot is determined at the servo, it is possible to use the method outlined in reference 1 and find the critical control gearing. In the notation used in the present report, this process consists of finding the intersection of ϵ_p and ϵ_a and then determining the factor K that will make $R_p = K(R_a)$. The critical control gearing will then be $K°\ \delta$ for every $1°\ \psi$. This will be the maximum ratio of δ to ψ which can be used without making the system unstable. If R_p is greater than R_a, the system is indicated to be stable, but there are other considerations than stability alone. One is the amount of stability or phase margin. This is usually increased by using a control gearing that is lower than critical. Another and counter consideration is that of providing adequate control. The control gearing must be high enough to ensure that any possible out of trim condition can be overcome without excessive airplane deviation and that sufficient control is available to meet maneuvering requirements. In some cases these conditions cannot be met with the autopilot as originally con-

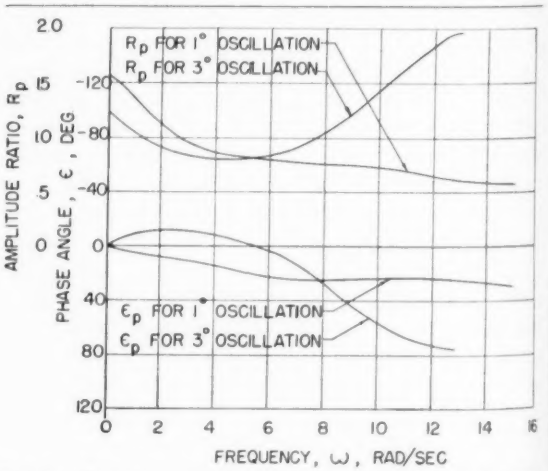

FIG. 10. Frequency-response curves at two amplitudes of oscillation for an electrically powered autopilot.

sidered, and it will become necessary to make alterations to the autopilot system which will shift the phase response in such a way that the intersection of ϵ_p and ϵ_a will occur at a point that will allow the conditions on R_p and R_a to be met.

Modifications to Improve Stability

Either the aircraft or autopilot may be changed when it is necessary to improve the stability of a system, but the basic aircraft design is usually dictated by performance requirements; therefore, the autopilot is the most convenient item to modify. An example of a possible modification is suggested by the curves on Fig. 2. It is obvious that, if the intersection of the ϵ curves could be made to occur at a higher frequency, the value of R_a at the intersection would be low enough to make the system stable. The intersection can be moved by causing the ϵ_p curve to have negative values in the region from $\omega = 0$ to 1. This change may be accomplished by adding first derivative lead to the autopilot.[1] Common ways of obtaining lead are by use of a rate gyroscope or by use of a rate-compensated electronic circuit. The effect of a rate gyroscope may be seen by comparing the ϵ_p curve of Fig. 2 with the 3° amplitude ϵ_p curve of Fig. 10, the chief difference between the two autopilots being that the data on Fig. 10 are for a system having a rate gyroscope. It should be noted that any actual rate gyro will have a resonant frequency beyond which the rate signal will drop off and that any compensating circuit will also vary in its effect as the frequency is increased. Use of higher derivatives (e.g., acceleration signal provides second derivative lead) and of integral signals can also be made to extend the range of the corrections, but in each case the modifying element or adjustment must be designed to meet the particular requirements of the system at hand.

Autopilot Cross Coupling

It happens that some autopilots, when subjected to a disturbance about one axis, will respond with control movements about two axes. That is, a disturbance in pitch may cause an aileron movement as well as the desired elevator movement. The unwanted aileron motion will, of course, cause an equally unwanted rolling motion. Thus, it is advisable to make tests to determine the existence and amount of cross-coupling. The amount that can be tolerated depends upon the use to which the aircraft is to be put and upon the general response characteristics. If the motion caused by cross-coupling does not affect the performance of the aircraft or if the period of the natural oscillation is appreciably different from that caused by coupling, it is possible to accept the cross-coupling. Generally, however, it is possible and advisable to eliminate such effects entirely, inasmuch as they are due to mechanical imperfections rather than inherent design features.

Concluding Remarks

The frequency response method, either by use of separate response curves or by use of Nyquist diagrams, offers a convenient means of analyzing autopilot aircraft stability problems. The method may be used to determine the characteristics of an existing system or to design a new system and is especially useful in handling certain types of nonlinear systems. The results of a frequency-response analysis can be used to indicate what sort of changes should be made to either the airplane or autopilot in order to obtain satisfactory stability characteristics.

There are, however, limitations to the accuracy of such an analysis. These limitations are chiefly due to the inaccuracies in the aerodynamic data for the airplane, the assumptions that are made in setting up the airplane equations, and the existence of nonlinearities in the autopilot. These errors can be minimized to some degree by making the airplane calculations for a sufficient range of aerodynamic derivatives and assumptions and by testing carefully the autopilot over a sufficiently large range of frequencies and amplitudes.

Appendix A

Example Showing Correspondence Between Frequency-Response and Mathematical Methods of Stability Analysis

To illustrate the validity and limitations of the frequency-response method, an analysis will be made of a one-degree-of-freedom system. The procedure is as follows: The frequency-response curves for the airplane and autopilot will be obtained, and from them the stability will be determined as outlined above. To check the results thus obtained, the differential equations of the complete system will be set up and solved. The frequency and damping of the system obtained from the complete solution will be compared with those obtained from the frequency-response method. The system chosen is convenient for purposes of analysis and is used because its mathematical solution is simple and well known. The new quantities used are defined as in Table B.

Table B

Symbol	Quantity	Magnitude
I_Z	Moment of inertia about Z axis, slug ft. squared	22.5
$N_{\dot{\psi}}$	Rate change of yawing moment with yawing velocity, ft.lbs. per rad. per sec.	−105
N_{ψ}	Rate change of yawing moment with yaw angle, ft.lbs. per rad.	−1,730
N_{δ}	Rate change of yawing moment with control deflection, ft.lbs. per rad.	−1,730
l	Control lag factor, sec.	Variable
K	Control gearing	0.6

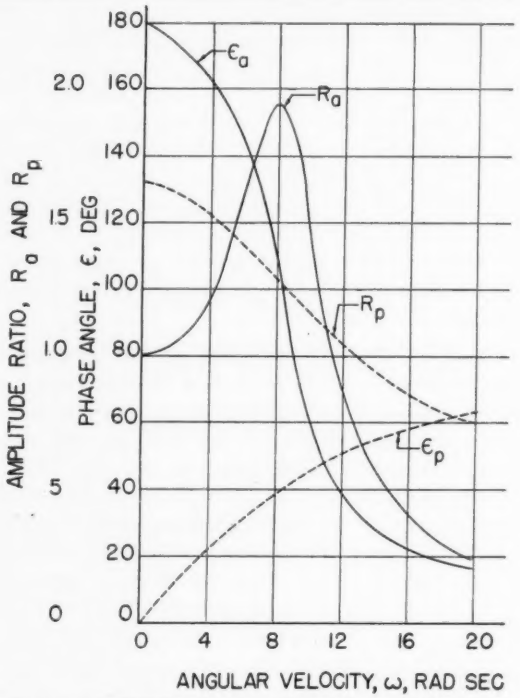

FIG. 11. Frequency-response curves of an aircraft free in yaw only and an autopilot which follows the expression $\delta = K(1 - lD)\psi$, $K = 0.6$, $l = 0.1$. The curves indicate neutral stability.

The equation

$$(I_Z D^2 - N_{\dot\psi} D - N_\psi)\psi = N_\delta \delta \qquad \text{(A1)}$$

represents the motion of an aircraft restrained in bank and sidewise motion but completely free in yaw. The equation

$$\delta = K\,(1 - lD)\psi \qquad \text{(A2)}$$

used for the autopilot, represents an inertialess system so arranged that the control deflection is proportional to the airplane deviation and subject to a viscous lag varying with the rate of airplane deviation.

First, to find the critical or natural frequency, the differential equation of the complete airplane-autopilot system is solved. Thus, taking

$$(I_Z D^2 - N_{\dot\psi} D - N_\psi)\psi = N_\delta \delta$$

and

$$\delta = K(1 - lD)\psi$$

and substituting for δ gives

$$(I_Z D^2 - N_{\dot\psi} D - N_\psi)\psi = N_\delta K(1 - lD)\psi$$

Combining terms gives

$$[I_Z D^2 + (-N_{\dot\psi} + N_\delta K l)D - N_\psi - N_\delta K]\psi = 0 \qquad \text{(A3)}$$

As mentioned before, the frequency response curves are computed for a condition of neutral stability. Therefore, the values of $N_{\dot\psi}$ and N_δ/K are so chosen that the total damping in the system is zero. This condition will be met if $N_{\dot\psi} = N_\delta l K$. Substituting thus in Eq. (A3) yields

$$[I_Z D^2 + (-N_\psi - N_\delta K)]\psi = 0 \qquad \text{(A4)}$$

This is an equation for simple harmonic motion with natural angular frequency,

$$\omega_n = \sqrt{(N_\psi + N_\delta K)/-I_Z}$$

It will now be shown that the same value for ω_n can be obtained from the frequency-response method. The first step is to compute the response curves for the airplane. This process is completely explained in the body of the report and in references 3 and 4 and is only outlined here.

The equation of motion for the airplane is

$$(I_Z D^2 - N_{\dot\psi} D - N_\psi)\psi = N_\delta \delta$$

Using the method previously described, the following expressions are obtained:

$$\left(\frac{\psi}{\delta}\right)_a = \frac{-N_\delta\,(I_Z\omega^2 + N_{\dot\psi})}{(I_Z\omega^2 + N_\psi)^2 + N_{\dot\psi}{}^2\omega^2} + i\,\frac{N_\delta N_{\dot\psi}\omega}{(I_Z\omega^2 + N_\psi)^2 + N_{\dot\psi}{}^2\omega^2}$$

which is of the form $A + iB$, a complex number.

The above relation describes the output motion ψ caused by a sinusoidal input of unit δ as a vector, the characteristics of which depend upon the frequency of input, ω. The properties of the vector $(\psi/\delta)_a$ may be described in terms of the ratio of the amplitudes of ψ and δ—that is, $\psi_{max.}/\delta_{max.}$ and the phase angle between ψ and δ. The expressions are $R_a = \sqrt{A^2 + B^2} = \psi_{max.}/\delta_{max.}$,

$$R_a = \frac{N_\delta}{\sqrt{(I_Z\omega^2 + N_\psi)^2 + N_{\dot\psi}{}^2\omega^2}} = \text{amplitude ratio} \qquad \text{(A5)}$$

and $\epsilon_a = \tan^{-1}(B/A)$.

$$\epsilon_a = \tan^{-1}\frac{-N_{\dot\psi}\omega}{I_Z\omega^2 + N_\psi} = \text{phase angle of } \psi \text{ referred to } \delta \qquad \text{(A6)}$$

These curves are shown in Fig. 11.

The equation for the autopilot is treated in a similar manner.

$$\delta = K\,(1 - lD)\psi \qquad \text{(equation of autopilot)}$$

$$\epsilon_p = \tan^{-1} l\omega \qquad \text{(phase angle of } \psi \text{ referred to } \delta) \qquad \text{(A7)}$$

$$R_p = \frac{1}{K\sqrt{1 + l^2\,\omega^2}} \qquad \text{(A8)}$$

These curves are also shown in Fig. 11. Now the condition for the possibility of a hunting oscillation is that the phase angle curves of aircraft and autopilot

intersect. That is,

$$\epsilon_a = \epsilon_p$$

To determine analytically the frequency at which the intersection will occur, the above expressions for ϵ, Eqs. (A6) and (A7), are equated, using the value for N_ψ of $N_\psi = lN_\delta K$.

$$\epsilon_a = \epsilon_p$$

$$\tan^{-1} l\omega = \tan^{-1}\left(\frac{N_\psi \omega}{-I_Z\omega^2 - N_\psi}\right)$$

gives, as the critical frequency,

$$\omega_c = \sqrt{\frac{N_\psi l + N_\psi}{-lI_Z}} = \sqrt{\frac{N_\psi + N_\delta K}{-I_Z}} \qquad \text{(A9)}$$

which is identical to the result obtained from the differential equation of the complete system.

The expressions for the amplitude ratios at the critical frequency are now compared by substituting Eq. (A9) in Eqs. (A8) and (A5). When this is done Eq. (A8) becomes equal to Eq. (A3) and thus satisfies the condition for neutral stability, as shown in Fig. 11. Thus, both the necessary conditions are met, and the system is shown to be neutrally stable.

Determination of the Frequency of a Damped Oscillation.—As mentioned in the body of the report, the intersection of the ϵ curves for neutral stability will not define the frequency of the oscillation if the oscillation is stable or unstable—that is, if the R curves do not intersect at the same frequency as the ϵ curves. The correct frequency can be determined, however, if the response curves are computed or measured for the actual amount of damping present in the system. The analytical solution is as follows:

The equations of motion are written in the same manner as before, but the condition of neutral stability is avoided by specifying that $N_\psi > lN_\delta K$, thus ensuring that the motion will be convergent. Thus, solving

$$(I_Z D^2 - N_\psi D - N_\psi)\psi = N_\delta K(1 - lD)\psi$$

gives, for the damped natural frequency,

$$\omega_{nd} = \sqrt{\frac{-(-N_\psi + N_\delta Kl)^2}{4I_Z{}^2} - \left(\frac{N_\psi + N_\delta K}{I_Z}\right)}$$

To check this result, the frequency-response equations are written in the same manner as before, but, when the substitution for D is made, a damping term is included. Thus, in

$$\left(\frac{\psi}{\delta}\right)_a = \frac{N_\delta}{I_Z D^2 - N_\psi D - N_\psi}$$

(instead of $D = i\omega$ use $D = -u + i\omega$) where u is equal to the sum of the damping terms (i.e., the coefficient of D divided by twice the coefficient of D^2) in the combined airplane and autopilot equation. The equation then becomes

$$(\psi/\delta)_a = N_\delta/[I_Z(-u + i\omega)^2 - N_\psi(-u + i\omega) - N_\psi]$$

This is solved to give

$$R_a = \frac{N_\delta\sqrt{(I_Z u^2 - I_Z\omega^2 + N_\psi u - N_\psi)^2 + (2I_Z u\omega + N_\psi\omega)^2}}{(I_Z u^2 - I_Z\omega^2 + N_\psi u - N_\psi)^2 + (2I_Z u\,\omega + N_\psi\omega)^2}$$

$$\epsilon_a = \tan^{-1}[(2I_Z u\omega + N_\psi\omega)/(I_Z u^2 - I_Z\omega^2 + N_\psi u - N\psi)]$$

The autopilot equation is treated similarly and yields

$$\left(\frac{\psi}{\delta}\right)_p = \frac{1 + lu}{K[(1 + lu)^2 + l^2\omega^2]} + \frac{il\omega}{K[(1 + lu)^2 + l^2\omega^2]}$$

$$\epsilon_p = \tan^{-1}[l\omega/(1 + lu)]$$

The curves for these expressions are plotted for two values of l in Figs. 12 and 13.

As before, the expressions for the phase angles of the airplane and autopilot are equated and solved for ω_c: $\epsilon_p = \epsilon_a$

$$\tan^{-1}\frac{l\omega}{1 + lu} = \tan^{-1}\frac{2I_Z u\omega + N_\psi\omega}{I_Z u^2 - I_Z\omega^2 + N_\psi u - N_\psi}$$

This reduces to

$$\omega_c = \sqrt{\frac{-(-N_\psi + lKN_\delta)^2}{4\,I_Z{}^2} - \left(\frac{N_\psi + N_\delta K}{I_Z}\right)}$$

which is the frequency of the damped oscillation, as predicted by the solution of the differential equation of the system.

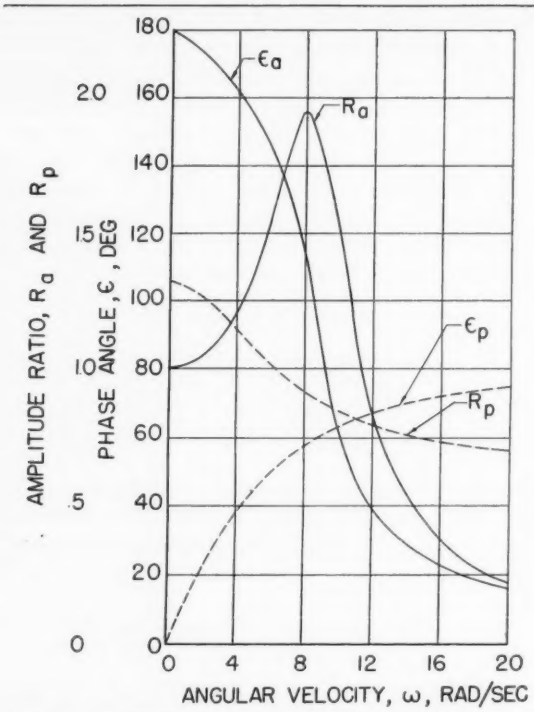

FIG. 12. Frequency-response curves of an aircraft free in yaw only and an autopilot which follows the expression $\delta = K(1 - lD)\psi$, $K = 0.6$, $l = 0.2$. The curves indicate instability.

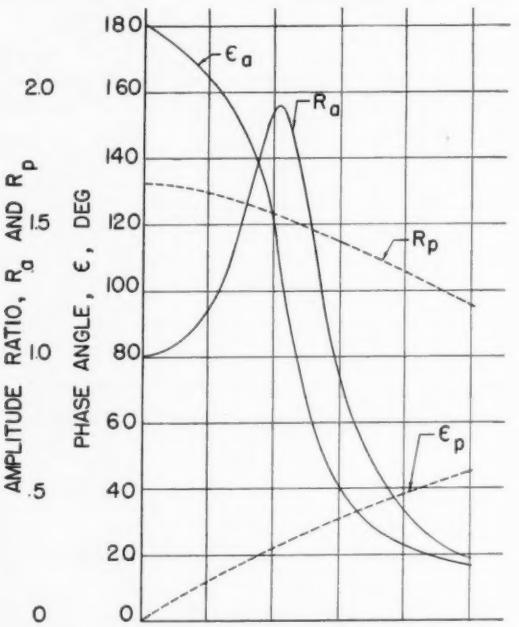

FIG. 13. Frequency-response curves of an aircraft free in yaw only and an autopilot which follows the expression $\delta = K(1 - D)\psi$, $K = 0.6$, $l = 0.05$. The curves indicate stability.

The three Nyquist plots that correspond to the curves shown in Figs. 11, 12, and 13 are presented in Fig. 14. It can be seen that each of the curves crosses the 0° ray at the critical frequency as defined by the separate phase angle curves of Figs. 11, 12, and 13. Further, applying the criterion that those curves that pass outside (0°, 1) indicate instability and those that pass inside (0°, 1) indicate stability, it is evident that the results obtained by both methods are identical. If the Nyquist plots in this paper are compared with those of the references, it will be noticed that the critical point in the references is usually at the 0°, −1 point instead of at the 0°, 1 point, as in Figs. 6, 7, and 14. This discrepancy arises because of the sign convention used in the autopilot equations and tests. It is usual in electrical work to represent the correction to a positive error by a negative quantity, but, because of the N.A.C.A. sign conventions, the correction to a plus or upward pitch error is represented by a plus (down elevator is positive) quantity. This difference in conventions causes the critical point to shift 180°. The Nyquist plots are equally valid for either case, and the method of interpretation remains the same.

Appendix B

EQUATIONS OF MOTION

Both longitudinal and lateral equations are subject to the following assumptions:

(1) All deviations from steady state are small—that is, incremental value $\ll 1$.

(2) The products of two or more incremental quantities may be neglected.

(3) The combined effect of two or more separate components is equal to the sum of the individual effects.

(4) The changes in aerodynamic forces and moments due to a deviation are directly proportional to the deviation—that is, the stability derivatives are constants.

(5) The lateral and longitudinal motions are independent of each other.

Equations of Longitudinal Motion

Equations in Three Degrees of Freedom.—These equations are written in terms of the more commonly used parameters of longitudinal motion: u, the ratio of change in forward speed to basic forward speed; θ, the angle of inclination of the body axis to the horizontal; and α, the angle of attack. The derivatives are written in terms of C_D, C_L, and C_m and include all those that have been considered appreciable for conventional airplanes, plus other derivatives that may be important in pilotless aircraft work. It is possible that there are other derivatives that should be used in specific cases. These can be inserted in the equations as needed, provided that they are expressed in the same units as the rest of the derivatives.

Drag force equation:

$$\frac{mV}{qS} Du = -2(C_D + C_{D_u})u - \left(C_{D_\alpha} + C_{D_{D\alpha}} D \frac{c}{2V}\right) \times \alpha - \left(C_{D_{\delta_e}} + C_{D_{D\delta_e}} \frac{2}{2V} D\right) - C_{D_{D\theta}} \frac{c}{2V} D\theta - T_C' \sin \alpha_0 \times \alpha - \frac{W}{qS} \cos \gamma_0 (\theta - \alpha)$$

Lift force equation:

$$\frac{mV}{qS} D\theta - \frac{mV}{qS} D\alpha = (2C_L + C_{L_u})\, u + \left(C_{L_\alpha} + C_{L_{D\alpha}} \frac{c}{2V} D\right) \alpha + \left(C_{L_{\delta_e}} + C_{L_{D\delta_e}} \frac{c}{2V} D\right) \times \delta_e + C_{L_{D\theta}} \frac{c}{2V} D\theta + T_C' \cos \alpha_0\, \alpha + \frac{W}{qS} \sin \gamma_0 (\theta - \alpha)$$

Pitching moment equation:

$$D^2\theta \frac{I_Y}{qSc} = 2C_m u + \left(C_{m_\alpha} + C_{m_{D\alpha}} \frac{c}{2V} D\right) \times \alpha + C_{m_u} u + C_{m_{D\theta}} \frac{c}{2V} D\theta + \left(C_{m_{\delta_e}} + C_{m_{D\delta_e}} \frac{c}{2V} D\right) \times \delta_e + T_C' \frac{y}{c}$$

where the quantities are defined as follows:

m	= mass of aircraft, slugs
q	= dynamic pressure $[(\rho/2)V^2]$, lbs. per sq.ft.
ρ	= air density, slugs per cu.ft.
S	= wing area, sq.ft.
c	= mean aerodynamic chord, ft.
D	= differential operator d/dt
V	= forward velocity, ft. per sec.
u	= ratio of incremental forward velocity to basic forward velocity, $\Delta V/V$
C_D	= drag coefficient, drag$/qS$
C_L	= lift coefficient, lift$/qS$
C_m	= pitching moment coefficient, pitching moment$/qSC$
T_C'	= thrust coefficient, thrust$/qS$
α	= angle of attack, radians
θ	= angle between aircraft body axis and horizontal, rad.
γ	= angle between flight path of center of gravity and horizontal, rad. NOTE: Subscript 0 indicates steady state value; symbol with no subscript indicates increment from steady state
q	= rate change of θ with time, $d\theta/dt$
δ	= deflection of control surface, rad.
y	= perpendicular distance from thrust line to center of gravity, ft.
$C_{D_\alpha}, C_{L_\alpha}, C_{m_\alpha}$	= $\partial C_D/\partial\alpha, \partial C_L/\partial\alpha, \partial C_m/\partial\alpha$
$C_{D_{D\alpha}}, C_{L_{D\alpha}}, C_{m_{D\alpha}}$	= $\partial C_D/\partial(D\alpha c/2V), \partial C_L/\partial(D\alpha c/2V), \partial C_m \div \partial(D\alpha c/2V)$
$C_{D_u}, C_{L_u}, C_{m_u}$	= $\partial C_D/\partial u, \partial C_L/\partial u, \partial C_m/\partial u$
$C_{D_\theta}, C_{L_\theta}, C_{m_\theta}$	= $\partial C_D/\partial\theta, \partial C_L/\partial\theta, \partial C_m/\partial\theta$
$C_{D_{D\theta}}, C_{L_{D\theta}}, C_{m_{D\theta}}$	= $\partial C_D/\partial(qc/2V), \partial C_L/\partial(qc/2V), \partial C_m/\partial(qc \div 2V)$
$C_{D_\delta}, C_{L_\delta}, C_{m_\delta}$	= $\partial C_D/\partial\delta, \partial C_L/\partial\delta, \partial C_m/\partial\delta$
$C_{L_{D\delta}}, C_{m_{D\delta}}$	= $\partial C_L/\partial(D\delta c/2V), \partial C_m/\partial(D\delta c/2V)$

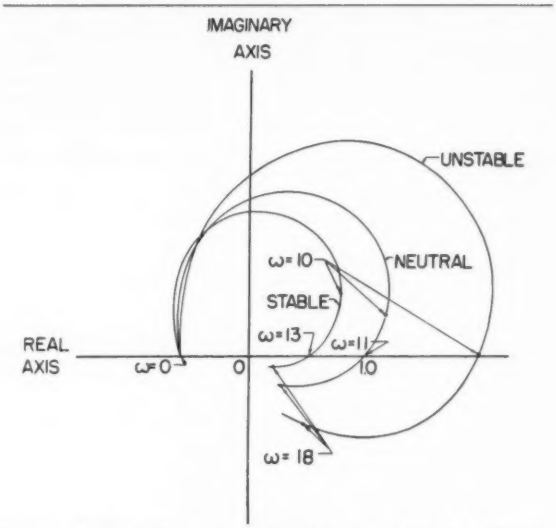

FIG. 14. Nyquist diagram for unstable, neutral, and stable aircraft-autopilot combinations.

Equations in Two Degrees of Freedom.—The three equations given before describe a motion that is usually the sum of two well-defined oscillatory motions. One of these, the phugoid, is a lightly damped, long-period motion in which the angle of attack remains nearly constant and the forward speed and horizontal inclination vary. The other is a short-period, heavily damped motion in which the forward speed remains constant and θ and α vary. It is chiefly the characteristics of this motion which affect the requirements that the autopilot must fulfill; therefore, the drag force equation and all terms due to a variation in forward speed may be dropped, leaving two equations in θ and α. These equations are presented below:

Lift force equation:

$$\frac{mV}{qS} D\theta - \frac{mVD\alpha}{qS} - \left(C_{L_\alpha} + C_{L_{D\alpha}} \frac{c}{2V} D\right) \times \alpha - \left(C_{L_{D\theta}} \frac{c}{2V} D\right) \theta - T_C' \cos \alpha_0\, \alpha - \frac{W}{qS} \times \sin \gamma_0 (\theta - \alpha) = \left(C_{L_{\delta_e}} + C_{L_{D\delta_e}} \frac{c}{2V} D\right) \delta_e$$

Pitching moment equation:

$$\frac{D^2\theta}{qSc} - \left(C_{m_\alpha} + C_{m_{D\alpha}} \frac{c}{2V} D\right) \alpha - C_{m_{D\theta}} \frac{c}{2V} D\theta - T_C' \frac{y}{c} = \left(C_{m_{\delta_e}} + C_{m_{D\delta_e}} \frac{c}{2V} D\right) \delta_e$$

Equations of Lateral Motion

Yawing and Sideslipping.—The complete set of three lateral equations was given in the body of the report. For certain types of aircraft, these equations may be simplified to two- and one-degree-of-freedom systems. If the aircraft is symmetrical and identical about the

X–Z and Y-body axis planes (i.e., of cruciform configuration), it can usually be assumed that there is no coupling between the rolling and either the yawing or sideslipping motion. This assumption can be proved by a wind-tunnel test that shows the derivative C_{l_β} to be zero. When the rolling terms are omitted, the equations become:

Yawing moment equation:

$$\frac{mk_Z^2D^2\psi}{qSb} - C_{n_r}\frac{b}{2V}D\psi - C_{n_\beta}\beta = C_{n_{\delta_a}}\delta_a + \left(C_{n_{\delta_r}} + C_{n_{D\delta_r}}\frac{b}{2V}D\right)\delta_r$$

Sideforce equation:

$$\left(\frac{mVD}{qS} - \frac{W}{qS}\sin\gamma_0 - C_{Y_r}\frac{b}{2V}D\right)\psi + \left(\frac{mVD}{qS} - C_{Y_\beta}\right)\beta = C_{Y_{\delta_a}}\delta_a + \left(C_{Y_{\delta_r}} + C_{Y_{D\delta_r}}\frac{b}{2V}D\right)\delta_r$$

The assumption upon which the above simplification was based is valid in one direction only. That is, it can be assumed that the side slipping and yawing does not cause rolling, but it cannot be assumed that a rolling motion will not cause yawing moments. Therefore, the two-equation method is valid only when the roll stabilization is good enough to limit the rolling velocities to values that will not cause appreciable yawing moments.

Rolling.—Using the same assumptions as for the yawing and sideslipping allows the rolling motion of a cruciform aircraft to be expressed by only one equation:

$$\left(\frac{mk_X^2D^2}{qSb} - C_{l_p}\frac{b}{2V}D\right)\phi = \left(C_{l_{\delta_a}} + C_{l_{D\delta_a}}\frac{b}{2V}D\right)\times \delta_a + C_{l_{D\delta_a}}\delta_r$$

References

[1] Greenberg, Harry, *Frequency-Response Method for Determination of Dynamic Stability Characteristics of Airplanes with Automatic Controls*, N.A.C.A. T.N. No. 1229, March, 1947.

[2] Hall, A. C., *The Analysis and Synthesis of Linear Servomechanisms;* The Technology Press, Massachusetts Institute of Technology, Cambridge, Mass., 1943.

[3] Johnson, *Mathematical and Physical Principles of Engineering Analysis*, Chapt. VII; McGraw-Hill Book Company, Inc., New York, 1944.

[4] von Kármán, Th., and Biot, M. A., *Mathematical Methods in Engineering*, Chapt. IX; McGraw-Hill Book Company, Inc., New York, 1940.

[5] Zimmerman, Charles H., *An Analysis of Lateral Stability in Power-Off Flight with Charts for Use in Design*, N.A.C.A. Report No. 589, 1937.

[6] Jones, T. Melville, *Airplane Stability.* Volume V of *Aeronautical Theory*, W. F. Durand, Ed.; Julius Springer, Berlin, 1934.

[7] Sternfield, Leonard, *Effect of Product of Inertia on Lateral Stability*, N.A.C.A. T.N. No. 1193, March, 1947.

[8] Greenberg, Harry, and Sternfield, Leonard, *A Theoretical Investigation of Longitudinal Stability of Airplanes with Free Controls Including Effect of Friction in Control System*, N.A.C.A. Wartime Report L-430, February, 1944.

[9] Soulé, Hartley A., and Miller, Marvel P., *The Experimental Determination of the Moments of Inertia of Airplanes*, N.A.C.A. T.R. No. 467, 1933.

[10] Cotter, William E., Jr., *Summary and Analysis of Data on Damping in Yaw and Pitch for a Number of Airplane Models*, N.A.C.A. T.N. No. 1080, 1946.

[11] Pearson, Henry A., and Jones, Robert T., *Theoretical Stability and Control Characteristics of Wings with Various Amounts of Taper and Twist*, N.A.C.A. Report No. 635, 1938.

[12] James, H. M., Nichols, N. B., Phillips, Ralph S., *Theory of Servomechanisms;* McGraw-Hill Book Company, Inc., New York, 1947.

[13] Bode, H. W., *Network Analysis and Feed Back Amplifier Design;* D. Van Nostrand, New York, 1945.

[14] Brown, Gordon S., and Campbell, Donald P., *Principles of Servomechanisms;* John Wiley & Sons, Inc., New York, 1948.

[15] Greenberg, Harry, *Application of the Frequency Response Method to the Calculation of the Dynamic Stability Limits of Airplanes with Two Independent Autopilots*, Princeton AEL Report No. 119, 1947.

[16] Shortal, Joseph A., *Effect of Tip Shape and Dihedral on Lateral-Stability Characteristics*, N.A.C.A. Report No. 548, 1936.

[17] House, Rufus O., and Wallace, Arthur R., *Wind-Tunnel Investigation of Effect of Interference on Lateral-Stability Characteristics of Four NACA 23012 Wings, an Elliptical and a Circular Fuselage, and Vertical Fins*, N.A.C.A. Report No. 705, 1941.

[18] Pass, H. R., *Analysis of Wind-Tunnel Data on Directional Stability and Control*, N.A.C.A. T.N. No. 775, 1940.

[19] Hoggard, H. Page, Jr., *Wind-Tunnel Investigation of Fuselage Stability in Yaw with Various Arrangements of Fins*, N.A.C.A. T.N. No. 785, 1940.

[20] Imlay, Frederick H., *The Estimation of the Rate of Change of Yawing Moment with Sideslip*, N.A.C.A. T.N. No. 636, 1938.

[21] Schade, Robert O., *Effect of Geometric Dihedral on the Aerodynamic Characteristics of Two Isolated Vee-Tail Surfaces*, N.A.C.A. T.N. No. 1369, July, 1947.

[22] Recant, Isidore G., and Wallace, Arthur R., *Wind-Tunnel Investigation of Effect of Yaw on Lateral-Stability Characteristics III. Symmetrically Tapered Wing at Various Positions on Circular Fuselage with and without a Vertical Tail*, N.A.C.A. T.N. No. 825, 1941.

[23] Letko, William, and Cowan, John W., *Effect of Taper Ratio on Low-speed Static and Yawing Stability Derivatives of 45° Sweptback Wings with Aspect Ratio of 2.61*, N.A.C.A. T.N. No. 1671, 1948.

[24] Bamber, M. J., and House, R. O., *Wind-Tunnel Investigation of Effect of Yaw on Lateral-Stability Characteristics. I—Four N.A.C.A. 23012 Wings of Various Plan Forms with and without Dihedral*, N.A.C.A. T.N. No. 703, 1939.

[25] Tamburello, Vito, and Weil, Joseph, *Wind Tunnel Investigation of the Effect of Power and Flaps on the Static Lateral Characteristics of a Single Engine, Low Wing Airplane Model*, N.A.C.A. T.N. No. 1327, June, 1947.

[26] Hagerman, John R., *Wind-Tunnel Investigation of the Effect of Power and Flaps on the Static Lateral Stability and Control Characteristics of a Single-Engine High-Wing Airplane Model*, N.A.C.A. T.N. No. 1379, July, 1947.

[27] Ribner, Herbert S., *The Stability Derivatives of Low-Aspect-Ratio Triangular Wings at Subsonic and Supersonic Speeds*, N.A.C.A. T.N. No. 1423, September, 1947.

[28] Ankenbruck, Herman O., *Effects of Tip Dihedral on Lateral Stability and Control Characteristics as Determined by Tests of a Dynamic Model in the Langley Free-Flight Tunnel*, N.A.C.A. T.N. No. 1059, 1946.

[29] Maggin, Bernard, and Bennett, Charles V., *Flight Tests of an Airplane Model with a 42° Swept-Back Wing in the Langley Free-Flight Tunnel*, N.A.C.A. T.N. No. 1287, May, 1947.

[30] Maggin, Bernard, and Bennett, Charles V., *Low-Speed Stability and Damping-in-Roll Characteristics of Some Highly Swept Wings*, N.A.C.A. T.N. No. 1286, May, 1947.

[31] Jones, A. L., Spreiter, John R., and Alksne, Alberta, *The Roll Due to Sideslip of Triangular, Trapezoidal, and Related Planforms in Supersonic Flow*, N.A.C.A. T.N. No. 1700, October, 1948.

[32] Harmon, Sidney M., *Stability Derivatives of Thin Rectangular Wings at Supersonic Speed*, N.A.C.A. T.N. No. 1706, November, 1948.

[33] Malvestuto, F. S., Jr., and Margolis, Kenneth, *Theoretical Stability Derivatives of Thin Sweptback Wings Tapered to a Point with Sweptback or Sweptforward Trailing Edges for a Limited Range of Supersonic Speeds*, N.A.C.A. T.N. No. 1761, January, 1949.

[34] Toll, Thomas A., and Queijo, M. J., *Approximate Relations and Charts for Low Speed Stability Derivatives of Swept Wings*, N.A.C.A. T.N. No. 1581, May, 1948.

[35] Seacord, Charles L., and Ankenbruck, Herman O., *Determination of the Stability and Control Characteristics of a Straight-Wing, Tailless Fighter-Airplane Model in the Langley Free-Flight Tunnel*, N.A.C.A. Wartime Report No. L-199, February, 1946.

[36] Fehlner, Leo F., and MacLachlan, Robert, *Investigation of Effect of Sideslip on Lateral Stability—I—Circular Fuselage with Variations in Vertical-Tail Area and Tail Length with and without Horizontal Tail Surface*, N.A.C.A. Wartime Report No. L-12, May, 1944.

[37] Recant, I. G., and Wallace, Arthur R., *Wind-Tunnel Investigation of Effect of Yaw on Lateral-Stability Characteristics—IV—Symmetrically Tapered Wing with a Circular Fuselage Having a Wedge-Shaped Rear and a Vertical Tail*, N.A.C.A. Wartime Report No. L-520, March, 1942.

[38] Recant, Isidore G., and Wallace, Arthur R., *Wind-Tunnel Investigation of the Effect of Vertical Position of the Wing on the Side Flow in the Region of the Vertical Tail*, N.A.C.A. T.N. No. 804, 1941.

[39] Soulé, Hartley A., *Influence of Large Amounts of Wing Sweep on Stability and Control Problems of Aircraft*, N.A.C.A. T.N. No. 1033, 1946.

[40] Campbell, John P., and Mathews, Ward O., *Experimental Determination of the Yawing Moment Due to Yawing Contributed by the Wing, Fuselage, and Vertical Tail of a Midwing Airplane Model*, N.A.C.A. Wartime Report No. L-387, June, 1943.

[41] Harmon, Sidney M., *Determination of the Damping Moment in Yawing for Tapered Wings with Partial-Span Flaps*, N.A.C.A. Wartime Report No. L-395, August, 1943.

[42] Glauert, H., *The Determination of Rotary Derivatives by E. F. Relf, T. Lavender, E. Owen, with an Appendix on Approximate Formulae for Rotary Derivatives*, R.A.E. R. & M. 809.

[43] Halliday, A. S., and Burge, C. H., *Whirling Arm Experiments on Lateral Stability*, A.R.C. R. & M. 1642, 1934.

[44] Murray, Harry E., and Wells, Evelyn G., *Wind Tunnel Investigation of the Effect of Wing Tip Fuel Tanks on Characteristics of Unswept Wings in Steady Roll*, N.A.C.A. T.N. No. 1317, June, 1947.

[45] MacLachlan, Robert, and Letko, William, *Correlation of Two Experimental Methods of Determining the Rolling Characteristics of Unswept Wings*, N.A.C.A. T.N. No. 1309, May, 1947.

[46] Jones, Arthur L., and Alksne, Alberta, *The Damping Due to Roll of Triangular, Trapezoidal, and Related Planforms in Supersonic Flow*, N.A.C.A. T.N. No. 1548, March, 1948.

[47] Brown, Clinton E., and Adams, Mac. C., *Damping in Pitch and Roll of Triangular Wings at Supersonic Speeds*, N.A.C.A. T.N. No. 1566, 1948.

[48] Neely, Robert H., Fairbanks, Richard W., and Conner, D. William, *Effects of Wing and Nacelle Modifications on Drag and Wake Characteristics of a Bomber-Type Airplane Mode* N.A.C.A. Wartime Report No. L-114, December, 1945.

[49] Campbell, John P., and Paulson, John W., *The Effects of Static Margin and Rotational Damping in Pitch on the Longitudinal Stability Characteristics of an Airplane as Determined by Tests of a Model in the NACA Langley Free Flight Tunnel*, N.A.C.A. Wartime Report No. L-55, June, 1944.

[50] Talmage, Donald B., *Determination from Flight Tests of Thrust Coefficients for 10 Full-Scale Airplanes in the Gliding Condition with Engine Idling*, N.A.C.A. Wartime Report No. L-88, June, 1945.

[51] Priestly, E., *Interim Report on the Estimation of Static Longitudinal Stability*, R.A.E. Farnborough Aero. 1728, June, 1942.

[52] Jones, Robert T., *Notes on the Stability and Control of Tailless Airplanes*, N.A.C.A. T.N. No. 837, 1941.

[53] Shortal, Joseph A., and Maggin, Bernard, *Effect of Sweepback and Aspect Ratio on Longitudinal Stability Characteristics of Wings at Low Speeds*, N.A.C.A. T.N. No. 1093, 1946.

[54] Weick, Fred E., and Sanders, Robert, *Aerodynamic Tests of a Low Aspect Ratio Tapered Wing with Various Flaps, for Use on Tailless Airplanes*, N.A.C.A T.N. No. 463, 1933.

[55] Zimmerman, C. H., *Aerodynamic Characteristics of Several Airfoils of Low Aspect Ratio*, N.A.C.A. T.N. No. 539, 1935.

[56] Jones, Robert T., *Properties of Low-Aspect-Ratio Pointed Wings at Speeds Below and Above the Speed of Sound*, N.A.C.A. T.N. No. 1032, 1946.

[57] Purser, Paul E., Spearman, M. Leroy, and Bates, William R., *Preliminary Investigation at Low Speed of Downwash Characteristics of Small-Scale Sweptback Wings*, N.A.C.A. T.N. No. 1378, July, 1947.

[58] Higgins, George J., *A Study of the Pitching Moments and the Stability Characteristics of Monoplanes*, N.A.C.A. T.N. No. 511, 1934.

[59] Lowry, John G., and Schneiter, Leslie E., *Investigation at Low Speed of the Longitudinal Stability Characteristics of a 60° Swept-Back, Tapered Low-Drag Wing*, N.A.C.A. T.N. No. 1284, May, 1947.

[60] Glauert, H., *The Lift and Pitching Moment of an Aerofoil Due to a Uniform Angular Velocity of Pitch*, R. & M. No. 1216, 1926.

[61] Glauert, H., and Gates, S. B., *The Characteristics of a Tapered and Twisted Wing with Sweep-Back*, R. & M. No. 1226.

[62] Cowley, W. L., and Glauert, H., *The Effect of the Lag of the Downwash on the Longitudinal Stability of an Aeroplane and on the Rotary Derivative Mq*, R. & M. No. 718, 1921.

[63] Simmons, L. F. G., and Ower, E., *An Investigation of the Influence of Downwash on the Rotary Derivative Mq*, R. & M. No. 826, 1921.

[64] Cohen, Doris, and Jones, Robert T., *An Analysis of the Stability of an Airplane with Free Controls*, N.A.C.A. T.R. No. 709, 1941.

[65] Zimmerman, Charles H., *An Analysis of Longitudinal Stability in Power-Off Flight with Charts for Use in Design*, N.A.C.A. T.R. No. 521, 1935.

[66] Zimmerman, Charles H., *Aerodynamic Characteristics of Several Airfoils of Low Aspect Ratio*, N.A.C.A. T.N. No. 539, 1935.

[67] Jones, Robert T., *Wing Plan Forms for High-Speed Flight*, N.A.C.A. T.N. No. 1033, 1946.

[68] Jones, Robert T., *Estimated Lift-Drag Ratios at Supersonic Speed*, N.A.C.A. T.N. No. 1350, July, 1947.

[69] Abbott, Ira H., von Doenhoff, Albert E., and Stivers, Louis S., Jr., *Summary of Airfoil Data*, N.A.C.A. Wartime Report No. L-560, March, 1945.

[70] Ames, Milton B., Jr., and Sears, Richard I., *Determination of Control-Surface Characteristics from NACA Plain-Flap and Tab Data*, N.A.C.A. T.R. No. 721, 1941.

[71] Research Department—Compiled by Thomas A. Toll, *Summary of Lateral-Control Researh*, N.A.C.A. T.N. No. 1245, March, 1947.

[72] Ribner, Herbert S., and Malvestuto, Frank S., *Stability Derivatives of Triangular Wings at Supersonic Speeds*, N.A.C.A. T.N. No. 1572, May, 1948.

[73] Lagerstrom, Paco A., and Graham, Martha E., *Linearized Theory of Supersonic Control Surfaces*, Douglas Report SM 13060, July 24, 1947.

[74] MacLachlan, Robert, and Fisher, Lewis R., *Wind Tunnel Investigation at Low Speeds of the Pitching Derivatives of Untapered Swept Wings*, N.A.C.A. RM L8G19, September, 1948.

[75] Fricke, Charles W., Jr., *Application of the Linearized Theory of Supersonic to the Estimation of Control Surface Characteristics*, N.A.C.A. T.N. No. 1554, March, 1948.

[76] Queijo, Manuel J., and Jaquet, Byron M., *Effects of Geometric Dihedral on the Low Speed Rolling Derivatives of Swept Wings*, N.A.C.A. T.N. No. 1732, October, 1948.

[77] Queijo, Manuel J., and Jaquet, Byron M., *Investigation of the Effects of Dihedral on the Low Speed Static Stability and Yawing Characteristics of an Untapered 45° Swept Wing Model of Aspect Ratio 2.61*, N.A.C.A. T.N. No. 1668, September, 1948.

[78] Zimmerman, Charles H., *Characteristics of Clark-Y Airfoils of Small Aspect Ratios*, N.A.C.A. Report No. 431, 1932.

[79] Tucker, Warren A., *Characteristics of Thin Triangular Wings with Triangular Tip Control Surfaces at Supersonic Speeds with Mach Lines behind the Leading Edge*, N.A.C.A. T.N. No. 1600, 1948.

[80] Tucker, Warren A., *Characteristics of Thin Triangular Wings with Constant Chord Full Span Control Surfaces at Supersonic Speeds*, N.A.C.A. T.N. No. 1601, 1948.

[81] Tucker, Warren A., and Nelson, Robert L., *Characteristics of Thin Triangular Wings with Constant Chord Partial Span Control Surfaces at Supersonic Speeds*, N.A.C.A. T.N. No. 1660, July, 1948.

[82] Tucker, Warren A., and Nelson, Robert L., *Theoretical Characteristics in Supersonic Flow of Constant-Chord Partial-Span Control Surfaces on Rectangular Wings Having Finite Thickness*, N.A.C.A. T.N. No. 1708, September, 1948.

[83] Tucker, Warren A., and Nelson, Robert L., *The Flexible Rectangular Wing in Roll at Supersonic Flight Speeds*, N.A.C.A. T.N. No. 1769, December, 1948.

[84] Fischel, Jack, and Tamburello, Vito, *Investigation of Effect of Spanwise Location and Chordwise Location of Spoilers on Lateral Control Characteristics of a Tapered Wing*, N.A.C.A. T.N. No. 1294, May, 1947.

[85] Luoma, Arvo A., *Effect of Compressibility on Section Characteristics of an Airfoil with a Round-Nose Slotted Frise Aileron*, N.A.C.A. T.N. No. 1975, May, 1946.

[86] Stevenson, David B., and Byrne, Robert W., *High-Speed Wind-Tunnel Tests of an NACA 16-009 Airfoil Having a 32.0-Percent-Chord Flap with an Overhang 20.7 Percent of the Flap Chord*, N.A.C.A. T.N. No. 1406, August, 1947.

[87] Stevenson, David B., and Adler, Alfred A., *High-Speed Wind-Tunnel Tests of an NACA 0009-64 Airfoil Having a 33.4-Percent-Chord Flap with an Overhang 20.1 Percent of the Flap Chord*, N.A.C.A. T.N. No. 1417, September, 1947.

Third Symposium on Plasticity

The Third Symposium on Plasticity will be held on September 8 and 9, 1950, under the auspices of the Graduate Division of Applied Mathematics at Brown University, Providence, R.I.

American and foreign experts in the field will present papers covering their most recent experimental and analytical research on "Stress-Strain Relations" and "Problems and Methods in the Analysis of Structures and Continuous Media." Institute members are invited to participate in the discussion.

For further information, please write to Prof. D. C. Drucker, Brown University, Providence 2, R.I.

Torsion of Thin-Walled Closed Cylinders Beyond the Elastic Limit*

G. H. HANDELMAN†

Carnegie Institute of Technology

SUMMARY

The torsion of thin-walled closed cylinders beyond the elastic limit is treated as a problem in "technical plasticity." From assumptions on the nature of the wall thickness, the problem is reduced to one of a single stress and a single strain. Formulas for the distribution of the shear stress, the shear strain, and the warping function are found. An analog to the formula for the torque vs. angle of twist in the elastic state is developed. It is shown how the problem may be reduced to an equivalent elastic tube through the introduction of an artificial thickness function. Formulas are also given for multicell sections. Specific numerical-graphical procedures are developed for sections of piecewise-constant wall thickness; two examples, single-cell and multi-cell, are given in detail.

STATEMENT OF PROBLEM

THE NUMBER OF EXAMPLES that have been solved in the field of solids stressed beyond the elastic limit appears small when compared with the corresponding amount of material developed in the classical theory of linear elasticity. This is in large part due to the mathematical complexities that arise from the essential nonlinearity of the theory. However, there appears to be one field of problems, not fully exploited, in which interesting results can be obtained without undue difficulty. These questions might be classified as belonging to the field of "technical plasticity." The corresponding problems in the theory of linear elasticity are usually considered in texts on strength of materials or applied elasticity. This paper is concerned with such a problem—the torsion of a thin-walled cylinder beyond the elastic limit. Various assumptions of the order of those used in the corresponding elasticity problem have been made, for the major question to be answered lies in the gross behavior of the section rather than a precise description of the stress-and-strain distribution.

Torsion of thin-walled elastic cylinders has been discussed in several books on applied elasticity[1] and strength of materials,[2] as well as in recent papers on applications of the theory and extensions to more complicated stress distributions.[3, 4] This paper is an attempt to extend these results to the case where the stresses exceed the yield limit and the stress-strain relation is no longer linear. In particular, an analog to Bredt's formula[5] relating the angle of twist per unit length and the applied torque will be derived and applied to two sections, a single-cell section and a double-cell section.

The cylinder in question is assumed to be a thin-walled, closed, prismatic tube subject to a distribution of end forces and couples that are statically equivalent to a single applied couple Q. In keeping with the semi-inverse method of elasticity, the exact distribution of these end forces can be ignored, and the stresses in the tube will be required only to have a resultant torque equal to Q. The lateral surfaces of the cylinder are assumed to be free from external loads. More precise conditions on the term "thin-walled" will be given later in the discussion.

Consider a cross section of the tube taken normal to the axes of the cylinder and a closed curve C, the reference line, lying in this cross section (see Fig. 1). If s denotes the arc length along C, measured from some fixed point 0, then the inner wall may be defined by a function $t_i(s)$, which measures the distance of this wall from C taken along a normal to C at the point s. Similarly, the outer wall can be defined by a function $t_0(s)$, the distance between the outer wall and C at s. The total thickness of the wall, $t(s)$, is defined by the relation

$$t(s) = t_0(s) + t_i(s)$$

Two coordinate systems, related naturally to this description of the tube, will be used in the discussion to follow. The first coordinate system consists of the reference line C, the normals to C, and the parallels to the axis of the tube. Thus, at each point of C we have a basic trihedral of mutually orthogonal unit vectors, the unit vector $\boldsymbol{t}$ tangent to C, the unit vector $\boldsymbol{n}$ normal to C, and the unit vector $\boldsymbol{z}$ parallel to the axis. These vectors are oriented so as to form a right-handed system in the order named (see Fig. 1). A point P_1 in the tube is then determined by three coordinates: s, the distance along C of the normal projection of P_1 on C; n, the normal distance of P_1 to C (positive if measured along the outward normal); and z, the distance between the cross section that contains P_1 and some fixed cross section. If the reference line is assumed to be a closed curve that admits a representation in terms of s and is twice differentiable with respect to that variable, then it can be shown that the element of arc length in

Received December 21, 1949.

* This paper is part of a thesis submitted in partial fulfillment of the requirements for the degree of Ph.D. in Applied Mathematics at Brown University.

† Assistant Professor of Mathematics.

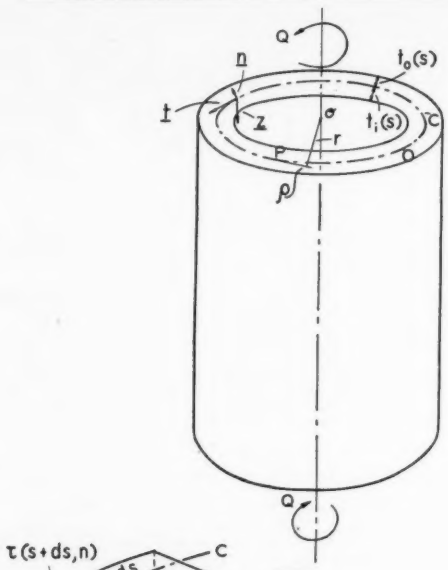

FIG. 1

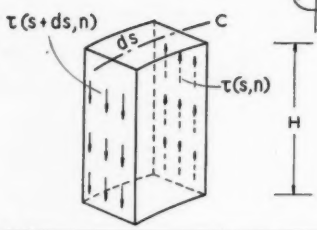

FIG. 2

these coordinates, dl, can be written as

$$dl^2 = [1 + (n/R)]^2\, ds^2 + dn^2 + dz^2 \qquad (1)$$

where R is the radius of curvature of C. A detailed derivation of this formula is given in the Appendix.

A second coordinate system defined in the plane of the cross section (see Fig. 1) is particularly convenient for describing certain quantities that appear in the analysis. Let O be a fixed point within C and $P = P(s)$ be an arbitrary point on C itself. Then P can be described by giving $r = r(s)$, the distance from O to the tangent to C at P, and $\rho = \rho(s)$, the distance from O to the normal to C at P. The functions r and ρ are not independent of one another but are related by two differential equations that are derived in the Appendix—namely,

$$(dr/ds) + (\rho/R) = 0 \qquad (2)$$

$$(d\rho/ds) - (r/R) + 1 = 0 \qquad (3)$$

where R is again the radius of curvature of C at P. These relations will be found useful in discussing the properties of certain components of the strain tensor.

Analysis of Strain

The displacements arising in the tube are assumed to be of the same form as those appearing in the Saint-Venant solution of the elastic torsion problem—that is, the displacements of a cross section consist of a small rotation about an axis parallel to the z-axis through an angle of θ radians per unit length of the cylinder and a displacement of each point of the cross section in the direction of the z-axis. The vertical displacement or warping function w is supposed to be independent of z; in other terms, $w = w(s, n)$.

At a given point in the cross section, the displacement in the s-direction will be denoted u_s, that in the n-direction by u_n, and that in the z-direction by u_z. The fixed point O, used in defining the functions $r(s)$ and $\rho(s)$, will be taken as the intersection of the axis of rotation with the plane of the cross section in question. Thus the components of the displacement vector will be given by

$$\left.\begin{aligned} u_s &= (r + n)\theta z \\ u_n &= \rho\theta z \\ u_z &= w(s, n) \end{aligned}\right\} \qquad (4)$$

Now the physical components of the strain tensor, $\epsilon_{\alpha\alpha}$, $\epsilon_{\alpha\beta}$, etc., in an arbitrary orthogonal curvilinear coordinate system, α, β, γ, are given by the following formulas:[6]

$$\left.\begin{aligned} \epsilon_{\alpha\alpha} &= h_1 \frac{\partial u_\alpha}{\partial \alpha} - h_2 \frac{\partial \log h_1}{\partial \beta} u_\beta - h_3 \frac{\partial \log h_1}{\partial \gamma} u_\gamma \\ \epsilon_{\beta\gamma} &= \frac{1}{2}\left[\frac{h_2}{h_3}\frac{\partial}{\partial \beta}(h_3 u_\gamma) + \frac{h_3}{h_2}\frac{\partial}{\partial \gamma}(h_2 u_\beta)\right] \end{aligned}\right\} \qquad (5)$$

etc., where the element of arc length is given by

$$dl^2 = (d\alpha^2/h_1^2) + (d\beta^2/h_2^2) + (d\gamma^2/h_3^2) \qquad (6)$$

Eqs. (5) can be evaluated for the case in question if the coordinates α, β, γ are replaced by s, n, z, respectively. From Eqs. (1) and (6), it follows that

$$h_1 = [1 + (n/R)]^{-1}, \quad h_2 = 1, \quad h_3 = 1$$

Therefore,

$$\left.\begin{aligned} \epsilon_{ss} &= \frac{1}{1 + (n/R)}\frac{dr}{ds}\theta z + \frac{\partial}{\partial n}\{\log [1 + (n/R)]\}\rho\theta z \\ \epsilon_{sn} &= \frac{1}{2}\left\{[1 + (n/R)]\frac{\partial}{\partial n}\left[\frac{r + n}{1 + (n/R)}\theta z\right] + \frac{1}{1 + (n/R)}\frac{\partial}{\partial s}(\rho\theta z)\right\} \\ \epsilon_{nz} &= (1/2)\,[(\partial w/\partial n) + \rho\theta] \\ \epsilon_{zs} &= \frac{1}{2}\left\{\frac{1}{1 + (n/R)}\frac{\partial w}{\partial s} + [1 + (n/R)]\frac{\partial}{\partial z}\left[\frac{(r + n)\,\theta z}{1 + (n/R)}\right]\right\} = \frac{1}{2}\left[\frac{1}{1 + (n/R)}\frac{\partial w}{\partial s} + (r + n)\,\theta\right] \\ \epsilon_{nn} &= 0 \\ \epsilon_{zz} &= 0 \end{aligned}\right\} \qquad (7)$$

Now ϵ_{ss} measures the change in length of an infinitesimal vector in the s-direction divided by the original length of the vector, ϵ_{sn} is one-half the change in the angle between the s and n directions after deformation, and similarly for the other components. As a consequence of the assumed displacements, all the strains except ϵ_{zs} and ϵ_{zn} should vanish identically. This has been shown to be the case for ϵ_{nn} and ϵ_{zz} and will be verified directly for the strains ϵ_{sn} and ϵ_{ss}. It is assumed, furthermore, that the cylinder wall is so thin that it will not support stresses in the direction of the vector n—that is, the shear stress τ_{nz} is zero. Consequently, the corresponding shear strain, ϵ_{nz}, can be expected to vanish. Now

$$\epsilon_{ss} = \left[\frac{1}{1 + (n/R)}\frac{dr}{ds} + \frac{1}{1 + (n/R)}\frac{\rho}{R}\right]\theta z = \frac{\theta z}{1 + (n/R)}\left(\frac{dr}{ds} + \frac{\rho}{R}\right) = 0$$

from Eq. (2). Similarly,

$$\epsilon_{sn} = \frac{1}{2}\left[1 - \frac{(r + n)/R}{1 + (n/R)} + \frac{1}{1 + (n/R)}\frac{d\rho}{ds}\right]\theta z = \frac{\theta z}{2[1 + (n/R)]}\left\{1 + (n/R) - [(r + n)/R] + \frac{d\rho}{ds}\right\} =$$

$$\frac{\theta z}{2[1 + (n/R)]}\left(1 - \frac{r}{R} + \frac{d\rho}{ds}\right) = 0$$

from Eq. (3). The condition that ϵ_{nz} vanishes implies that

$$(\partial w/\partial n) + \rho\theta = 0$$

This equation can be integrated directly, since neither ρ nor θ depends on n; hence,

$$w = -\rho\theta n + f(s) \tag{8}$$

where $f(s)$ is an arbitrary function of s which must be determined. It may be assumed, without loss of generality, that $f(0) = 0$. Eq. (8) shows that the warping function w always varies linearly across a normal to the reference line; the slope depends only on the geometry of the cross section and the angle of twist, whereas the constant term must be determined from the stress-strain relations.

Finally ϵ_{sz} is one-half the shearing strain γ as usually, employed in technical literature. Since the radius of curvature R is large compared to the wall thickness for most of the practical beam shapes, the shearing strain can be written in the following form if powers of (n/R) of the second degree and higher are ignored in Eq. (7):

$$\gamma = [1 - (n/R)]\,(\partial w/\partial s) + (r + n)\theta \tag{9}$$

Analysis of Stress

It has been assumed in the discussion of the strains existing in the tube that only the shearing stress τ_{sz} exists. Since the corresponding strain is independent of z, $\tau_{sz} = \tau(s, n)$. Under this hypothesis, the boundary condition that the surface of the tube be free from stress will not be fulfilled exactly. The boundary condition would be satisfied if the walls were parallel to the reference line. This assumption implies, then, that the walls are almost parallel to the reference line; the surface conditions will be met only to within this order of approximation.

Consider the equilibrium of an element of the cylinder obtained by taking two sections normal to the reference line C at a distance ds apart measured along C (see Fig. 2). If H is the total height of the cylinder, equilibrium of vertical forces requires that

$$H\int \tau(s + ds, n)\,dn = H\int \tau(s, n)\,dn \tag{10}$$

where the first integral is taken over the thickness $t(s + ds)$ at $s + ds$ and the second is taken over the thickness $t(s)$ at s. It is customary to call the integral

$$T(s) = \int \tau(s, n)dn$$

the *shear flow* because of its analogy to similar terms in hydrodynamics. Eq. (10) may then be rewritten as

$$T(s + ds) = T(s) \text{ or } T(s) = \text{const.}$$

that is, the shear flow is constant throughout the whole cross section. This constant will be denoted simply by T.

In addition, the *mean shearing stress*, $\tau^*(s)$, will be defined by the relation

$$\tau^*(s) = [1/t(s)]\int \tau(s, n)dn = T/t(s) \tag{11}$$

Since the distribution of shearing stress across the wall may be expected to be well behaved, the shearing stress along the reference line, $\tau(s, 0)$, will approximate the mean shearing stress provided the reference line is more or less centrally located between the outer and inner cylindrical surfaces. In the elastic case, the curve C could be determined by this requirement, since the shear distribution across a normal will be a linear function of the applied torque Q. Once C is determined for a single value of Q, it would remain the same for any other value. This will not be true beyond the elastic range, since the position of C will shift in general with Q because of the nonlinearity of the stress-strain relation. Thus, it must be specifically assumed that, independent of the stress-strain law, $\tau^*(s) = \tau(s, 0) =$

$\tau(s, n)$ on C to within the order of approximations considered here.

A closed, thin-walled, single-cell tube is statically determinate in the sense that the shear flow T can be found from the applied torque Q without any reference to the stress-strain law. The distribution of the shearing stress along a normal to C, however, cannot be found without considering the strains involved. The resultant torque Q about a point O within the cross section (see Fig. 1) can be readily computed, for it is simply

$$Q = \int_0^l \int_{n_0(s)}^{n_1(s)} \tau(s, n)\,[r(s) + n]\,dn\,ds \qquad (12)$$

As in the previous section, $r(s)$ is the distance from O to the tangent to C at s; $n_0(s)$ is the coordinate of the point on the inner wall corresponding to s; $n_1(s)$ is that of the corresponding point on the outer wall; and l is the total length of C. The integral in Eq. (12) can be split into two parts—namely,

$$Q = \int_0^l \int_{n_0(s)}^{n_1(s)} \tau(s, n)r(s)\,dn\,ds + \int_0^l \int_{n_0(s)}^{n_1(s)} \tau(s, n)n\,dn\,ds \qquad (13)$$

The second integral in Eq. (13) is small compared to the first for most technically important sections and can be neglected. Since

$$\int_{n_0}^{n_1} \tau(s, n)r(s)\,dn = r(s)T$$

the torque may be expressed as

$$Q = \int_0^l \int_{n_0(s)}^{n_1(s)} \tau(s, n)r(s)\,dn\,ds = T\int_0^l r(s)\,ds \qquad (14)$$

Eq. (14) is equivalent to assuming that the actual shear stresses may be replaced by the shear flow concentrated along C for the purpose of computing the torque. Since $(1/2)r(s)ds = dA$, the element of area in the r, s coordinate system

$$Q = 2AT \qquad (15)$$

where A is the total area enclosed by C. Given the applied torque Q, T can be found from Eq. (15) without reference to the stress-strain law. The relation between Q and T is the same for both the elastic and the plastic range. The actual distribution of $\tau(s, n)$ cannot be determined from this result alone; the succeeding section will deal with this problem. Finally, the relation between Q and T is independent of the position of the point O, and thus any point may be used as origin within the curve C.

Stress-Strain Relations

As has been pointed out in the previous sections, only one component of stress and one component of strain (the shearing stress and corresponding shearing strain) need be considered. Accordingly, then, the only characteristic of the material which is required is the shear stress vs. shear strain curve. It is assumed that the function†

$$\tau(s, n) = g[\gamma(s, n)] \qquad (16)$$

has an inverse that will be denoted by

$$\gamma(s, n) = h[\tau(s, n)] \qquad (17)$$

Since the sign of τ and γ can be chosen arbitrarily, both g and h must be odd functions of their arguments; consequently, $g(0) = h(0) = 0$. Within the elastic limit, Eq. (16) can be written in the form

$$\tau(s, n) = G\,\gamma(s, n)$$

where the constant G is the modulus of rigidity of the material. Since the problem concerns only loading, nothing will be said about the equation or conditions governing unloading and permanent set.

Along the curve C, $n = 0$; the shear strain at points of C is given by $\gamma(s, 0)$ and the shear stress by $\tau(s, 0) = \tau^*(s)$. Thus, from Eqs. (9) and (17),

$$\gamma(s, 0) = \frac{\partial w(s, 0)}{\partial s} + r\theta = h[\tau^*(s)] \qquad (18)$$

On the other hand, Eq. (8) states that

$$\frac{df}{ds} = \frac{\partial w(s, 0)}{\partial s} = h[\tau^*(s)] - r\theta$$

or

$$f(s) = \int_0^s h[\tau^*(s)]ds - \theta\int_0^s r(s)\,ds$$

Therefore, Eq. (8) becomes

$$w(s, n) = -\rho\theta n + \int_0^s h\,[\tau^*(s)]\,ds - \theta\int_0^s r(s)\,ds$$

Now $\tau^*(s) = T/t(s)$ by definition [Eq. (11)] and $T = Q/2A$ [Eq. (15)]; consequently, the warping function may be expressed in terms of the applied torque Q and resultant angle of twist θ as

$$w(s, n) = -\rho\theta n + \int_0^s h\left[\frac{Q}{2At(s)}\right]ds - \theta\int_0^s r(s)\,ds \qquad (19)$$

Once a relation is found between Q and θ, the warping function can be expressed solely in terms of one of these parameters. For this purpose, consider Eq. (18) integrated along the total length of C,

† A more general stress-strain law of the form $\dot{\tau} = g(\gamma, \tau)\dot{\gamma}$, where $\dot{\tau}$ and $\dot{\gamma}$ are the first derivatives of τ and γ with respect to some homogeneous parameter, might also be considered. With reasonable assumptions on the function g, however, this equation can be integrated with respect to the parameter and rewritten in the form of Eq. (16).

$$\oint \frac{\partial w(s, 0)}{\partial s}\, ds + \theta \oint r ds = \oint h\,[\tau^*(s)] ds$$

The warping function must be a single-valued, periodic function of the total length of C; accordingly, the first integral vanishes. It has been previously pointed out that the second integral has the value $2A$. Therefore,

$$\theta = \frac{1}{2A} \oint h\left[\frac{Q}{2At(s)}\right] ds \tag{20}$$

In the elastic case, $h(\tau) = \tau/G$; thus Eq. (20) reduces to the following expression:

$$\theta = (Q/4A^2G) \oint [ds/t(s)] \tag{21}$$

in the elastic range. Eq. (21) is one of the classical Bredt formulas.[5] It is natural then to introduce an artificial thickness function $t'(s)$ defined by

$$t'(s) = Q/2AGh[Q/2At(s)]$$

Then, Eq. (20) reduces to a generalized Bredt's formula—namely,

$$\theta = (Q/4A^2G) \oint [ds/t'(s)] \tag{22}$$

which is valid for a general shear stress-shear strain relation.

Similarly, the warping function $w(s, n)$ within the elastic limit is given by

$$w(s, n) = -\rho\theta n + \frac{Q}{2AG}\int_0^s \frac{ds}{t(s)} - \theta \int_0^s r(s)\, ds \tag{23}$$

Introduction of the artificial thickness function $t'(s)$ reduces the general formula for the warping function [Eq. (19)] to

$$w(s, n) = -\rho\theta n + \frac{Q}{2AG}\int_0^s \frac{ds}{t'(s)} - \theta \int_0^s r(s)\, ds \tag{24}$$

The shearing strain can be evaluated by substituting Eq. (19) into Eq. (9),

$$\begin{aligned}\gamma(s, n) &= \left(1 - \frac{n}{R}\right)\left\{-n\theta \frac{d\rho}{ds} + h\left[\frac{Q}{2At(s)}\right] - \theta r\right\} + (r + n)\theta \\ &= \left(1 - \frac{n}{R}\right)\left\{n\theta\left(1 - \frac{r}{R}\right) + h\left[\frac{Q}{2At(s)}\right] - \theta r\right\} + (r + n)\theta\end{aligned}$$

from Eq. (3). Finally,

$$\gamma(s, n) = \left(1 - \frac{n}{R}\right) h\left[\frac{Q}{2At(s)}\right] + n\theta\left(2 - \frac{n}{R} + \frac{nr}{R^2}\right) \tag{25}$$

In the elastic range,

$$\gamma(s, n) = \left(1 - \frac{n}{R}\right)\left[\frac{Q}{2AGt(s)}\right] + n\theta\left(2 - \frac{n}{R} + \frac{nr}{R^2}\right) \tag{26}$$

and with the introduction of the artificial thickness function, Eq. (25) becomes

$$\gamma(s, n) = \left(1 - \frac{n}{R}\right)\left[\frac{Q}{2AGt'(s)}\right] + n\theta\left(2 - \frac{n}{R} + \frac{nr}{R^2}\right) \tag{27}$$

Comparison of Eq. (21) with Eq. (22), Eq. (23) with Eq. (24), and Eq. (26) with Eq. (27) shows that the angle of twist vs. applied torque relation, the warping function, and the shear strain for a material with a *general stress strain* law can be found by solving the *elastic torsion* problem for a tube with a thickness function given by $t'(s)$. Unfortunately, the thickness of the equivalent elastic tube is a nonlinear function of the applied torque Q; thus, a different elastic tube must be studied for each value Q desired. The distribution of shear stress does not follow this pattern, however, for in the elastic case it is given by

$$\tau(s, n) = \left(1 - \frac{n}{R}\right)\left[\frac{Q}{2At(s)}\right] + n\theta G\left(2 - \frac{n}{R} + \frac{nr}{R^2}\right)$$

whereas in the nonelastic case it is

$$\tau(s, n) = g\left\{\left(1 - \frac{n}{R}\right)\left[\frac{Q}{2At'(s)}\right] + n\theta\left(2 - \frac{n}{R} + \frac{nr}{R^2}\right)\right\} \tag{28}$$

Finally, Eqs. (22), (24), (27), and (28) constitute a complete solution to the problem of finding the angle of twist, the warping function, and the distribution of shear stress and shear strain as a function of the applied torque.

Torque Versus Angle of Twist for Multicell Sections

By means of the results obtained in the previous section, it is possible to solve the technical problem of finding torque vs. angle of twist curves for multicell sections—that is, closed sections with several internal webs (see Fig. 5). The technique used by von Kármán and Christensen[7] for the elastic case will be generalized to stresses beyond the elastic limit.

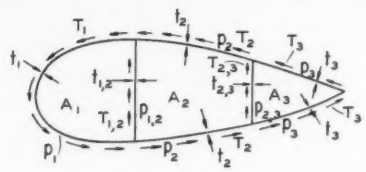

FIG. 3

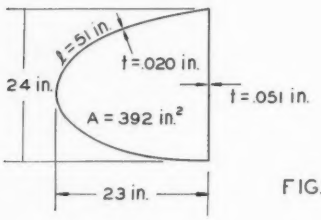

FIG. 4 a

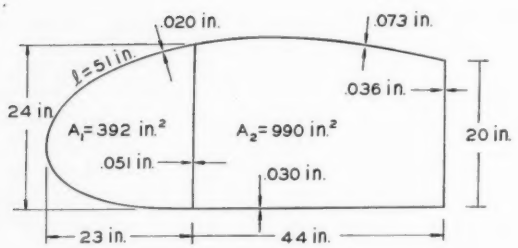

FIG. 4 b

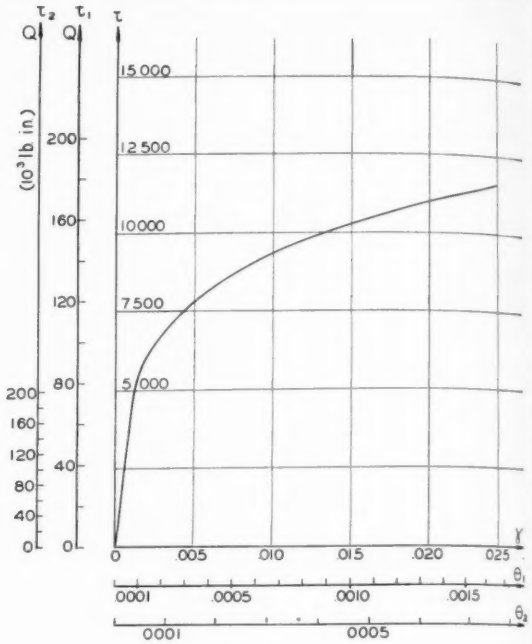

FIG 5

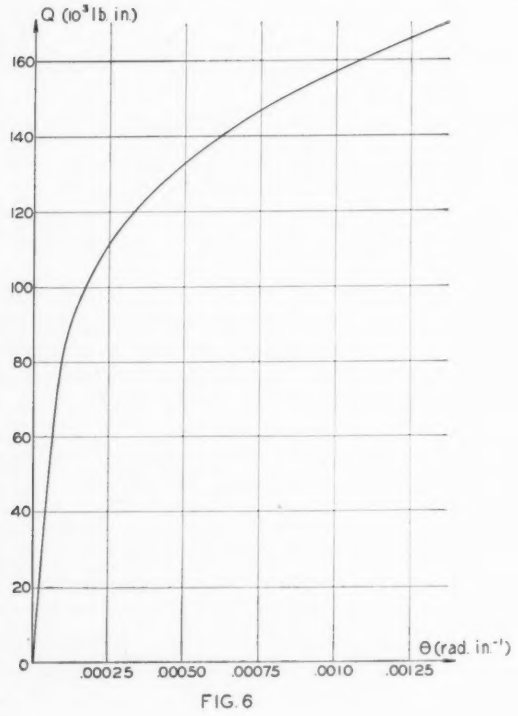

FIG. 6

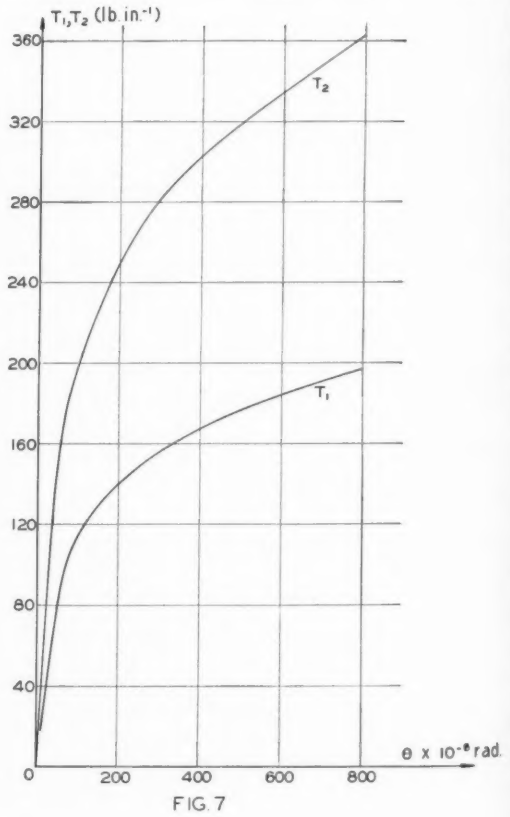

FIG. 7

The reference line of the outer cell and each of the interior webs will be defined in the same manner as in the first section. Let $p_{i,k}$ denote the reference line between the ith and kth sections and p_i denote the reference line of the remainder of the ith cell not included in the webs. The thickness function for the i-k web will be given by $t_{i,k}$ and that of the ith cell by t_i. The shear flows, T_i, in each section will have the same positive orientation (counterclockwise). The functions T_i will not, in general, be continuous at the junction points, but the resulting stress concentrations will be ignored in the computation of the total applied torque, as in the elastic case. The shear flow in the i-k web will be denoted by $T_{i,k}$. Finally, the area of the ith cell will be given by A_i.

The proof, given in the third section, that the shear flow is constant holds equally well for each cell of the multicell section. If the positive sense of $T_{i,k}$ is taken to be the same as T_i, then the equilibrium conditions at the junction of the web yield

$$T_{i,\,k} = T_i - T_k \tag{29}$$

Each cell must have the same angle of twist θ per unit length as the whole section; therefore, Eqs. (15), (26), and (29) may be applied to each cell, in turn, to give, for an n-cell section,

$$\left.\begin{aligned}
2A_1\theta &= \int_{p_1} h\left[\frac{T_1}{t_1(s)}\right]ds + \int_{p_{1,2}} h\left[\frac{T_1 - T_2}{t_{1,2}(s)}\right]ds \\
2A_2\theta &= \int_{p_2} h\left[\frac{T_2}{t_2(s)}\right]ds - \int_{p_{1,2}} h\left[\frac{T_1 - T_2}{t_{1,2}(s)}\right]ds + \int_{p_{2,3}} h\left[\frac{T_2 - T_3}{t_{2,3}(s)}\right]ds \\
&\cdots\cdots\cdots\cdots\cdots\cdots\cdots\cdots\cdots\cdots\cdots\cdots\cdots\cdots\cdots\cdots\cdots\cdots\cdots\cdots\cdots\cdots \\
2A_i\theta &= \int_{p_i} h\left[\frac{T_i}{t_i(s)}\right]ds - \int_{p_{i-1,i}} h\left[\frac{T_{i-1} - T_i}{t_{i-1,i}(s)}\right]ds + \int_{p_{i,\,i+1}} h\left[\frac{T_i - T_{i+1}}{t_{i,\,i+1}(s)}\right]ds \\
&\cdots\cdots\cdots\cdots\cdots\cdots\cdots\cdots\cdots\cdots\cdots\cdots\cdots\cdots\cdots\cdots\cdots\cdots\cdots\cdots\cdots\cdots \\
2A_n\theta &= \int_{p_n} h\left[\frac{T_n}{t_n(s)}\right]ds - \int_{p_{n-1,n}} h\left[\frac{T_{n-1} - T_n}{t_{n-1,n}(s)}\right]ds
\end{aligned}\right\} \tag{30}$$

where the integration is taken over the web or remainder of the cell designated by the subscript on the integral. Eqs. (30) constitute the nonlinear analogs of the linear, algebraic equations for the T_i found by von Kármán and Christensen in the elastic case.

Finally, the total applied torque can be found by adding the torque produced in each cell as computed from Eq. (15)—namely,

$$Q = 2\sum_{i=1}^{n} A_i T_i \tag{31}$$

Eqs. (30) and (31) will give a complete solution of the problem of finding the angle of twist per unit length as a function of the applied torque. Normally, the computation is carried out by selecting a value of θ, finding the shear flows from Eqs. (30), and then finding the torque produced from Eq. (31).

The next section contains an application of these methods.

Application to Sections of Piecewise Constant Thickness

Most technically important sections are ones in which the thickness function is piecewise constant. The computation problem is somewhat simplified for shapes of this type. Two examples, taken from the paper[8] of Paul Kuhn,† will be considered. One section consists of a single cell; the other, of two cells.

The single cell, shown in Fig. 4a, can be simply analyzed through a suitable modification of the scales on the stress-strain diagram, for in this case Eq. (20) can be written as

$$\theta = \frac{1}{2A}\left[l_1 h\left(\frac{Q}{2At_1}\right) + l_2 h\left(\frac{Q}{2At_2}\right)\right] \tag{32}$$

where l_1 is the length of the reference line of the portion of thickness t_1 and l_2 is the length of the reference line of the portion of thickness t_2. Eq. (32) states that the angle of twist can be found by adding together two shearing strains: one shearing strain is $l_1/2A$ times the shearing strain that corresponds to a shearing stress of magnitude $Q/2At_1$, while the second shearing strain is $l_2/2A$ times the shearing strain that corresponds to a shearing stress of magnitude $Q/2At_2$. Consider, for example, the shear stress vs. shear strain curve shown in Fig. 5. This curve has been modified by adding two scales to the vertical axis and two corresponding scales to the horizontal axis. The first vertical scale is found by replacing the τ scale by a corresponding scale marked off in terms of Q by means of the relation

$$\tau = \tau_1 = Q/2At_1$$

† The first example is simply the leading edge cell of the second example.

The corresponding horizontal scale, θ_1 scale, can be determined by the relation

$$\theta_1 = \gamma l_1/2A$$

The other pair of scales are found in exactly the same fashion from the equations

$$\tau = \tau_2 = Q/2At_2, \quad \theta = \gamma l_2/2A$$

For the particular section studied, the constants have the values $A = 392$ sq. in., $l_1 = 51$ in., $t_1 = 0.020$ in., $l_2 = 24$ in., and $t_2 = 0.051$ in. The Q vs. θ graph for the whole section can then be determined by picking a value of Q, finding this Q value on the τ_1 scale, and finding the corresponding θ_1 value from the stress-strain curve and the θ_1 scale. Similarly, θ_2 is determined by reading off the value on the θ_2 scale which corresponds to the given Q reading on the τ_2 scale. Finally, θ is found from Eq. (32) by adding θ_1 and θ_2. In this manner, the Q vs. θ graph can be readily found; the results of the computation are given in Table 1 and are shown in Fig. 6.

The two-celled cross section shown in Fig. 4b cannot be handled so simply, for it reflects the essential nonlinearity of the problem. Eq. (30) becomes, in this case,

$$2A_1\theta = \int_{p_1} h\left(\frac{T_1}{t_1}\right) ds + \int_{p_{1,2}} h\left(\frac{T_1 - T_2}{t_{1,2}}\right) ds$$

$$2A_2\theta = \int_{p_2} h\left(\frac{T_2}{t_2}\right) ds - \int_{p_{1,2}} h\left(\frac{T_1 - T_2}{t_{1,2}}\right) ds$$

Since t_1, t_2, and $t_{1,2}$ are piecewise constant functions, these equations may be readily integrated; in terms of the constants shown in Fig. 4b, they become

$$\left.\begin{aligned} 784\theta &= 51h\left(\frac{T_1}{0.020}\right) + 24\,h\left(\frac{T_1 - T_2}{0.051}\right) \\ 1{,}980\theta &= 44h\left(\frac{T_2}{0.073}\right) + 20h\left(\frac{T_2}{0.036}\right) + \\ &\quad 44h\left(\frac{T_2}{0.030}\right) - 24h\left(\frac{T_1 - T_2}{0.051}\right) \end{aligned}\right\} \quad (33)$$

The computation problem is somewhat simplified if these relations are written in the form

$$\gamma^*(T_2) = 2{,}764\theta - 51h(T_1/0.020)$$

$$51h(T_1/0.020) = 784\theta - 24h\,[(T_1 - T_2)/0.051]$$

where

$$\gamma^*(T_2) = 44h(T_2/0.073) + 20h(T_2/0.036) + 44h(T_2/0.030)$$

The functions $51h(T_1/0.020)$, $24h[(T_1 - T_2)/0.051]$, and $\gamma^*(T_2)$ can be plotted as functions of the arguments T_1, $T_1 - T_2$, and T_2, respectively, by simple modifications of the stress-strain curve of Fig. 5 as in the previous example. Once these curves have been obtained, a rather simple iteration scheme can be employed to find T_1 and T_2 for a given value of θ. Let $T_1^{(n)}$ and $T_2^{(n)}$ denote the nth approximation for T_1 and T_2. Then the $(n+1)$ approximation can be obtained from

$$\left.\begin{aligned} 51h(T_1^{(n+1)}/0.020) &= 784\theta - \\ &\quad 24h[(T_1^{(n)} - T_2^{(n)})/0.051] \\ \gamma^*(T_2^{(n+1)}) &= 2{,}764\theta - 51h(T_1^{(n+1)}/0.020) \end{aligned}\right\} \quad (34)$$

where the values $T_1^{(n+1)}$, $T_2^{(n+1)}$ can be found from the graphs just described.

In practice, it has been found convenient to compute the T_1, T_2 vs. θ curves in the following manner. The points are computed successively for increasing values of θ. For the first value of θ, the first approximation in Eqs. (34) for $T_1 - T_2$ was taken to be zero. For succeeding values of θ, the first approximation taken for $T_1 - T_2$ was the final value of this difference obtained from the computation for the preceding value of θ. To within the order of accuracy used, the first stage of the iteration scheme required five steps; from this point on, only three steps were required for each point. If errors are committed in the computations, the process will still converge, although a little more slowly. A formal proof of the convergence can be given in the standard fashion. Finally, the torque vs. angle of twist per unit length curve can be found by evaluating Eq. (31) for the section in question—that is,

$$Q = 784T_1 + 1{,}980\,T_2$$

The results of the computation are given in Table 2 and are plotted in Figs. 7 and 8.

TABLE 1

Q (10^3 lb. in.)	θ (rad. in.$^{-1}$)
0	0
20	0.000186
40	0.000435
60	0.000661
80	0.000929
100	0.001694
120	0.003430
140	0.006230
160	0.010750
180	0.017080

TABLE 2

Angle of Twist per Unit Length [θ (rad. in.$^{-1}$ × 10^{-6})]	Shear Flows [T_1 (lb. in.$^{-1}$)]	[T_2 (lb. in.$^{-1}$)]	Torque Q (lb. in. × 10^3)
0	0	0	0
25	43.0	77.0	186.2
37	61.0	114.0	273.5
50	78.0	153.0	364.1
100	114.7	199.0	483.9
150	129.0	227.3	551.2
200	140.0	250.9	606.5
250	148.5	268.5	647.7
300	155.8	282.2	630.9
350	162.0	293.4	707.9
400	167.2	302.5	730.0
450	172.0	311.0	750.6
500	176.3	319.0	769.8
550	180.4	326.0	786.9
600	184.2	333.5	804.7
650	187.7	340.0	820.4
700	191.0	347.2	837.2
750	194.2	354.2	853.6
800	197.0	361.5	870.2

Appendix

(a) *The Derivation of Eq. (1)*

The line element dl, in the t, n, z coordinate system can be found by considering two points, one A with coordinates (s, n, z) and the other B with coordinates $(s + ds, n + dn, z + dz)$. The projection of B in the cross-section plane containing A will be denoted by B' (see Fig. 9). This point has the coordinates $(s + ds, n + dn, z)$. In terms of the auxiliary points shown in Fig. 9,

$$dl^2 = \overline{AB'}^2 + dz^2$$

and

$$\overline{AB'}^2 = \overline{AC}^2 + dn^2$$

Let $R(s)$ be the radius of curvature of the reference line at the point s. Then, by similar triangles,

$$\overline{AC} = [(R + n)/R]ds = [1 + (n/R)]ds$$

Therefore, the line element is given by Eq. (1)—that is,

$$dl^2 = [1 + (n/R)]^2 ds^2 + dn^2 + dz^2$$

(b) *The Proof of Identities (2) and (3).*

Consider a point P at s on the reference line C and a neighboring point on C,P', at $s + ds$ (see Fig. 10). The center of curvature of C corresponding to P will be denoted by K. The lines $\overline{OA}$ and $\overline{OA'}$ are perpendicular to $\overline{KP}$ and $\overline{KP'}$, respectively; therefore,

$$\overline{OA} = \rho, \quad \overline{OA'} = \rho + d\rho$$
$$\overline{AP} = r, \quad \overline{A'P} = r + dr$$
$$\overline{KP} = \overline{KP'} = R, \quad \overline{PP'} = ds$$
$$\text{ang. } (PKP') = \text{ang. } (AOA') = ds/R$$

Since triangle AOB is similar to triangle PKP',

$$\overline{OA}/\overline{KP} = \overline{AB}/\overline{PP'}, \quad \overline{OA}/\overline{KP} = \overline{OB}/\overline{KP'} \quad (35)$$

Now

$$\overline{AB} = \overline{AK} - \overline{BK} = r - R - (r + dr - R) \times \cos \text{ ang. } (PKP') = r - R - (r + dr - R) \times \cos (ds/R) = -dr$$

since higher order terms in ds/R can be neglected. The first of Eqs. (35) can be applied to yield

$$\rho/R = -dr/ds$$

or Eq. (2).

On the other hand,

$$\overline{OB} = \overline{OA'} - \overline{BA'} = \rho + d\rho - (r + dr - R) \tan (ds/R) = \rho + d\rho - (r + dr - R)(ds/R)$$

after higher order terms in ds/R are neglected. The second of Eqs. (35) can thus be written as

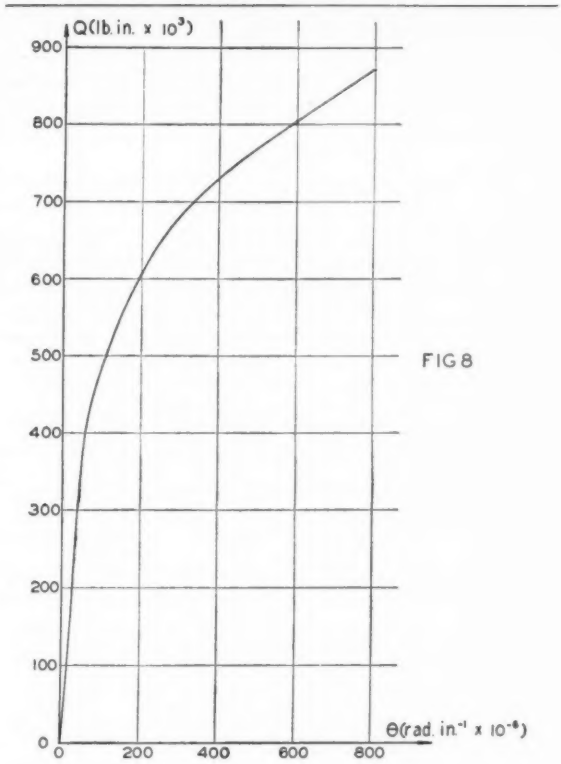

FIG 8

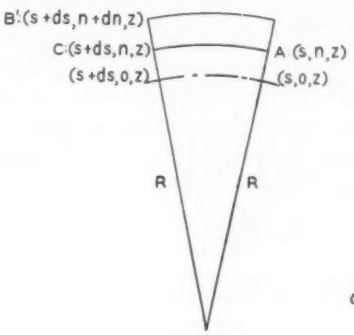

FIG. 9

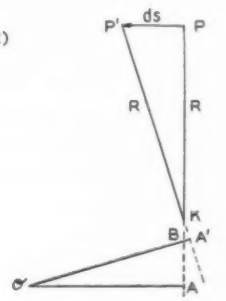

FIG. 10

$$\frac{\rho}{R} = \frac{\rho + d\rho}{R} - (r + dr - R)\frac{ds}{R^2}$$

that is,

$$(d\rho/ds) - (r/R) + 1 = 0 \quad (36)$$

since the product $drds$ is of higher order. Eq. (36) is identity (3).

References

[1] Prescott, J., *Applied Elasticity*, p. 165; Longmans, Green, and Company, London, 1924.

[2] Timoshenko, S., *Strength of Materials, II*, 2nd Ed., p. 278; D. Van Nostrand Company, New York, 1941.

(*Continued on page 518*)

Column Buckling in the Elastoplastic Range

P. CICALA*

Córdoba, Argentina

SUMMARY

A theory of inelastic buckling of a column of constant, H-shaped section is presented and an approximate procedure of solution indicated. The numerical application confirms qualitatively the results found by Shanley on the idealized semirigid strut. On this last simplified scheme the effect of initial eccentricities is investigated and Southwell's plot analyzed. Considering the curvature of the stress-strain characteristic, it appears that, in accordance with experimental observations, the load decreases with increasing deflections after reaching a value that, for small initial eccentricities, may not attain the tangent-modulus value.

INTRODUCTION

THE STUDY OF COLUMN BUCKLING in the inelastic range has received an important contribution from Shanley's paper,[1] which showed that the buckling process of a straight column starts at the tangent-modulus load. Shanley analyzed the problem on an extremely simplified scheme, considering the column as initially straight, supposing only a short central section to be deformable, and neglecting the curvature of the stress-strain diagram. In the present paper, this same problem is investigated in a more general form, and the three mentioned simplifications are separately removed. The results confirm and extend the conclusions reached by Shanley; furthermore, they afford a fuller explanation of experimental observations and eliminate some doubts and objections[2] that the mentioned paper had aroused.

ANALYSIS

The Column of Constant Cross Section

The section of the strut is supposed to be concentrated in two equal flanges, at distance $2a$ apart, the web area being considered as negligible. Let A be the area of each flange and L be the strut length between end hinges (Fig. 1). Under the compressive load P, the axis of the strut, initially straight, deflects in the plane of symmetry parallel to the web. Quantities corresponding to flange 1 (on the concave side) are distinguished by subscript 1, while subscript 2 refers to the opposite flange.

In a section whose deflection is denoted by ay, the flange loads are

$$P_1 = (1/2)P(1 + y), \qquad P_2 = (1/2)P(1 - y) \quad (1)$$

Let ϵ_1, ϵ_2 be the corresponding strains and x be the axial coordinate measured from the mid-section and referred to the half-strut length. Variable quantities are considered as functions of the parameters x and P. Compressive stresses and strains are considered as positive. Thus, we write

$$(4a/L^2)\ (\partial^2 y/\partial x^2) = (\epsilon_2 - \epsilon_1)/2a \quad (2)$$

The stress-strain relations are represented in Fig. 2. When P increases, the load in both flanges increases and the representative points lie on the stress-strain characteristic of the material (line cc). If the load on one flange is decreasing, the representative point departs from line cc along a line whose slope is E. We call "regression zone" the part of the strut where $\partial P_2 \div \partial P < 0$. Section s-s (Fig. 1) is supposed to be taken in this zone, the corresponding state of stress being represented by points 1,2 on Fig. 2a. If the portion of the characteristic here involved may be represented by a straight segment of slope E_t, the stresses in the flanges are expressed by

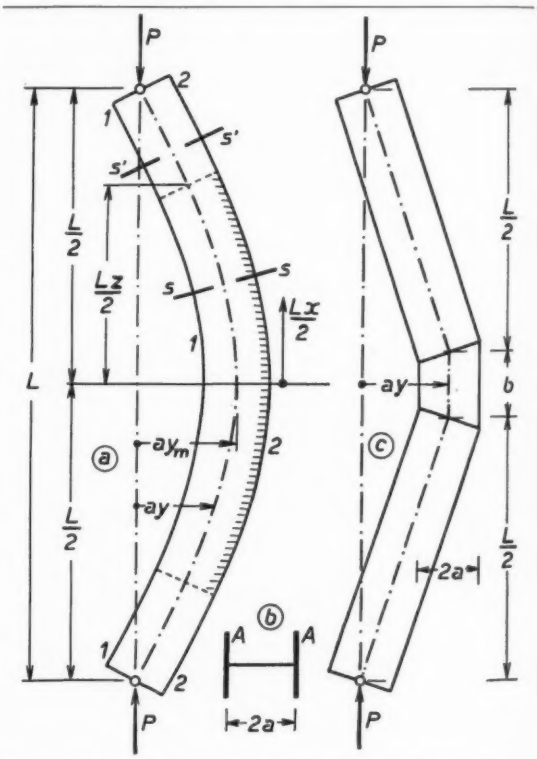

Fig. 1. Scheme and notation. (a) Constant section column. (b) Cross section. (c) Semirigid scheme.

Received November 28, 1949.

* Professor of the Politecnico di Torino. Now at the Instituto Aerotécnico and University of Córdoba.

$$\left.\begin{aligned}\sigma_1 &= P_1/A = \sigma_x + E_t(\epsilon_1 - \epsilon_x)\\ \sigma_2 &= P_2/A = \sigma_x + E(\epsilon_2 - \epsilon_x)\end{aligned}\right\} \quad (3)$$

where σ_x and ϵ_x are the coordinates of the point X of departure. From Eqs. (1), (2), and (3) we get

$$\frac{8AE_t a^2}{L^2}\frac{\partial^2 y}{\partial x^2} + \frac{k-1}{2k}(P - 2P_x) + \frac{k+1}{2k}Py = 0 \quad (4)$$

where

$$P_x = A\sigma_x, \quad k = E/E$$

Putting

$$\left.\begin{aligned}p^2 &= L^2P/8AE_ta^2, \quad q = L^2P_x/4AE_ta^2\\ \alpha^2 &= (k+1)/2k, \quad h = (k-1)/(k+1)\end{aligned}\right\} \quad (5)$$

Eq. (4) may be written as follows:

$$(1/\alpha^2)(\partial^2 y/\partial x^2) + p^2 y + h(p^2 - q) = 0 \quad (6)$$

where α, h are constants and q is a function of x. This equation is valid in the regression zone; denoting by y_m the value of y for $x = 0$, the solution may be expressed as follows:

$$y = \frac{\alpha h}{p}\int_0^x q(x')\sin \alpha p(x - x')dx' + (y_m + h)\cos \alpha px - h \quad (7)$$

according to symmetry with respect to section $x = 0$.

We call "progression zone" the parts of the strut where $\partial P_2/\partial P > 0$. For these portions of the column, which lie near the hinges, the fundamental equations take the simpler form that can be deduced from Eqs. (4) and (6) for $k = 1$. Therefore, in the upper portion of the column we have

$$y = C \sin p(1 - x) \quad (8)$$

We denote by z the relative coordinate of the sections that limit the regression zone. For $x = z$, Eqs. (7) and (8) must give the same values of y and $\partial y/\partial x$. These conditions yield the quantities C and y_m. For the first we get

$$C[\cos p(1 - z)\cos \alpha pz - \alpha \sin p(1 - z)\sin \alpha pz] = \alpha h \sin \alpha pz - \frac{\alpha^2 h}{p}\int_0^z q \cos \alpha px\, dx \quad (9)$$

From Eqs. (1), (8), and (9) the expression of P_2 may be deduced as a function of p and x, containing the quantities z, function of p, and q, function of the variable of integration. For the limiting section $x = z$

$$\partial P_2/\partial P = 0 \quad (10)$$

$$P_2 = P_x \quad (11)$$

According to Eqs. (5), Eq. (11) yields†

$$q = p^2 - Cp^2 \sin p(1 - z) \quad (12)$$

Hence, the following set of equations may be derived:

$$\left.\begin{aligned}&(q - p^2)p\cos p(1 - z) + (dq/dz)\sin p(1 - z) = 0\\ &\left(\alpha q - \frac{p^2}{\alpha}\right)p \sin \alpha pz + \frac{dq}{dz}\cos \alpha pz + \alpha^2 hp\int_0^z q\cos \alpha px\, dx = 0\end{aligned}\right\} \quad (13)$$

which define in an integrodifferential form the relation between the quantities p, z, and q.

† The argument of q may be called indifferently x or z.

The problem may be given an approximate solution by means of a step-by-step procedure based directly on Eqs. (10) and (11). The expression of P_2, as obtained from Eqs. (1), (8), and (9), satisfies the condition

$$\partial P_2/\partial z = 0$$

for $x = z$. Therefore, Eq. (10) reduces to

$$\partial q/\partial p = 0 \quad (14)$$

if this derivative is taken from Eq. (12), considering z as a constant and p as an independent variable. Thus, if the values $q_1, q_2, \ldots, q_i$ of q at stations $z_1 = 0, z_2, \ldots, z_i$ are known and if we express the integral that appears in Eq. (9) by Simpson's rule, the value of q at station z_{i+1} can be calculated immediately, from Eq. (12), as a function of p. Then, Eq. (14) defines p and, consequently, q.

The solution depends on one boundary condition—for instance, the value of p_0 of p for which $q = p^2$ (i.e., $y = 0$). This condition corresponds to the onset of buckling; under the initial value $p = p_0$, the regression zone reaches as far as section z_0 given by the equation

$$\tan \alpha p_0 z_0 \tan p_0(1 - z_0) = \alpha \quad (15)$$

For $p_0 = \pi/2$—that is, if the buckling starts at the tangent-modulus load represented by

$$P_t = 2\pi^2 AE_t a^2/L^2 \quad (16)$$

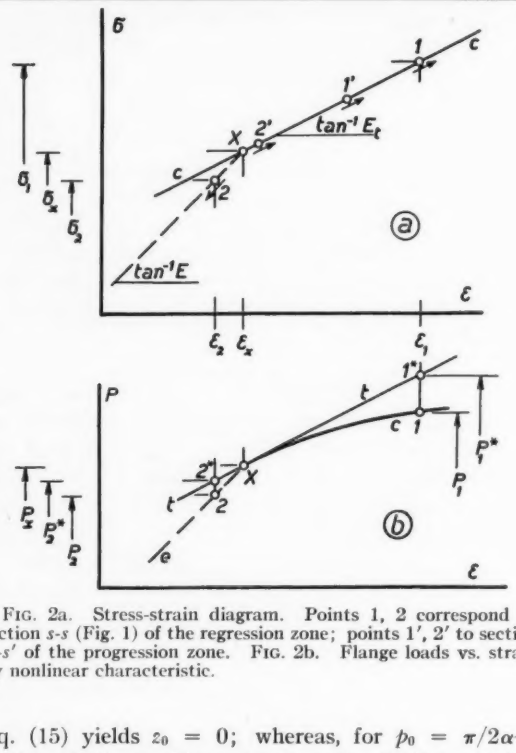

FIG. 2a. Stress-strain diagram. Points 1, 2 correspond to section *s-s* (Fig. 1) of the regression zone; points 1′, 2′ to section *s′-s′* of the progression zone. FIG. 2b. Flange loads vs. strain by nonlinear characteristic.

Eq. (15) yields $z_0 = 0$; whereas, for $p_0 = \pi/2\alpha$—that is, if the buckling starts at the double-modulus load P_t/α^2—the regression zone covers the entire strut at once. For values of $P < P_t$, no bent configuration of equilibrium exists. From the initial limits, the regression zone spreads out toward the ends of the column, while the deflections increase.

The most important case is that by which the buckling begins at $P = P_t$. In this case, expanding the solution of Eqs. (13) into power series of z gives

$$p = (\pi/2) + [\pi^3(k-1)/96k]z^3 + \dots$$
$$q = (\pi^2/4) + [\pi^6(k-1)/3{,}840k]z^5 + \dots \quad (17)$$

The results of calculations carried out for $k = 2$ are shown in Fig. 3. The dotted line b represents Eq. (15). Line a defines the variations of the regression zone for the fundamental case $p_0 = \pi/2$. Line c corresponds to $z_0 = 0.6$. The solution corresponding to $p_0 = \pi/2$ is also represented by the dotted lines a_1, a_2 of Fig. 4, which give the loads on the flanges as functions of the applied load at section $x = 0$.

The Semirigid Column

According to Fig. 1b, the strut is supposed to be formed by two rigid parts of equal length $L/2$ and a short central deformable section of length b. The deflection ay is supposed to be constant along the deformable portion; let y_0 be the value of y for $P = 0$ (initial eccentricity). Eq. (2) modifies in this case as follows:

$$(4a/Lb)\,(y - y_0) = (\epsilon_1 - \epsilon_2)/2a \quad (18)$$

while Eqs. (1) and (3) hold true. Thence,

$$P_t(y - y_0) = \frac{k-1}{2k}(P - 2P_x) + \frac{k+1}{2k}Py \quad (19)$$

where

$$P_t = 8AE_t a^2/Lb$$

In the particular case $y_0 = 0$, $P_x = P_t$, Eq. (19) agrees with Eq. (18) of Shanley's paper. Neglecting the curvature of the stress-strain diagram in the region implied, the same Eq. (19) holds below the regression point with $k = 1$, thus giving

$$y = y_0[P_t/(P_t - P)] \quad (20)$$

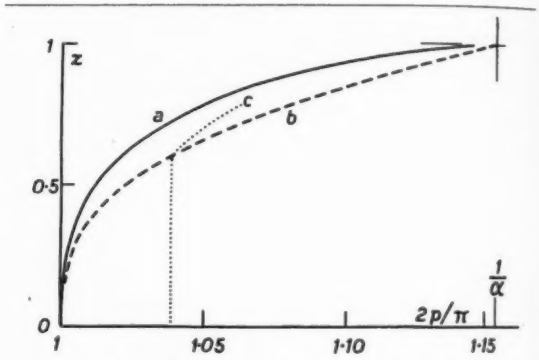

FIG. 3. Length of the regression zone vs. load parameter.

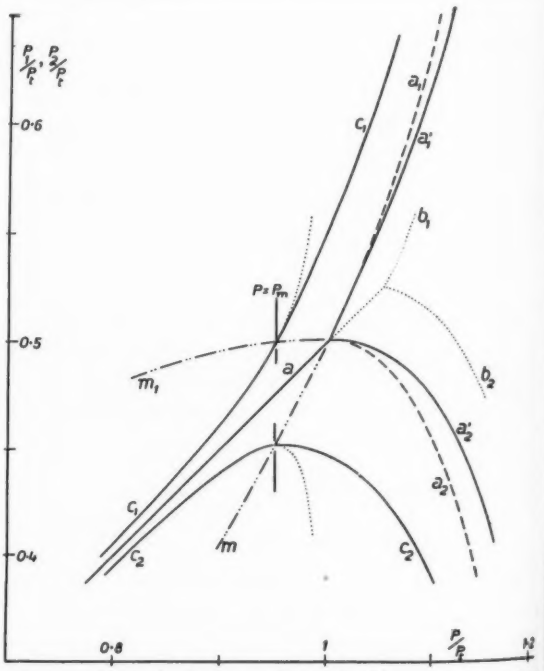

FIG. 4. Flange loads vs. applied load. Lines a_1, a_2: constant section column. Lines a_1', a_2': semirigid column, $y_0 = 0$. Lines c_1, c_2: semirigid column, $y_0 = 1/400$.

The value P_m of P, for which the reversal condition (namely, $dP_2/dP = 0$) is verified, results:

$$P_m = P_t(1 - \sqrt{y_0}) \tag{21}$$

Under this load, the stress σ_2 attains the value σ_x corresponding to point X where departure from the characteristic takes place (Fig. 2a). Thus, we obtain

$$P_x = P_m^2/2P_t \tag{22}$$

With this value of P_x, the column deflections for any load $P > P_m$ can be calculated from Eq. (19); thence, the flange loads can be computed according to Eqs. (1). The results of calculations carried out for $k = 2$ are resumed in Fig. 4, where the ratios P_1/P_t and P_2/P_t are plotted versus P/P_t. Lines c_1 and c_2 give, respectively, the values of P_1 and P_2 for $y_0 = 1/400$. The line m, whose equation is $P_2/P_t = P^2/2P_t^2$, represents the locus of maximum P_2. Its crossing divides line c_2 in two parts of different character: the "progression branch" ($P < P_m$), where Eq. (20) holds; and the "regression branch," where Eq. (19) is valid. The corresponding division on line c_1 is established by line m_1, whose equation is

$$P_1/P_t = (P/P_t) - (P^2/2P_t^2)$$

For any value of initial eccentricity, the regression branches have, as an asymptote, the vertical

$$P = P_r = 2kP_t/(k + 1)$$

For vanishing initial eccentricity, both progression branches tend jointly toward the straight line a ($P_1 = P_2 = P/2$), whereas the regression branches approach, respectively, lines a_1' and a_2', which are obtained from Eqs. (1) and (19) for $y_0 = 0$, $P_x = P_t$. For the initially straight column ($y_0 = 0$), from the same equations, other curves such as b_1, b_2 may be obtained if P_x is given any intermediate value between P_t and P_r. These lines represent the buckling process in the ideal case that the column be maintained straight until the tangent-modulus load is exceeded. They have practically no importance, since in no case are they approached by equilibrium lines representing the natural behavior of actual columns.†

It may be easily shown that, if the values of $(y - y_0)/P$ are calculated using Eq. (19) and plotted against $y - y_0$ according to Southwell's representation, we obtain a curve whose slope tends asymptotically to $1/P_r$. A simpler representation is reached using the form of this plot as modified by Lundquist.[3] In this case the parameters following are introduced:

$$u = (y - y')/(P - P'), \quad v = y - y' \tag{23}$$

where y' is the deflection that corresponds to a load P' arbitrarily chosen. Taking $P' > P_m$, we get from Eq. (19)

$$(P_r - P')u - v = y' + h \tag{24}$$

Except for the constant term h, the equation is the same as if the material were elastic and the critical load were P_r.

The Case of Nonlinear Stress-Strain Relation

The buckling process can be easily analyzed if the idealization referred to in Fig. 1b is adopted. The flange loads are plotted versus the relative shortening of the same fibers in Fig. 2b. For increasing strain, the relation is represented by line c, according to the properties of the material; line t is the tangent to c at point X, whence the representative point for flange 2 departed along line e. Taking into account Eqs. (1), Eq. (18) may be written as follows:

$$P_t[(P_1 - P_2)/(P_1 + P_2) - y_0] = P_1^* - P_2^* \tag{25}$$

where P_1^* and P_2^* are the loads that, on the tangent t, correspond to the strains that actually exist in the flanges. For a given P_1, the value of P_1^* may be read on the diagram, while P_2^* may be expressed by

$$P_2^* = P_r - (P_r - P_2)/k \tag{26}$$

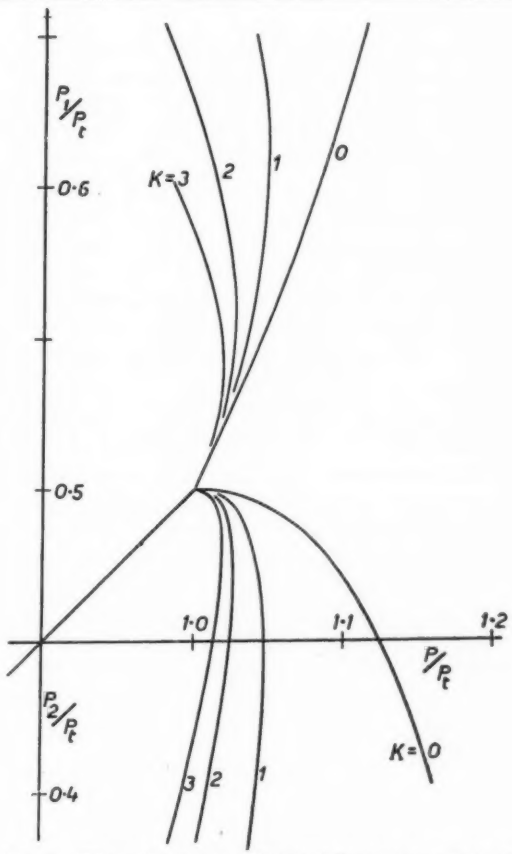

FIG. 5. Flange loads vs. applied load for various values of $K = -(\sigma/2E_t)(dE_t/d\sigma)$.

† In the load vs. column shortening graph, the lines corresponding to different initial buckling loads for $y_0 = 0$ do not cut each other; as in Fig. 4, the line starting at $P = P_t$ limits the region covered by equilibrium lines for imperfect columns.

Replacing these values in Eq. (25) yields a quadratic equation for P_2. In order to perform the calculations in an analytical way, considering $(P_x - P_1)$ as a small quantity, we may approximate the experimental relation by writing

$$P_1^* = P_1 + K[(P_1 - P_x)^2/P_x] \tag{27}$$

where

$$K = -(1/2)\ [(\sigma/E_t)\ (dE_t/d\sigma)] \tag{28}$$

the values in the brackets being calculated at point X.

According to Osgood's stress-strain law ($E\epsilon = \sigma + \text{constant}\cdot\sigma^n$), we obtain

$$K = [(k - 1)/2k]\ (n - 1) \tag{29}$$

Using the stress-strain law given in *R.A.S. Data Sheets 00.02* for an aluminum alloy having a yield stress of 55 ksi. and a ultimate stress of 73 ksi., at the stress for which $E_t = E/2$, we obtain the value $K = 2.80$.

Fig. 5 represents the values P_1 and P_2 as functions of the applied load computed for $k = 2$, $P_x = P_t$, and the values of K indicated near each curve.

Conclusions

The investigation of the symmetrical buckling of a column of constant, H-shaped section leads to a rather complex analytical problem, even when the curvature of the stress-strain diagram is neglected. The equation implied may be solved with the desired accuracy by a step-by-step procedure. The analysis shows that the buckling can start at any load between the tangent- and the reduced-modulus value. At the onset of buckling, the stresses in one of the flanges begin to decrease; the zone where this occurs (we call it "regression zone") covers a central portion of the strut (shadowed in Fig. 1a). The more the initial buckling load exceeds the tangent-modulus value, the wider the initial regression zone; its amplitude successively grows with increasing axial load and lateral deflections.

In the fundamental case, wherein the buckling starts at the tangent-modulus load, the regression zone proceeds from the mid-section of the column, spreading rapidly over a wide part of the strut. Analyzing for this case the variation of the flange loads in the mid-section, the results obtained by Shanley on the idealized semirigid strut appear qualitatively confirmed. The lateral deflections and the maximum stress in the mentioned region increase rapidly as the tangent-modulus load is exceeded.

Shanley's semirigid scheme was used to investigate the effect of initial eccentricities. In any case, the strain reversal occurs in one flange at a load less than the tangent-modulus value. The increase of deflections, and, consequently, of the maximum stress, is anticipated by initial imperfections. If these are supposed to vanish, the behavior of the strut approaches the ideal case of the straight column beginning to buckle at the tangent-modulus load. Therefore, the possible buckling processes starting at higher loads, as indicated by both the rigorous and the simplified analysis, appear as actually not attainable, unless an artificial restraint prevents the unavoidable eccentricities from their natural growth.

Furthermore, the analysis indicates that Southwell's plot of lateral deflections shows the same asymptotic slope as if the critical load had the reduced-modulus value. The representation of the buckling process, in the form proposed by Lundquist for the elastic range, may yield a straight graph, parallel to the line that should be obtained if the column behaved elastically according to the reduced modulus. However, these diagrams do not have the same value here as in the elastic range, where they serve to detect the true critical load, avoiding the construction of extraordinarily accurate specimens. In the case under consideration, they can conceal the real character of the phenomenon, disguising the bifurcation of the equilibrium line that exists at the tangent-modulus load for the straight column.

Another aspect of the problem which can be easily investigated on the ideal semirigid column is the effect of the curvature of the stress-strain diagram. When this factor is taken into account, the load resisted by the strut does not permanently increase with lateral deflections, as the previous analysis indicated. Even in the case of vanishing initial eccentricities, the maximum load resisted by the column is markedly less than the reduced-modulus value. This maximum load is considerably affected by the combined influence of previous imperfections of the column and curvature of the stress-strain diagram and may not attain the tangent-modulus value.

References

[1] Shanley, F. R., *Inelastic Column Theory*, Journal of the Aeronautical Sciences, Vol. 14, No. 5, p. 261, May, 1947.

[2] Wang, Chi-Teh, *Inelastic Column Theories and an Analysis of Experimental Observations*, Journal of the Aeronautical Sciences, Vol. 15, p. 283, May, 1948.

[3] Lundquist, E. E., *Generalized Analysis of Experimental Observations in Problems of Elastic Stability*, N.A.C.A. T.N. No. 658, 1938.

Hydrodynamic Longitudinal Stability

GEORGE S. SCHAIRER*
Boeing Airplane Company

Abstract

The various forms of hydrodynamic instability of flying boats are described, and the physical phenomena associated with these instabilities are examined. It is shown that there is a discontinuity in flow characteristics when the chine at the main step becomes submerged, which changes the wetted area from a triangle to a trapezoid. In cases where the afterbody or tail extensions are not in the water, this point of changing flow defines the lower porpoising limit. The lower limit is also partially determined by the point at which the afterbody first contacts the water. A form of upper limit porpoising which differs from skipping and closely resembles lower limiting porpoising is described. It is pointed out that hydrostabilizers† can materially change lower-limit porpoising.

Introduction

The longitudinal stability characteristics of seaplanes while riding on the water have been the subject of much study in recent years. This has come about because of numerous cases of oscillatory instability during take-off and landing in recent seaplanes. For many reasons these instabilities have become more important in recent seaplanes. As in the case of free-flight stability, a theory of oscillatory stability has existed for many years. Also similarly, this theory has been of little, if any, help in understanding and correcting the faults in seaplanes. In nearly all cases these faults have been corrected, if at all, by a cut-and-try method without any fundamental understanding of what was going on. To a partial extent such fundamental understanding now exists for certain types of hydrodynamic instabilities. Certain facts concerning the physical phenomena of instability are presented in this paper in the hope that those working on the theory of stability may be able to better match theory to practice.

Regions of Flow

The physical flows of water around a seaplane hull during take-off or landing cover a wide range of conditions. When at rest and at low speeds, the hull behaves very like a displacement boat, and virtually all lift is derived from displacement. In this régime resistance is mostly surface friction and wave drag. Aerodynamic forces on the seaplane are normally negligible except for propeller thrust. Longitudinal oscillations are usually highly damped under these conditions. At the opposite end of the speed scale near flying speed, entirely different conditions exist. In this régime displacement effects tend to be negligible, and lift is obtained from the planing action of the hull and aerodynamic lift on the wing. Resistance stems partially from surface friction and partially from a wave drag analogous to induced drag. Nearly all forms of hydrodynamic instability occur in this régime of planing flow. In the transition region between the displacement régime and the planing régime mixed flows exist. Apparently, all cases of instability existing in this régime are identical to, or closely associated with, those in the planing régime.

Stability Limits

It has been found that the angle of trim of the seaplane hull to the free water surface is of primary importance in describing stability limits. When operating at a given speed and weight, it will normally be found that within certain trim limits all longitudinal motions are damped and that within certain other limits longitudinal oscillations continue at finite magnitudes. The angle limits that divide these regions are sharp and definable in most experimental cases. In general, it has been found that the only effect of center of gravity is to change the trim angles that are obtainable because of control limitations. Center of gravity appears to have no effect upon the angle limits for stability. For this reason, it is convenient to use a trim angle versus speed plot to describe stability limits. Such a plot is shown in Fig. 1. On this plot are shown not only the trim limits for stability but also the free-to-trim angles for several elevator positions at one center-of-gravity location.

Types of Longitudinal Instability

The first type of longitudinal instability to attract much attention was a low-angle type of instability. In this type of instability, if the trim is reduced below certain values, a combination pitching and heaving oscillation starts. The motion is approximately sinusoidal with the two motions out of phase with each other and with a period of several seconds. This motion is commonly described as "porpoising." The magnitude of the motion may be small or large depending upon the extent to which the seaplane is trimmed into the unstable region of trims and upon the configuration of the hull. At low speeds the stability limit occurs at a high

Received November 18, 1949.

* Staff Engineer, Aerodynamics and Power Plant.

† The hydrostabilizer is a lateral stability sponson attached on either side of the hull at the main step, as in Boeing 314 and Martin 130 seaplanes.

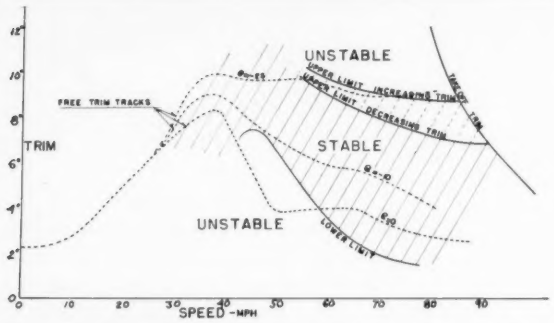

FIG. 1. Trim limits for stability of a typical flying boat.

trim angle, and at high speeds the trim limit is small. The stability limits for this type of instability for a conventional seaplane are shown in Fig. 1. In this type of motion the hull will practically never leave the water, and the motion will stop shortly after the trim has been shifted into the stable region.

A high-angle type of instability, commonly described as "skipping," has come into prominence in the last few years. In this type of instability the seaplane will commonly attempt to land at a fairly high angle, but immediately following contact with the water the angle of attack will increase and the craft becomes air-borne again. This cycle is repeated until the seaplane has lost flying speed or until flight is resumed. The action appears similar to the skipping of a stone on water. The same phenomenon may be experienced during take-off if the trim angle is increased into the skipping range. In this case the angle of attack increases suddenly, and the seaplane leaves the water. This maneuver is usually followed by a short pull-up, and the craft seldom contacts the water again. Skipping invariably involves leaving the water entirely, and, although the motion is repeated several times in some landings, it cannot be analyzed by any linear theory nor is the motion sinusoidal.

Trim limits for skipping are hard to measure full scale but are readily determined in constant-speed model tests. Two limits normally exist. There is a limit above which the trim must be raised to start the skipping, and there is a somewhat lower limit below which the trim must be reduced to stop the skipping. Typical limits are shown in Fig. 1. The severity of the motion at angles in the unstable region differs widely between hulls and is of more interest than the limits themselves.

There is another type of high-angle instability. This motion is similar to low-angle porpoising and has a single upper limit as compared with the double upper limit of skipping. The hull does not leave the water, and the motion appears to be nearly sinusoidal. The appearance of this instability to the pilot is essentially identical to the low-angle type, except that the angle must be reduced to stop the motion.

HYDRODYNAMIC STABILITY

A theory to account for hydrodynamic stability was given by Glauert in *R. & M. 1493* in 1932. This theory is similar in basis to most theories of stability for complex systems and involves certain assumptions and limitations that are usually considered admissible. These assumptions include: that the motion is small, that linear coefficients can be used, that no discontinuities exist, and that terms of order other than the first may be neglected. The Glauert theory has been difficult to apply and has seldom given results that agree with experiment. So far as is known, the Glauert theory has never been used to assist in understanding instabilities or correcting them. It is important that the Glauert theory be expanded into a useful and correct form or that a new theory be developed which adequately explains the physical phenomena. The absence of a proper understanding of these stability problems has prevented the correction of serious faults in many seaplanes.

INVESTIGATION OF WATER FLOWS

In order to determine the overall action of a seaplane, a detailed investigation of the water flows is necessary. Nearly all porpoising occurs in the planing region where the afterbody and tail extension are free of the water and only the straight portions of the main planing surface and the afterbottom need be studied. Nearly all hulls consist of Vee bottoms with flat surfaces except for a small amount of chine flare. To a first approximation the wetted area in the planing régime will be the area of the bottom which would be wetted if the heave and trim were held fixed and the velocity reduced to zero—that is, the water is deflected but little before contacting the planing surface. Using this approximation, it can readily be seen how the wetted area varies with heave or displacement. A typical wetted area sketch is shown in Fig. 2. With flat surfaces, the area is triangular up to the point where the chine at the step is wetted. For greater displacements the areas are double trapezoids. The wetted area increases as the square of the heave until the chine is wetted and linearly

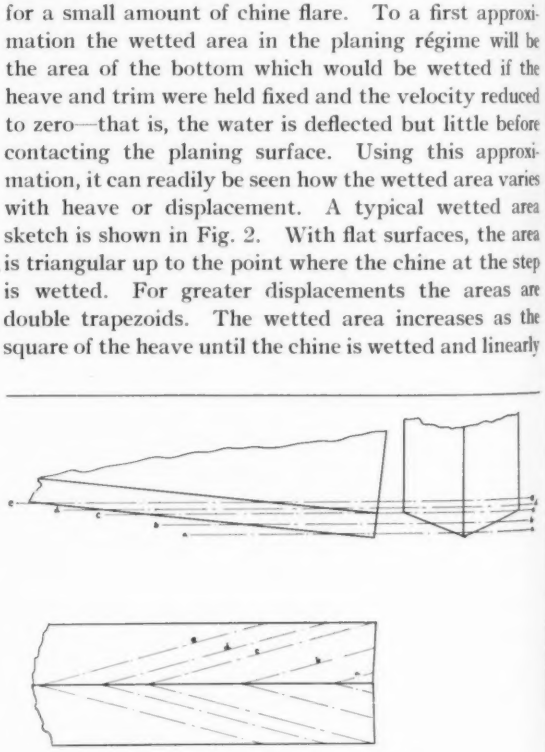

FIG. 2. Wetted area vs. heave.

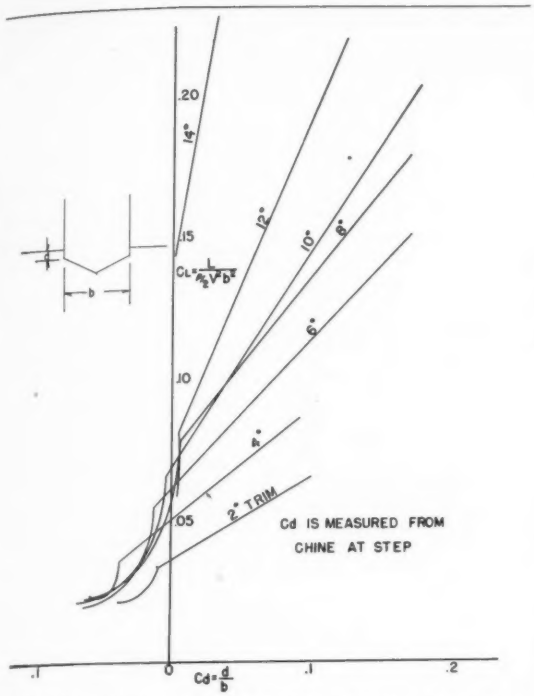

FIG. 3. Hydrodynamic lift coefficient as a function of trim and displacement. $C_v = 0.696$.

from then on. The lift should be nearly proportional to wetted area. Also, the motion of the center of lift should bear some relation to the motion of the center of wetted area. A typical set of lift data is shown in Fig. 3. These data are for a Vee planing surface with chine flare as used in a conventional hull. These data show a definite change in the curves at a value of heave nearly identical to that for chine wetting when at rest. The data also show a parabolic shape followed by a linear shape and have been plotted in coefficient form, with the coefficients based on dynamic considerations rather than the conventional displacement coefficients. These data are not greatly affected by Froude Number or displacement effects in the regions where instabilities occur.

In the case of a hull planing upon its forebottom, if the trim is increased sufficiently, the afterbottom will contact the water. As the trim is increased, still further considerable lift will be carried upon the afterbody. This contacting of the afterbody will produce a marked change in the moment characteristics and some change in the lift. The flow in the wake of the main step is complicated, and the water surface may be either above or below the undisturbed water surface and the angle may be inclined to the horizontal. Thus, it is difficult to predict either the trim angle at which the afterbody will contact or the forces following contact. Since the water surface will normally be curved, the forces may depend more on the curvature than upon the angle, and discontinuities may result from so-called "sticking flow," as over a spoon when held with the convex side under a water faucet.

STABILITY THEORY

An examination of the basic flows as given above is necessary before the application of planing surface data to the stability theory. The examination above shows a number of different flows over the hull. The stability theory must be applied separately to each region of flow and must not be applied at all in the immediate vicinity of the changes between types of flow. The application of the linear theory in the region where the lift varies as the square of the displacement will be difficult at best and not necessarily possible. The next consideration is to determine in what flow regions instabilities actually exist on seaplanes. These regions are sharply defined for normal hulls and can be plotted on the trim versus speed plot. If the aerodynamic lift is assumed constant with angle, the hull will operate at a given weight and speed at constant lift coefficient. For a constant water lift coefficient, the variation of trim with displacement can be determined from Fig. 3 and plotted as in Fig. 4. The chine is wetted at low angles and free at high angles. A typical afterbody has been shown in Fig. 4 but was not considered in the lift calculations. At some trim angle the sternpost will touch.

The regions of flow are plotted on a speed versus trim plot in Fig. 5. Not only is the lower envelope of these curves similar in shape to the lower limit but, for several cases, it is identical to the lower limit.

This is a most important fact. For several cases, it shows that stability was not dependent upon some fine gradation of damping but was determined by

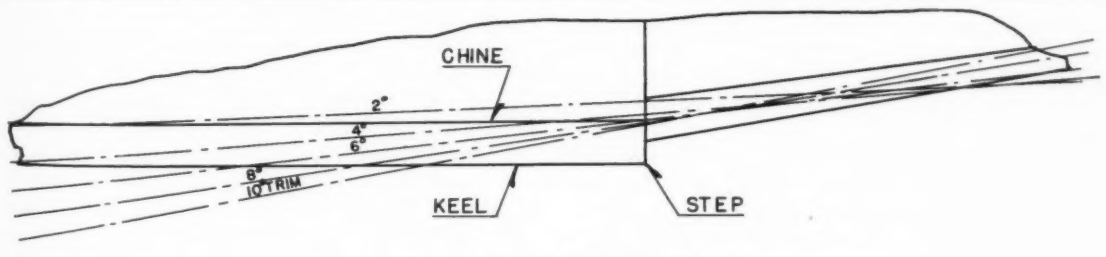

FIG. 4. Water lines for equal lift.

changing physical phenomena. It has frequently been observed that wetting of the sternpost is never present in lower-limit porpoising, but the chine limit is believed to be a new discovery. Model tests of the XPBB1 confirm the coincidence of the lower limit with both the force break in the lift curves and the point of visual wetting of either the sternpost or chine. In the full-scale tests it was not possible to observe the sternpost wetting, but in the speed region where the sternpost was probably free the lower limit was identical to the point at which the chine was wet. If the chine were visually wet more than $^1/_2$ in. forward of the step, a definitely perceptible heaving oscillation could be felt. This was checked at a number of speeds.

Additional tests were run on the model at various weights and without the wing, and in all cases the lower limit was defined as described above.

Extensive dynamic stability tests were run on a model of the Boeing 314 which had hydrostabilizers. The full-scale tests had never indicated the existence of a lower limit to stability. The model tests showed that a mild type of lower-limit porpoising was possible in certain limited regions of speed and trim. These are shown in Fig. 6. When the hydrostabilizers were removed from the model, conventional lower limits were obtained as shown in Fig. 6. The lower-limit porpoising was violent in this case. It is obvious that the hydrostabilizers have a major effect on the lower limit. Here again, the physical flows were investigated, and it was found that there was no instability when the hydrostabilizers were contacting the water. Below certain trim angles, the hydrostabilizers planed on the water with a triangular wetted area. Since the step of the hydrostabilizers intersected the hull proper slightly above the chine, it was possible to wet the chine without wetting the hydrostabilizers in certain regions, and it was only in these regions that instability could be found. Since the angle limits for this instability were narrow, only a small oscillation could exist without exceeding the limits and a mild motion resulted.

It might be presumed that a complete explanation of lower-limit porpoising has been found. This is certainly not the case. Lower-limit porpoising is essentially a coupled oscillation of a system with at least two degrees of freedom. Without going into the mathematics of the cases, it would appear that for certain combinations of physical phenomena stability normally exists and that for certain other combinations instability normally exists. Nothing has been presented herewith to prove that an unstable case might not be found under physical conditions normally giving stability or vice versa. Damping of sufficient magnitude and properly applied should make any case stable. Possibly, such damping can be supplied by an aerodynamic tail surface. In any case, data conflicting with the above findings may exist.

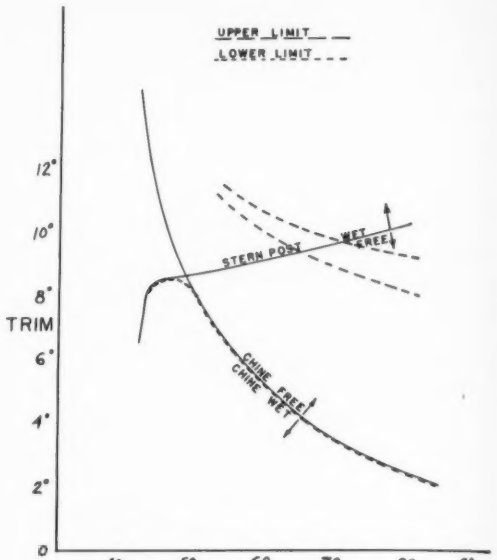

FIG. 5. Trim vs. speed.

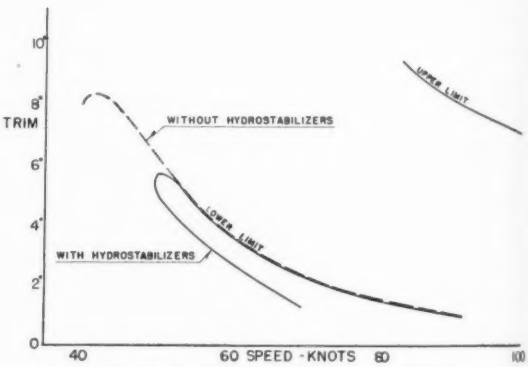

FIG. 6. Trim limits for stability of Boeing 314.

DISCUSSION

In examining data it is important to know the basis of the data. Some investigators use a finite amplitude of oscillation (such as a double amplitude of 3°) as the definition of the limit of stability, and such data will not agree with the data of this paper wherein the limits are for no perceptible oscillation. Much broader limits will be obtained if a finite oscillation is used as the basis of stability limits.

It is not difficult to find common hull types to which the physical limits described above cannot be applied. A hull with a long, pointed, main step without any break between the step and the chines is such a case. This is exactly the form of surface used for the afterbody of most recent flying boats. The characteristics of such a surface will vary widely and for certain conditions may be stable and for certain other conditions may be unstable. It will probably be difficult to find any physical

phenomena in connection with the flow over such surfaces which will tie in with the stability limits. Other hull forms not covered include fluted bottoms, flat bottoms, Vee steps, sea sleds, and all forms of hull differing much from those investigated.

Most investigators have attempted to check theory against practice in the flow region where the hull characteristics most nearly approximate those of a flat planing surface. This is, of necessity, the region where the afterbody is free and the chines are wet. It is not surprising that instability was indicated for most cases. The fact that the hull may operate under widely different conditions has usually been neglected. It is these different conditions that supply the stable regions for most seaplanes.

For conventional hulls, it would appear that the seaplane designer has no control over the lower stability limits. The sternpost angle is the only important variable. The designer has considerable latitude in the application of the hull in order to provide that the seaplane will normally be operated within its stable region. This control is exerted mostly by properly locating the center of gravity, but it is also influenced to some extent by the overall configuration of the seaplane and to some extent by its loading. Highly loaded hulls are much more susceptible to trouble than lightly loaded hulls. It has been found that, if the speed scale is divided by the square root of the hydrodynamic lift, the trim limits are nearly independent of the weight. Thus, increasing the weight moves the trim limits out to higher speeds. In some cases this can be serious. Since take-off and landing are accelerated conditions, the time spent in any given region will be short. If the instability is not great, it is perfectly feasible to accelerate through an unstable region without ever encountering an oscillation. However, at high weights the accelerations are reduced, and sufficient time may be spent in a condition to realize fully the instability characteristics of the region. Unstable regions should be avoided if at all possible.

Skipping has not yielded to any simple physical reasoning. The hull-water combination is analogous to the landing gear-tire-oleo combination of a landplane. If a seaplane lands with a vertical velocity, the hull displacement will exceed the statically required displacement, and an upward velocity will be imparted to the hull. This is similar to a spring effect. Of course, there will be some energy absorption as by an oleo, but the hull may leave the water and make a second contact. This can all occur without the trim angle changing appreciably. The result is a simple bouncing. If the total water reaction results in an increase in trim angle, both the hydrodynamic and aerodynamic lift will increase, and the vertical velocity leaving the water can be higher than that when entering. Such a condition is similar to that occurring on an airplane with the main wheels ahead of the center of gravity, except that it may be more severe. On the Boeing 314 in its original configuration, a high-angle landing would put the afterbody and a portion of the main bottom in the water. Although all of this area was behind the center of gravity, the resultant forces on the seaplane resulted in an increase in trim, and the ship usually left the water immediately. A number of structural failures occurred on this and other seaplanes in which the afterbottom structure failed downward. Apparently, the increase in trim results from downward forces upon at least a portion of the afterbottom. On the Boeing 314, it was found, by the cut-and-try method, that after deepening the step this tendency to increase trim was sufficiently reduced to prevent leaving the water on most landings. Some semblance of the phenomena remained in the scale model after changing the step, and the angles at which it occurred were essentially unchanged but the magnitude of the motion was greatly reduced.

Sudden trim increases during take-off resulting in unintentional take-offs also occurred in the Boeing 314. These were analogous to the skipping on landing but proved that the difficulty was not primarily associated with the vertical velocity on landing and was more a function of the hydrodynamic moments than anything else. Apparently, the moments are discontinuous with trim angle. This may not be a static moment condition but does appear to be related to the effect of aerodynamic ventilation upon the hydrodynamic flow over the afterbottom. Deep steps and ventilation nearly always reduce the severity of skipping but have little effect upon the trim limits for stability. In the case of the Boeing 314, the step depth was increased by moving the step aft, and all skipping was eliminated in the full-scale case both during take-off and landing. Such a change would not have been possible in a normal seaplane, but in this particular case there was no lower-limit porpoising, and the trim change resulting from moving the step had unimportant effects. Without the hydrostabilizers this seaplane would have trimmed in the lower-limit porpoising range both before and after the step change. In the case of the XPBB1, the hull was initially designed with an extremely deep step, and no evidence of skipping was ever seen in the full-scale article. Double upper limits of skipping could be found in the model, but the motion was mild. The deceleration during a landing is sufficiently great to prevent mild motions from becoming evident to the pilot. So far as is known to the author, the XPBB1 never left the water after its first contact in landing. In landings with high vertical velocities, the ship would initially sink noticeably below the static displacement and would then rise nearly clear of the water, followed by a normal slowing down in the water.

In the XPBB1 definite evidence was found at full scale of an upper-limit instability that closely resembled lower-limit porpoising and which had none of the characteristics of skipping. The motion was mild and had a single upper limit as distinguished from the double upper limit of skipping. There was no tendency to leave the water, and the condition could be found from

hump speed to near take-off speed. There is no assurance that this instability was encountered on the model, possibly because the model did not aerodynamically resemble the full-scale article at the extremely high angles at which this motion was encountered. During this motion, the afterbottom was wet to a great extent, and the main step was wet with a triangular area. It occurs to the author that this instability may result from the same combination of events applied to the afterbody which causes lower-limit porpoising when applied to the forebody alone.

Conclusion

It is the hope of the author that the material of this paper will stimulate further investigations toward the end that the longitudinal hydrodynamic stability problems will become well understood. It appears necessary to make the theory agree with the physically observable facts if success is to be had. In the case of lower-limit porpoising, there appears to be excellent agreement between the regions of stabilities and the regions of certain basic flow types. Skipping and a new type of upper-limit porpoising have been described.

Since preparation of this paper, a paper "Some Aspects of the Flow Round Planing Seaplane Hull or Floats and Improvement in Step and Afterbody Design," by K. M. Tomaszewski and A. G. Smith was given at the VII International Congress of Applied Mechanics. The latter contains information concerning upper-limit porpoising which complements the information on lower-limit porpoising given above.

Torsion of Thin-Walled Closed Cylinders Beyond the Elastic Limit

(*Continued from page 507*)

[3] Kuhn, Paul, *Some Elementary Principles of Shell Stress Analysis with Notes on the Use of the Shear Center*, N.A.C.A. T.N. No. 691, March, 1939.

[4] von Kármán, Th., and Christensen, N. B., *Methods of Analysis for Torsion with Variable Twist*, Journal of the Aeronautical Sciences, Vol. 11, p. 110, 1944.

[5] Bredt, R., V. D. I., Vol. 40, p. 815, 1896.

[6] McConnell, A. J., *Applications of the Absolute Differential Calculus*, p. 308; Blackie and Son Ltd., London and Glasgow, 1931.

[7] von Kármán, Th., and Christensen, N. B., loc. cit., p. 112.

[8] Kuhn, Paul, loc. cit., p. 33.

I.A.S. Nineteenth Annual Meeting

Authors wishing to have papers considered for presentation at this meeting should submit outlines or short abstracts to the Meetings Committee, 2 East 64th St., New York 21, N.Y., no later than September 15, 1950.

A Mechanical Analogy for Hypersonic Flow

H. REESE IVEY*

Langley Aeronautical Laboratory, N.A.C.A.

SUMMARY

A mechanical analogy for hypersonic flow is described which may be useful for the Mach Number range of 5 to infinity.

The basic characteristics of the various flow types are reviewed: gas dynamics, slip flow, and free molecule flow. From that discussion the requirements are determined for an analogy to simulate hypersonic flows. The theory of the analogy is developed, and a simple apparatus is described for demonstrating it. The functions of the various parts of the device are explained, and typical photographs of the resulting flow are presented. The pictures show the gradual degeneration of shock waves as the effective operating altitude is increased from the gas dynamics region to the free molecule region. Possible uses of the analogy are suggested, and the operating limitations are discussed.

INTRODUCTION

SOME OF THE FEATURES that characterize modern aerodynamics may be conveniently illustrated by considering missiles. For example, missiles designed for operating at high supersonic speeds present several complex aerodynamic problems related to the large changes in atmospheric density encountered along the flight paths. At the lower altitudes the mean free paths of the molecules are short, and the air can be considered as a continuous medium. In this case the laws of gas dynamics apply: strong, sharply defined shock waves occur and fully developed boundary layers are formed.

As the missile rises into the upper atmosphere, the mean free paths of the molecules become appreciable but are still small by comparison with the characteristic missile dimension. Since shock waves are at least one mean-free-path length thick, the shock waves on the missile are no longer sharply defined but are noticeably thick and diffuse. Similarly, the boundary layers begin to behave differently from the boundary layers of continuous fluids. For example, a molecule can carry momentum from a relatively high speed level of the boundary layer to the surface of the missile without always hitting intermediate molecules or losing momentum to them. Thus, the flow velocity at the missile surface is no longer zero, as is the case for continuous fluids, but is higher, being determined from statistical considerations of the velocities of the molecules hitting the surface. Since the velocity at the surface is not zero, the flow can be said to "slip," and the missile is operating in the "slip-flow" region of flight. At a still higher altitude, the molecular mean free path becomes large with respect to the missile dimensions. There, the molecules in the free stream can hit the missile surface at full speed and are re-emitted without direct interference from other molecules. Shock waves and boundary layers are no longer recognizable as such in this free molecule flow.

Relatively little information is available concerning the transition of the flow from one type to another as the flow density is varied while the Mach Number is kept constant at some high supersonic value. Therefore, it seems desirable to develop an apparatus that can provide visual information that may give a better understanding of the phenomena and can give qualitative force measurements. The preceding discussion suggests that the flow in such an apparatus must behave as though it consists of finite particles or molecules rather than acting as a continuous medium. The present paper presents a mechanical analogy for hypersonic flows which uses hard elastic pellets to represent the molecules of a real gas.

BASIS FOR THE MECHANICAL ANALOGY

The Mach Number M of a flow is usually defined as the ratio of the directed macroscopic speed V of the flow to the speed of sound a

$$M = V/a \tag{1}$$

From the kinetic theory of gases, with the usual limitations of equipartition of energy and perfect elasticity, the speed of sound is determined by the number of excited degrees of freedom n of the gas molecules and the root-mean-square random speed v_{rms} of the molecules—that is,

$$a = [(n + 2)/3n]^{1/2} v_{rms} \tag{2}$$

Combining Eqs. (1) and (2) yields

$$M = (V/v_{rms})[3n/(n + 2)]^{1/2} \tag{3}$$

Eq. (3) serves as the basis for a hypersonic flow analogy. For a given type of ideal molecule, the Mach Number of the flow is determined by the ratio of the free-stream speed to the root-mean-square random speed of the molecules.

In addition to securing the proper Mach Number, one must obtain the desired mean free path of the molecules in order to have the right type of flow. The mean free path L is a function of the effective diameter d and the number of molecules N in a unit volume

$$L = 0.2251/Nd^2 \tag{4}$$

Eq. (4) shows that a few large molecules can give the

Presented at the Aerodynamics Session, Eighteenth Annual Meeting, I.A.S., New York, January 23–26, 1950.

* Aeronautical Research Scientist, Theoretical Aerodynamics Division.

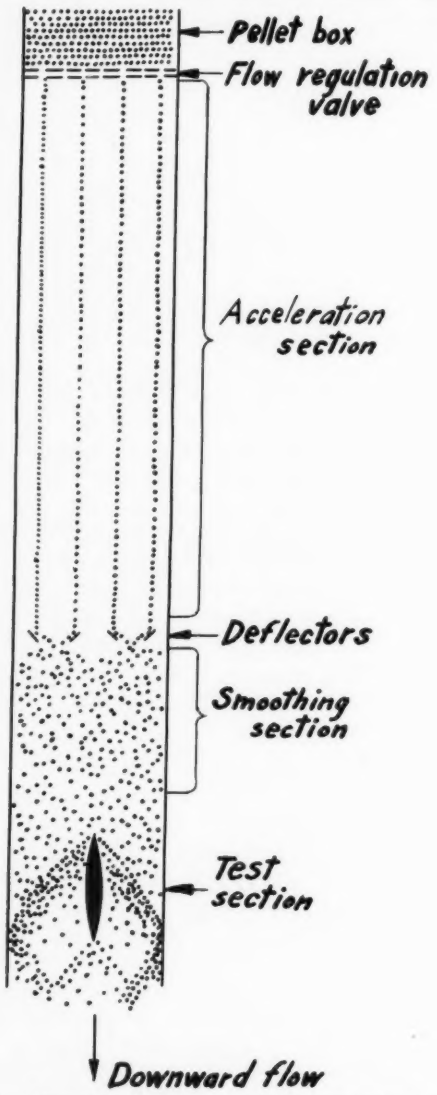

FIG. 1. Schematic diagram of simple mechanical analogy apparatus.

same mean free path as many small molecules. As long as the mean free path is large compared with the particle size, the molecules of a real gas can be represented by relatively few small elastic spheres in order to form a mechanical analogy of the real flow. The effective Mach Number [Eq. (3)] is determined by the ratio of the directed speed of a stream of pellets to their random speed.

The Reynolds Number of the flow is proportional to the ratio of the Mach Number and mean free path for given dimensions and gas properties.

A Simple Mechanical Analogy Apparatus

In a simple piece of equipment for demonstrating the mechanical analogy, the elastic pellets are simply dropped onto deflectors and then onto a model to be tested (Fig. 1).

The various parts of the apparatus and their functions are as follows:

(A) Pellet storage box stores the pellets and supplies them in a steady stream.

(B) The flow regulation valve distributes and regulates the mass flow.

(C) The acceleration section gives directed motion to the stream of pellets by allowing them to fall.

(D) The deflectors give small disturbance velocities to the pellets.

(E) The smoothing section furnishes the pellets with a space in which the disturbed pellets can collide with each other and develop a random disturbance velocity superimposed on the general stream velocity.

(F) The model is placed at the lower end of the smoothing section so that the pellets will stream over and around it.

Gravity can be used to furnish the required particle speeds, but in that case the length of the acceleration section must be long when compared with the length of the model in order to approximate unaccelerated flow.

The flow density at constant Mach Number may be varied by means of a flow-regulation valve. At high flow densities, the flow corresponds to the gas dynamics type of flow, and regular shock waves are formed as evidenced by a sharp demarcation between high-density and low-density regions of the flow. At lower flow densities slip flow occurs, and at sufficiently low densities the flow corresponds to free molecule flow. With free molecule flow, the pellets that hit the model bounce off and leave the vicinity of the model without running into other pellets. In this case no phenomenon that can be identified as a shock wave occurs, and only a gradual increase in density exists near the front portion of the model. Weak disturbances from the model are visible considerably ahead of the position a shock wave would have if the flow were sufficiently dense.

One parameter that is of some importance in simulating a supersonic flow is the ratio of the specific heats of the gas γ. If the energy is equally divided among the various degrees of freedom of the molecules, then kinetic theory gives the ratio of specific heats simply as a function of the number of degrees of freedom

$$\gamma = (n + 2)/n \tag{5}$$

Air molecules at room temperature possess many of the features of rigid dumbbell molecules, which have three translational degrees of freedom and two rotational degrees. Then, for air,

$$\gamma = 7/5 = 1.4$$

In order for a hypersonic analogy to give the proper shock-wave angles, the effective value of γ should be close to 1.4. If spherical pellets are used in the analogy to represent molecules, the value of γ analogous to the

ratio of specific heats in a real gas is found from Eq. (5). A spherical pellet has three translational and three rotational degrees of freedom; however, the rotational degrees may not be fully excited. Thus, one might expect a flow of spherical pellets to behave somewhat like a gas with fewer than six degrees of freedom. The values of γ for a real gas having three and six degrees of molecular freedom, respectively, are

$$\gamma_3 = \frac{n+2}{n} = \frac{5}{3} = 1.67; \quad \gamma_6 = \frac{8}{6} = 1.33$$

From these considerations, a flow of spherical pellets should behave somewhat like a gas having a value of γ between 1.33 and 1.67. In a real gas having nearly spherical effective boundaries for the molecules (for example N_2), the excitation of molecular rotations may take ten collisions, whereas only one or two are required for approaching translational equilibrium. The ratio of specific heats is discussed in more detail subsequently in the present paper.

When the lower density flows are being considered, the proper type of molecular reflections from the model surface must be secured. When an air molecule hits a surface, it seems to stick momentarily and then leave again in some random direction that is not related to its original direction of motion. In order to simulate such diffuse reflections with the mechanical analogy, the model surface must be machined with a particular type of surface roughness designed to make the pellets bounce in random directions with a Maxwell distribution of speeds. The surface pressures are not critically affected by slight deviations from the desired velocity distribution.

The pressure exerted on a surface by a low-density airflow depends on the momentum change of the molecules hitting the surface. The momentum change depends partly on the velocity with which molecules are re-emitted from the surface. For a translational accommodation coefficient of 1, the average velocity of emission is proportional to the square root of the surface temperature. If the surface temperature is less than the stagnation temperature (as is the usual case for hypersonic missiles at high altitudes), the molecules lose part of their energy to the surface. It thus becomes apparent that an inelastic surface in the mechanical analogy is analogous to a cold surface in air. Similarly, a perfectly elastic surface in the analogy corresponds to a surface at stagnation temperature. A vibrating rough surface may have to be used in the analogy to simulate a surface hotter than stagnation temperature by increasing the energy of the particles that hit the surface.

The Mach Number of the flow can be altered by changing the angle of the deflectors that are responsible for the random motion of the pellets. This change essentially corresponds to securing a different speed of sound in the real gas. Possibly the simplest and most interesting case is that in which no deflectors are installed. The speed of sound is then effectively zero in the corresponding real gas and the Mach Number infinite.

Typical Visual Results

Interesting optical studies of the flow can be made with ordinary photographic equipment. In order to secure information on the instantaneous distribution of pellets, short exposure times are used. A series of similar pictures taken with a high-speed motion-picture camera is sufficient to determine the paths and speeds of the pellets. Time exposures are useful in giving smooth flow patterns.

Fig. 2 is a typical picture of the flow around a wedge airfoil at a Mach Number estimated from high-speed motion pictures of the flow to be about 10. The white region represents high-density flow, and the dark region represents low-density flow. The flow rate in the apparatus is such that the mean free path of the flow is small compared with the model dimensions but is not negligible. This flow rate is analogous to slip flow in a real gas. Note that the shock wave represented by the leading edge of the white flow region is diffuse; this diffuseness indicates that the mean free path of the pellets is appreciable. In fact the mean free path of the particles is so large in the dark region of the flow that no trailing edge shock wave is noticeable. The blunt edge of the test airfoil causes the shock wave to be slightly detached from the nose. For this particular picture, the ratio of specific heats for the corresponding real flow was approximately 1, as is explained later in the paper, and, hence, the flow separates from the airfoil at the midchord of the lower surface as predicted by the author.[1]

Fig. 3 shows the same airfoil as Fig. 2, except that the flow density is lower. The shock wave is becoming

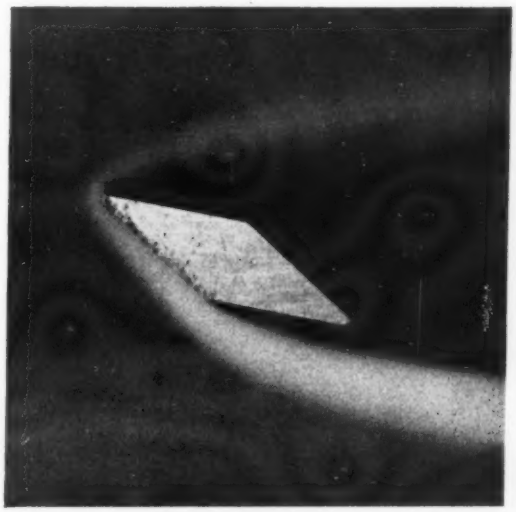

FIG. 2. Hypersonic flow around wedge airfoil in slip flow.

FIG. 3. Hypersonic flow around wedge airfoil in low-density slip flow.

FIG. 4. Hypersonic flow around wedge airfoil in free molecule flow.

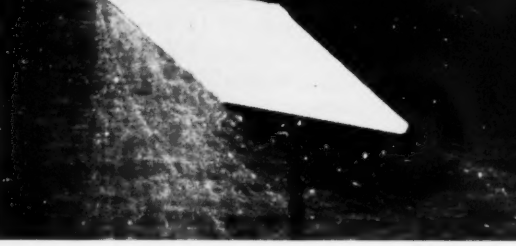

FIG. 5. Hypersonic flow around circular cylinder in slip flow.

more diffuse and the high-density region is increasing in extent.

Fig. 4 shows the airfoil in a still lower density flow. This time the mean free path is so long that the leading shock wave has broken down and the molecules are reflecting from the surface in quasi-specular fashion (free molecule flow with the ratio of specific heats approximately 1.33). The influence of the airfoil can be seen well ahead of the usual gas dynamics shock-wave location.

Fig. 5 shows the flow around a circular cylinder when the mean free path is in the slip-flow region with the ratio of specific heats in the corresponding real gas equal to approximately 1.0. Again the diffuse shock wave can be seen. This type of picture should serve as a partial check on the hypersonic method of reference 1, which used the assumption of $\gamma = 1$ because of resulting simplifications.

Fig. 6 pictures the flow around the cylinder of Fig. 5 at a lower density. The density increase in front of the cylinder has become gradual, and the density increase begins ahead of the gas dynamics shock-wave location.

Determination of Operating Conditions

The determination of the operating conditions in an analogy apparatus rests primarily on the development of instrumentation, but a possible approach to the problem can be discussed briefly.

When w is the weight of pellets in the pellet storage box b and t is the time, the weight flow rate dw/dt in the tunnel can be found from the rate of change of weight of pellets (dw/dt) in the pellet storage box and can be written as

$$dw/dt = -(dw/dt)_b \tag{6}$$

The directed stream velocity V in the test section is found from the acceleration of gravity g, the height h

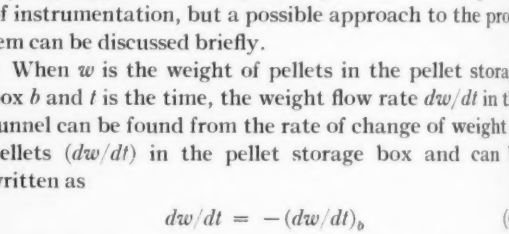

FIG. 6. Hypersonic flow around circular cylinder in low-density slip flow.

that the pellets fall from the flow regulation valve to the deflectors, and the distance h from the valve to the test section. This velocity must be corrected for the drag force D on the deflectors. Air resistance is eliminated by operating in a vacuum. The approximate directed speed is

$$V = \sqrt{2gh}\left[1 - \frac{1}{h}\sqrt{2gh_1}\left(\frac{D}{dw/dt}\right) + \frac{g}{2h}\left(\frac{D}{dw/dt}\right)^2\right]^{1/2} \tag{7}$$

The density ρ of the flow is found from the test-section cross section A, the velocity, and the mass flow.

$$\rho = (dw/dt)/AV g \tag{8}$$

The speed of sound a in the analogous real gas is found from the ratio of specific heats γ, the pressure p exerted on the test-section walls by the pellets in the corresponding real gas, and the density ρ. Thus, with all the assumptions previously made,

$$a = \sqrt{\gamma p/\rho} \tag{9}$$

Eqs. (1), (7), and (9) determine the Mach Number. Eqs. (7) and (8) serve as a basis for determining the dynamic pressure.

The mean free path of the pellets is important in determining the type of flow over the model: free molecule flow, slip flow, or gas dynamic flow. Since the mean free path is essentially determined by the cross section of particles in a given volume, numerous small pellets are better than a few large ones if the mean free path is to remain larger than the molecular diameter. In the present investigation, solid glass beads approximately 0.006 in. in diameter were found to be satisfactory and are readily obtainable.

The mean free path L of the pellets is a function of the number N in a unit volume and of their diameter d

$$L = 0.2251/Nd^2$$

Operating Limitations

The mechanical analogy apparatus possesses certain basic limitations that must be considered.

It has been pointed out that the spherical pellets have six degrees of freedom instead of the five degrees that cool air has. The three rotational degrees may not be fully excited. Hence, the equivalent ratio of specific heats γ is between 1.33 and 1.67 instead of 1.4. This analogous value of γ will give shock-wave angles and density ratios that are slightly in error and pressures that are approximately correct except at extremely high supersonic speeds.

Other values of γ can be simulated by means of special designs. Lower values of γ are attainable by using more complicated "molecules," and higher values are obtainable by eliminating some of the degrees of freedom. For example, if the apparatus is only one "molecule" wide, the spheres have only two translational degrees of freedom and one rotational degree (the rotation may not be fully excited). The simulated value of γ is then between 1.67 and 2.0.

Whereas air molecules essentially are perfectly elastic, the small pellets used in the mechanical analogy possess a definite internal damping that is related to the coefficient of restitution. This damping limits the number of collisions allowable in the flow. For low flow densities where free molecule flow exists, the damping is not important, but, as the flow density is increased until gas dynamic flow begins, the damping becomes important and sets the limit on the usable flow densities. If the flow density is high, the random motions will damp out as though the molecule represented by the pellet had an infinite number of degrees of freedom which shared equally in energy. The value of γ simulated by high-density flow in the mechanical analogy is then

$$\gamma = \lim_{n \to \infty} [(n + 2)/n] = 1$$

Thus, some control can be exercised over the value of γ represented by the flow of pellets; however, except for the case of $\gamma = 1$, the flow density must be kept low because of internal damping. If the Mach Number is known for simulated gas dynamic flow over a wedge, the effective value of γ can be determined by measuring the shock-wave angle and applying the classical shock-wave equations. In order to minimize the effective variation of γ with density, it is necessary to use elastic particles (glass beads were used in the present investigation) and a massive model (no thin skin) made either of an elastic material or a material that has a high modulus of elasticity.

The importance of γ in determining the pressures and shock-wave angle at supersonic speeds can be estimated from the following table for the flow over a 4° slope at a Mach Number of 7:

γ	Shock Angle	Pressure Coefficient	Ratio of Pressure Coefficients to That of Air
1.0	10° 29′	0.02555	0.953
1.4 (air)	11°	0.02682	1.0
1.667	11° 22′	0.02775	1.035

At higher speeds the per cent error is more for straight-sided shapes but is small for many curved shapes.

It is probably well to take into consideration the fact that solid pellets do not necessarily reflect specularly from smooth surfaces. For deflections at small angles of incidence the reflection angle may be less than the angle of incidence because the coefficient of restitution is less than 1. At high angles of incidence, the angle of reflection may be larger than the angle of incidence because of the drag exerted on the pellet by the surface friction which causes the pellet to rotate.

One of the most important problems in developing the mechanical analogy is the overcoming of the effects

of inelasticity of the pellets. One approach to the problem would be to add continually random energy to the flow by means of vibrating surfaces or by means of electrical or magnetic excitation of some kind. Another approach is to increase effectively the efficiency of the collisions; for example, possibly the mechanical collisions can be replaced by some more efficient electrical repulsion between pellets.

Possible Uses of the Mechanical Analogy

The successful application of the mechanical analogy requires a certain understanding of the basic behavior of air molecules under similar circumstances. For example, in order to secure true pictures or force data for an airfoil in free molecule flow, it is necessary to make the proper adjustments to the surface finish so that the pellets will undergo diffuse reflection. In effect, the mechanical analogy apparatus is a device for carrying out involved computations, provided it is given the proper basic functions with which to work.

One of the most important characteristics of the mechanical analogy is that the flow pattern, the density distribution, and even the paths of the individual "molecules" are readily apparent to the eye or to a camera. This flow visibility is vitally important in attaining a quick understanding of the mechanism of various phenomena.

The mechanical analogy may be useful in several fields of aerodynamics as a means of supplementing other equipment, particularly in preliminary work where the ease of changing the model, the Mach Number, and the flow density may be important. Probably the most accurate information will be obtained for either free molecule flow or slip flow, since the internal damping of the particles is not so large.

Concluding Remarks

A mechanical analogy has been described which is suitable for studying hypersonic flows at speeds from Mach Number 5 to infinity. Photographs have been presented which show the gradual flow evolution at high altitudes where discontinuous shock waves no longer occur. Possible uses and limitations of the apparatus have been discussed. The most serious limitation of the analogy is the inelasticity of the particles used to simulate air molecules. At the present stage of development the analogy can be used for visual studies of various flow phenomena and for qualitative force measurements.

Reference

[1] Ivey, H. Reese, Klunker, E. Bernard, and Bowen, Edward N., *A Method for Determining the Aerodynamic Characteristics of Two- and Three-Dimensional Shapes at Hypersonic Speeds*, N.A.C.A. T.N. No. 1613, July, 1948.

First U. S. National Congress of Applied Mechanics

Plans have now been formulated to hold the First U.S. National Congress of Applied Mechanics on June 11–16, 1951, at Chicago, Ill. The Illinois Institute of Technology will be host to the Congress.

Members of the Institute, one of the sponsoring societies, are cordially invited to submit papers, which should constitute original research in applied mechanics. (Their length must not exceed 5,000 words or the equivalent in equations, tables, and diagrams.) Abstracts must be submitted to the Chairman of the Editorial Committee before April 14, 1951; complete papers must be submitted prior to June 11, 1951.

Additional information about the Congress may be obtained by writing to N. M. Newmark, Secretary of the Congress, University of Illinois, Urbana, Ill. All members are invited to attend.

Readers' Forum

BRIEF REPORTS of investigations in the aeronautical sciences and discussions of papers published in the JOURNAL are presented in this special department. The publication will be completed approximately 8 weeks after receipt of the material. The Editorial Committee does not hold itself responsible for the opinions expressed by the correspondents. Contributions should not exceed 800 words in length.

On the Stability for a Certain Degenerate Type of Disturbance of Viscous Fluid Flow Between Parallel Walls

S. I. Pai

Institute for Fluid Dynamics and Applied Mathematics, University of Maryland, College Park, Md.

May 23, 1950

IN THE STUDY OF HYDRODYNAMICAL STABILITY of two-dimensional parallel flows, H. B. Squire made a great contribution by showing that three-dimensional wavy disturbances are more stable than two-dimensional ones.[1] It simplifies the mathematical analysis to a large extent. However, the analysis of a certain degenerate type of disturbance treated by Squire in reference 1 is incomplete. This note gives the complete analysis of the stability for this degenerate type of disturbance.

For convenience of comparison, we use the same notations as those used in reference 1.

We consider the steady two-dimensional flow of an incompressible viscous fluid upon which a disturbance is superimposed. The origin O is taken at a point midway between the walls, the axis of x is in the direction of the flow and parallel to the walls, the axis of y is perpendicular to the walls, and the axis of z is parallel to the walls and perpendicular to the other axes. If $2b$ is the distance between the walls, these will coincide with the plane $y = \pm b$. The main flow is defined by

$$u = U(y), \quad v = 0, \quad w = 0 \tag{1}$$

where u, v, w are the velocities in the direction Ox, Oy, Oz, respectively.

If now a small disturbance be superposed on the main flow, the velocities will be given by

$$u = U(y) + u_1, \quad v = v_1, \quad w = w_1 \tag{2}$$

where u_1, v_1, w_1, are small quantities whose squares may be neglected.

It will be assumed that any disturbance can be broken up into a set of disturbances which is periodic with respect to x and to z. Thus we may take

$$\left.\begin{aligned} u_1 &= u(y) \exp i(jx + kz - \sigma t) \\ v_1 &= v(y) \exp i(jx + kz - \sigma t) \\ w_1 &= w(y) \exp i(jx + kz - \sigma t) \end{aligned}\right\} \tag{3}$$

where j and k are real and positive and σ is in general complex.

For the degenerate type of disturbance $v(y) = 0$, the equation of motion for the disturbance in nondimensional form will be

$$\Delta(u) = [D^2 - (\alpha^2 + \beta^2) - iR\alpha(V - c)]u = 0 \tag{4}$$

with the boundary conditions of u.

$$u = 0 \quad \text{for} \quad y = \pm 1 \tag{5}$$

where

$D = d/dy$
$\alpha = jb$
$\beta = kb$
$V = U/U_0$
$cU_0 = \sigma/j$
$y = y/b$
$R = U_0 b/\nu$ = Reynolds Number
U_0 = some reference velocity

Squire has shown that if c is real, no real value of $R\alpha$ can be found which satisfies Eqs. (4) and (5). This only means that, for finite Reynolds Number R, there is no *neutral stable disturbance* of this degenerate type.

In order to determine whether the flow is stable or not for this degenerate type of disturbance, we have to find a complex c that satisfies Eqs. (4) and (5) with positive real α, β, and R. Reynolds Number must be real and positive in order to have some physical significance. The imaginary part of this complex c determines the stability of this type of disturbance.

Write

$$c = c_R + ic_i \tag{6}$$

Eq. (4) becomes

$$\Delta(u) = [D^2 - (\alpha^2 + \beta^2) - iR\alpha(V - c_R - ic_i)]u = 0 \tag{7}$$

Let $\bar{u}$ be the function conjugate to u which satisfies the equation

$$\Delta(\bar{u}) = [D^2 - (\alpha^2 + \beta^2) + iR\alpha(V - c_R + ic_i)]\bar{u} = 0 \tag{8}$$

and the same boundary conditions as u.

Multiply Eq. (7) by $\bar{u}$ and Eq. (8) by u and subtract and integrate across the field. Then

$$0 = \int_{-1}^{1} [\bar{u}\,\Delta u - u\,\Delta\bar{u}]\,dy = -2iR\alpha \int_{-1}^{1} (V - c_R)u\bar{u}\,dy \tag{9}$$

performing the same operations and adding, we have, after integrating by parts and making use of the boundary conditions,

$$-R\alpha c_i \int_{-1}^{1} u\bar{u}\,dy = 2\int_{-1}^{1} {}^1u'\bar{u}'\,dy + (\alpha^2 + \beta^2) \int_{-1}^{1} u\bar{u}\,dy \tag{10}$$

where $u' = du/dy$, and $\bar{u}' = d\bar{u}/dy$.

All the integrals in Eq. (10) are positive real numbers. By definition, α and β are positive real numbers. Hence, for positive real Reynolds Number R, c_i must be negative. Hence, all profiles $V(y)$ are stable for disturbances of this degenerate type.

Eq. (9) determines the velocity of propagation of this degenerate type of disturbance.

REFERENCE

[1] Squire, H. B., *On the Stability for Three-Dimensional Disturbance of Viscous Fluid Flow Between Parallel Walls*, Proc. Roy. Soc. London A., Vol. 142, pp. 621–628, 1933.

Base Pressures at Supersonic Velocities

A. Gabeaud

Centre d'Essais de Méchanique des Fluides, Paris, France

May 1, 1950

I HAVE JUST NOTICED in the Readers' Forum (JOURNAL OF THE AERONAUTICAL SCIENCES, Vol. 17, No. 3, P. 185, March, 1950) the note by Freeman K. Hill on "Base Pressures at Supersonic Velocities," in which the author, after recalling the results observed in free flight and in a wind tunnel for Mach Numbers up to 2.5 and mentioning the theoretical relationship that I proposed some time ago,[1] drew attention to a recent result obtained at $M = 5.1$ in a wind tunnel. The author suggested a

semiempirical expression for the base pressure for Mach Numbers between 2 and 6 as follows:

$$C_B = f\frac{2}{\gamma M^2}\left(1 - \frac{\gamma - 1}{2}\lambda M^2\right)^{\gamma/(\gamma-1)} - \frac{2}{\gamma M^2} \qquad (1)$$

where f and λ are two adjustable coefficients whose values are determined from the experimental results observed for $M = 2.5$ and $M = 5.1$ ($f = 0.5394$; $\lambda = 0.055$).

It has not escaped Hill's notice that this expression leads to a negative value of the base pressure for values of M greater than 9.5, and for this reason he recommended its use only up to $M = 6$.

Having recalled this fact, I wish to make the following two remarks:

(1) The theoretical law that I proposed in 1936 gives $C_B = -0.034$ at $M = 5.1$; the most recent law that I communicated in 1949[1] and which takes the simple form

$$C_B = \frac{2}{\gamma M^2}\frac{2\gamma M^2 - (\gamma - 1)}{\gamma + 1}\left(\frac{2}{\gamma + 1}\right)^{1.4}\frac{1}{M^{2.8}} - \frac{2}{\gamma M^2} \qquad (2)$$

gives $C_B = -0.0415$. The theoretical result is then confirmed very well by experiment ($C_B = -0.0457$).

(2) The same theoretical law does not give a perfect vacuum until $M = \infty$.

From these two remarks it would appear that the theoretical law, Eq. (2), which is well verified by experiment in the regions from $M = 1.8$ to $M = 5.1$ and which does not predict a perfect vacuum until $M = \infty$, is preferable to the semiempirical law, Eq. (1) [Hill's Eq. (2)], the use of which presents the inconveniences indicated by its author above $M = 5.1$.

Reference

[1] Gabeaud, A., *Base Pressures at Supersonic Velocities*, Readers' Forum, Journal of the Aeronautical Sciences, Vol. 16, No. 10, p. 638, October, 1949.

Note on the Calculation of Deflections of Indeterminate Structures

Bruno A. Boley* and Roland H. Mooret
Goodyear Aircraft Corporation, Akron, Ohio
May 10, 1950

A SIMPLIFICATION IS PRESENTED HERE of the usual method of calculating deflections of indeterminate structures by means of the principle of virtual displacements. A review of the literature, including some of the best-known texts on the subject, was carried out; none of the works consulted appeared to mention the possibility of this simplification (however well known it may be to practicing engineers). It was therefore decided to present it in the hope that, once the advisability of mentioning it were pointed out, it would find its way in new books and in new editions of old ones.

The usual procedure in calculating deflections is as follows. Let the deflection δ_A of a point A in the structure in question be required in a given direction. The internal strains in the structure caused by the external loads will be denoted by ϵ_x, ϵ_y, ϵ_z, γ_{xy}, γ_{yz}, and γ_{zx}, following the usual notation. If the structure is indeterminate, the evaluation of these strains will require use of virtual work or some equivalent concept related to the distortions of the structure. This calculation may be considered the first step in the determination of deflections, and no simplification of it is suggested here.

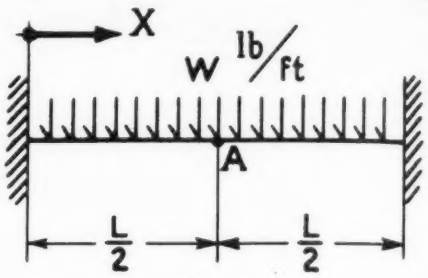

FIG. 1.

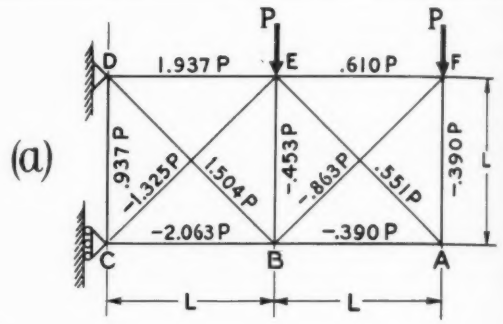

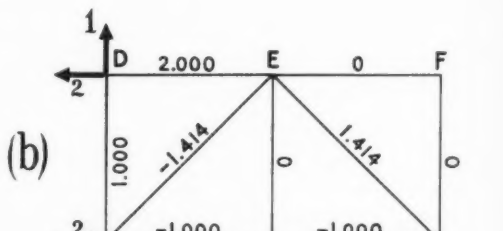

FIG. 2.

In the next step, a dummy system of self-equilibrating loads is applied to the structure. The dummy system is chosen in such a manner that it does work only when a deflection δ_A occurs at point A in the desired direction and has such a magnitude that this work is equal to δ_A. The internal stresses due to the dummy system will be denoted by σ_x', σ_y', σ_z', τ_{xy}', τ_{yz}', and τ_{zx}'.

The equilibrium of the structure under the dummy system is then tested (though it was established at the outset) by means of the principle of virtual displacements. This principle states that a system of forces is in equilibrium if, and only if, the work done by it during any arbitrary virtual displacement is zero. The work done by the dummy system must then also be zero when the actual displacements of the structure are used. This work is the sum of the external and internal work; or

$$\delta_A - \oint(\sigma_x'\epsilon_x + \sigma_y'\epsilon_y + \sigma_z'\epsilon_z + \tau_{xy}'\gamma_{xy} + \tau_{yz}'\gamma_{yz} + \tau_{zx}'\gamma_{zx})dx\,dy\,dz = 0,$$ from which the deflection δ_A is easily obtained.

* Engineering Specialist. Now, Assistant Professor of Aeronautical Engineering, The Ohio State University.
† Stress Analyst.

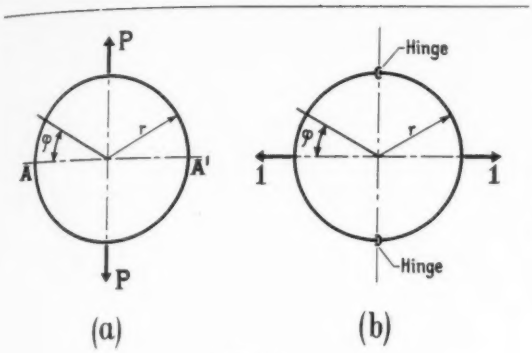

FIG. 3.

The only requirements that the dummy system is expected to satisfy in this derivation are those of equilibrium; at no time is it required that the stresses due to it satisfy the compatibility conditions for the structure. Hence, the following simplification may be employed: that, in obtaining the stresses due to the dummy load, it is not necessary to ensure continuity of displacements throughout the structure and that, therefore, the redundant members of the structure may be neglected in this part of the calculations.

It may seem at first that, if this is done, the displacements used to calculate the virtual work violate the conditions of restraint of the structure considered. This is not the case, however, since the principle of virtual displacements is in reality applied only to the simplified structure acted upon by the dummy loads. The displacements of the given structure do not violate any of the restraints of the simplified one.

Three examples of the use of this simplification are indicated below.

Let the deflection at point A in the beam of Fig. 1 be required. Then the dummy system consists of a 1-lb. load downward at A and a $^1/_2$-lb. load upward at each end, the redundant end moments being neglected. Hence, for this part of the calculations the beam reduces to a simple beam.

Fig. 2b shows the dummy system to be used in finding the downward deflection of point A of the truss of Fig. 2a. In calculating the forces due to the dummy system the redundant bars may be disregarded; thus, the simplified truss of Fig. 2b results.

In obtaining the shortening of diameter AA' in Fig. 3a, the dummy system of Fig. 3b must be used. The determination of the bending moments due to the dummy loads may be simplified by the insertion of imaginary hinges (Fig. 2b) which eliminate two internal redundants (the third redundant being eliminated by considerations of symmetry).

The Effects of Weight Variation on the Range of Air-Borne Craft

Ralph W. Allen
Research Engineer, North American Aviation, Inc., Los Angeles, Calif.

May 25, 1950

DURING A PRELIMINARY ANALYSIS of a long-range aircraft design, it is frequently necessary to adjust the final weights from the original estimations. The results of this adjustment, among other things, usually affects the range of the craft. In order to achieve a first approximation as to the magnitude of this effect, without entering into exact calculations, the equation and curves derived herein can be applied.

The converse can also follow—that is, a change in the original estimated range of the craft introduces a change in the weight. These changes can be visualized immediately from the curves shown in Fig. 1.

The range of an air-borne craft traveling at a constant speed and maintaining a constant lift to drag ratio, powered by a system that maintains thrust to drag equalization, is expressed by the Breguet formula

$$R = I(L/D)\,V \log_e (W_G/W_E) \tag{1}$$

where:

R = range
I = specific impulse
L = lift
D = drag
W_G = gross weight of craft
W_E = weight empty of craft

The weight of the craft can be broken up into three major parts—namely,

$$W_G = W_F + W_S + W_P \tag{2}$$

in which

W_F = weight of Fuel
W_S = structural weight
W_P = pay load

The weight empty is defined as the sum of the pay load and structural weights

$$W_E = W_P + W_S \tag{3}$$

Let W_G/W_E be denoted by μ; then, if R_0 represents the initial range based on μ_0 and R_1 is the new range based on μ_1, the ratio of R_1/R_0 becomes, from Eq. (1),

$$R_1/R_0 = \log \mu_1/\log \mu_0 \tag{4}$$

This reduces to

$$\mu_1 = \mu_0^{R_1/R_0}$$

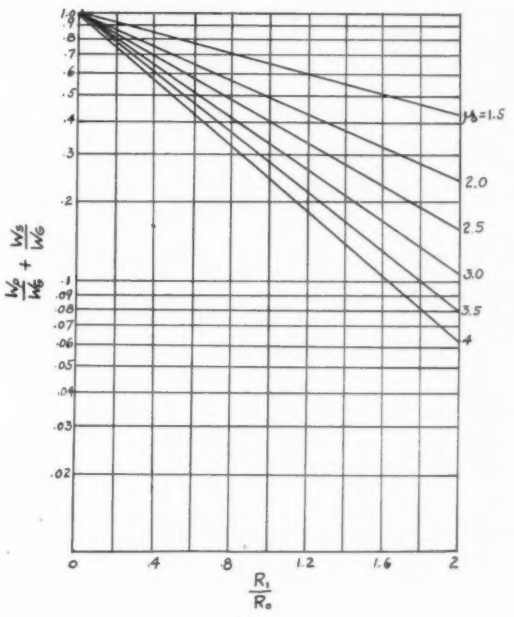

FIG. 1.

From Eqs. (2), (3), and (4), the following relations are deduced:

$$\mu_1 = [W_G/W_E]_1 = [W_G/(W_P + W_S)]_1 = \mu_0^{R_1/R_0}$$

reducing,

$$W_G/W_P = 1/\mu_0^{-R_1/R_0} - (W_S/W_G)] \quad (5)$$

or

$$(W_P/W_G) + (W_S/W_G) = \mu_0^{-R_1/R_0} \quad (6)$$

Under a given load criteria, the structural ratio W_S/W_0 usually remains fairly constant with respect to range changes, so that for a given structural weight ratio the ratio of gross weight to pay load is determined by Eq. (5).

From the results of Eq. (5), it is noticed that the gross weight of the craft increases exponentially with the range increase. Thus, given a gross weight and pay load, a new gross weight is found resulting from the designated range ratio.

The curves of Fig. 1 quickly aid in determining these various changes.

Library Facilities of the

Institute of the Aeronautical Sciences

To serve Institute members and others in the aeronautical industry, the Institute of the Aeronautical Sciences offers the facilities of:

The W. A. M. Burden Library

2 East 64th Street
New York 21, N.Y.

The facilities of this library are available for reference study at the Institute.

The Paul Kollsman Lending Library

2 East 64th Street
New York 21, N.Y.

This library loans books without charge to members and others in the United States over eighteen years of age. Full information will be sent on request.

The Pacific Aeronautical Library

7660 Beverly Boulevard
Los Angeles 36, Calif.

This is a service and reference library for West Coast members and organizations. Full information as to its facilities will be sent on request.